



저작자표시-비영리-변경금지 2.0 대한민국

이용자는 아래의 조건을 따르는 경우에 한하여 자유롭게

- 이 저작물을 복제, 배포, 전송, 전시, 공연 및 방송할 수 있습니다.

다음과 같은 조건을 따라야 합니다:



저작자표시. 귀하는 원저작자를 표시하여야 합니다.



비영리. 귀하는 이 저작물을 영리 목적으로 이용할 수 없습니다.



변경금지. 귀하는 이 저작물을 개작, 변형 또는 가공할 수 없습니다.

- 귀하는, 이 저작물의 재이용이나 배포의 경우, 이 저작물에 적용된 이용허락조건을 명확하게 나타내어야 합니다.
- 저작권자로부터 별도의 허가를 받으면 이러한 조건들은 적용되지 않습니다.

저작권법에 따른 이용자의 권리는 위의 내용에 의하여 영향을 받지 않습니다.

이것은 [이용허락규약\(Legal Code\)](#)을 이해하기 쉽게 요약한 것입니다.

[Disclaimer](#)

공학박사학위논문

**탄성과 모드 제어와
빔 조향이 가능한 메타물질**

**Mode controlling and Beam steering
Metamaterial for Elastic waves**

2021년 8월

서울대학교 대학원
기계항공공학부
이 우 림

탄성과 모드 제어와 빔 조향이 가능한 메타물질

Mode controlling and Beam steering
Metamaterial for Elastic waves

지도교수 김 윤 영

이 논문을 공학박사 학위논문으로 제출함

2021 년 4 월

서울대학교 대학원

기계항공공학부

이 우 립

이우립의 공학박사 학위논문을 인준함

2021 년 6 월

위 원 장 : 윤 병 동

부위원장 : 김 윤 영

위 원 : 김 도 년

위 원 : 오 주 환

위 원 : 이 혁

ABSTRACT

Mode controlling and Beam steering Metamaterial for Elastic waves

Woorim Lee

School of Mechanical and Aerospace Engineering

The Graduate School

Seoul National University

This dissertation aims to design and verify elastic metamaterials that precisely control multi modes of elastic waves and simultaneously control their propagation directions. Elastic ultrasound is used in various applications such as non-destructive testing and biomedical equipment, and a technology to precisely control the ultrasound is very important. Recently, elastic metamaterials, which are artificial structures capable of remarkably controlling ultrasonic waves, have attracted attention, but it is intrinsically difficult to control elastic waves because of their multi-modality involving both longitudinal and shear wave modes. As a result, the multi-modality poses serious limitations on elastic wave control.

In this study, we propose metamaterials that can steer wave beam directions and control their modes simultaneously. Specifically, the direction of the wave is controlled either by the elastic phononic crystals or the elastic metasurfaces. In the

course of this study, the condition in which the only desired wave propagates is established and used for the design of metamaterials. First, in elastic phononic crystals, the propagation of a single-mode wave is investigated through modal analysis. Experiments showed that an elastic phononic crystal designed to achieve this objective was shown to control elastic ultrasonic waves precisely.

Secondly, in the elastic metasurface, converting an incident elastic wave of a specific wave mode into a transmitted wave of a desired wave mode, either the same or different mode, is investigated. At the same time, the beam steering of the transmitted wave along a specific direction is considered. Using the transfer matrix and scattering matrix, we find the material properties of the unit cell that control the phase shift of the transmitted wave. The designed monolayer metamaterials can successfully control the phase shift with mode-conserving or mode-converting and steer the transmitted wave along the target direction. The proposed metamaterial analysis and design strategies are expected to greatly improve the elastic ultrasonic wave technology that requires precise control.

Keywords: Elastic metamaterial, Ultrasonic wave, Elastic wave mode control, Beam steering, Phononic crystal, Metasurface.

Student Number: 2015-20704

TABLE OF CONTENTS

ABSTRACT	i
TABLE OF CONTENTS	iii
LIST OF TABLES	vi
LIST OF FIGURES.....	vii
<CHAPTER 1> INTRODUCTION.....	1
1.1 Research Motivation	1
1.2 Research Objectives	3
1.3 Outline of Thesis	4
<CHAPTER 2> THEORETICAL BACKGROUND	7
2.1 Chapter Overview	7
2.2 Waves in an Elastic Media	8
2.2.1 Wave Equations for Elastic Bodies	9
2.2.2 Wave Reflection and Refraction at an Interface	12
2.3 Elastic Waves Transmission through an Anisotropic Material	14
2.3.1 Transfer Matrix.....	15
2.3.2 Scattering Matrix.....	18
2.4 Elastic Wave Propagation in a Periodic Structure	19
<CHAPTER 3> WAVE STEERING USING EQUI-FREQUENCY CONTOUR OF ELASTIC PHONONIC CRYSTALS.....	31
3.1 Chapter Overview	31

3.2 Elastic Phononic Crystal Prism Model.....	33
3.3 Wave Steering Simulation using EFC of Elastic Phononic Crystals.....	34
3.3.1 Dispersion curve of phononic crystals	35
3.3.2 Design Analysis using EFC.....	35
3.3.3 Verification of the EFC analysis by time-transient simulations	38
3.4 Wave Cancellation of two waves through a Phononic Crystal Prism	38
3.4.1 Calculate the widths of the incident source beams.....	38
3.4.2 Calculate the phases of the incident source beams.....	39
3.4.3 Numerical Simulation Verification.....	39
3.5 Experimental Validation.....	41
3.6 Summary	44
<CHAPTER 4> MONOLAYER FULL-TRANSMISSIVE ELASTIC	
 METASURFACES WITH PERFECT MODE CONTROL.....	54
4.1 Chapter Overview	54
4.2 Research Background: Generalized Snell’s Law for Multi-Mode waves in Elastic Metasurfaces.....	56
4.3 Research Background: Lens Equation for Mode-converting metalens.....	58
4.4 Amplitude and Phase of Transmitted Wave through an Anisotropic Material Layer	59
4.5 Design a Mode-converting Metasurface	60
4.5.1 Phase control condition with mode-conversion	61
4.5.2 Design of Phase-controlling Unit Cells with Mode-conversion.....	65

4.5.3 Transmission and Phase Spectra for 4 Unit Cells.....	66
4.5.4 Various Numerical Simulation of Metasurfaces.....	67
4.6 Design a Mode-conserving Metasurface.....	72
4.6.1 Phase Control condition with Mode-conservation.....	73
4.6.2 Design of Phase-controlling Unit Cells with mode-conservation..	78
4.6.3 Transmission and Phase Spectra for 16 Unit Cells.....	78
4.6.4 Various Numerical Simulation of Metasurfaces.....	81
4.7 Experimental Validation.....	84
4.8 Summary.....	86
<CHAPTER 5> CONCLUSIONS	119
APPENDIX A. Variables affecting the efficiency of metasurfaces.....	123
REFERENCES.....	131
ABSTRACT (KOREAN).....	139
ACKNOWLEDGEMENTS.....	141

LIST OF TABLES

Table 4.1 Values of lengths, widths, and angles of slits in designed models.....	87
Table 4.2 Transmission coefficient of L to S mode-converting metasurface for each incident angle.	88
Table 4.3 Phase shift values of unit cells when longitudinal and shear waves are incidence.	89
Table 4.4 The detailed values of slits in designed unit cells.....	90
Table 4.5 Transmission coefficient of mode-conserving metasurface for each mode of incident wave.	91
Table 4.6 Unit cells rearranged for the mode-splitting metasurface. And phase shift values when longitudinal and shear waves are incidence.	92

LIST OF FIGURES

Fig. 2.1 3D elastic body with body force.	24
Fig. 2.2 Refraction and reflection of wave which enters from material A to material B.	25
Fig. 2.3 Wave propagation along +x-axis from material A to material C.	26
Fig. 2.4 (a) 1-dimensional periodic structure model. (b) The unit cell of the periodic structure.	27
Fig. 2.5 Dispersion relation of the 1D periodic structure.	28
Fig. 2.6 (a) 2-dimensional periodic structure model composed of material A and B. (b) The unit cell of the periodic structure.	29
Fig. 2.7 Dispersion surface for the 2-dimensional lattice of the first Brillouin zone. The dispersion surface is symmetric about k_x -axis and k_y -axis.	30
Fig. 3.1 A schematic configuration to verify wave cancellation phenomenon with an elastic phononic crystal.	46
Fig. 3.2 (a) Dispersion curves of utilized PC structure, (b) the mode shape of the branch(SH0 mode) used in our research with red points of dispersion curves, (c) the mode shape of the other branch (A0 mode) with green points of dispersion curves.	47
Fig. 3.3 Analysis of the refraction mechanism by using EFCs.	48
Fig. 3.4 The snapshots of wave field by (a) positive source and (b) of negative source at different time steps. (The color level denotes the magnitude of the	

displacement field.)	49
Fig. 3.5 Shear displacement plot time-harmonic simulation for (a) positive, (b) negative and (c) both sources.	50
Fig. 3.6 Time transient simulation of the displacement component yieldin shear stress for each case and displacements of refracted waves (blue line: positive, black line: negative and red line: both sources) along the red line in the simulation. The red line is located at $x = 0$ and it is 7 cm long in the y -direction. (For interpretation of the references to colour in this figure legend, the reader is referred to the web version of this article.)	51
Fig. 3.7 (a) The experimental setup and a PSA-OPMT configuration. (b) Raw data for 3 cases at the red point in Fig. 3.7 (a).....	52
Fig. 3.8 Contour plots of acquired data obtained from (a) the numerical simulation and (b) the experiments.	53
Fig. 4.1 A schematic diagram of elastic mode-control metasurface.....	93
Fig. 4.2 The diagram of wave path from material 1 to material 2 to derive generalized Snell's law for multi-mode. There is a metasurface between two materials.	94
Fig. 4.3 The diagram of wave path from material 1 to material 2 to derive phase equation for wave focusing. There is a metalens between two materials..	95
Fig. 4.4 The model for applying transfer matrix method consider (a) the only metamaterial layer and (b) background medium. The left and right medium is a background medium and the center medium is a metamaterial.	96

Fig. 4.5 Shape optimization model with 6 variables for mode-converting metamaterial.....	97
Fig. 4.6 2 mode-converting unit cells designed by shape optimization. The detailed values of lengths, widths, and angles of slits are written in Table. 4.1.....	98
Fig. 4.7 Simulation verification of designed unit cells. The two simulation results in Model A are the simulation results for the effective medium and the designed unit cell from above. Similarly, the two simulation results in Model B are the simulation results for the effective medium and the designed unit cell from above.	99
Fig. 4.8 (a) The phase shift of the transmitted shear wave is controlled by using the flipped model A. An incident longitudinal wave is shown on the left side of the unit cell, and a transmitted shear wave is shown on the right side. (b) Simulation results over a wider area is shown to check the phase shift in more detail.....	100
Fig. 4.9 Transmission and phase spectra of the transmitted shear waves using model A, model B, and the reversed models.....	101
Fig. 4.10 Metasurface and phase gradient graph constructed using designed models.	102
Fig. 4.11 Simulation results when a longitudinal wave enters into the mode-conversion metasurface. (a) Longitudinal wave field and (b) shear wave field are plotted respectively.....	103
Fig. 4.12 The results of frequency sweeps when a longitudinal wave enters into the	

designed metasurface.	104
Fig. 4.13 Simulation results when a shear wave enters into the mode-conversion metasurface. (a) Longitudinal wave field and (b) shear wave field are plotted respectively.....	105
Fig. 4.14 (a) Designed unit cells with target frequency of 125 kHz. (b) Transmission and phase spectra using two designed models.	106
Fig. 4.15 Metasurface configuration at 125 kHz and simulation results when longitudinal waves are incident.....	107
Fig. 4.16 Simulation results when the longitudinal wave oblique incidence with incidence angle (a) 10° and (b) 30° in the metasurface designed at 100 kHz.	108
Fig. 4.17 (a) Phase gradient graph(Φ - x) for L to S metalens with focal point $p = 0.5$ m and simulation result when longitudinal wave is incident. (b) Longitudinal wave field and (c) shear wave field are plotted respectively.	109
Fig. 4.18 (a) Phase gradient graph(Φ - x) for S to L metalens with focal point $p = 0.3$ m and simulation result when shear wave is incident. (b) Longitudinal wave field and (c) shear wave field are plotted respectively.	110
Fig. 4.19 Shape optimization model with 8 variables for mode-conserving metamaterial.....	111
Fig. 4.20 Supercell of metasurface for (a) only one wave mode (b) multi-mode.	112
Fig. 4.21 Transmission and phase spectra for the mode-conservation metasurface	

when (a) longitudinal waves and (b) shear waves enter into designed 16 unit cells respectively.	113
Fig. 4.22 Simulation results for the mode-conservation metasurface when (a) only longitudinal waves (b) only shear waves and (c) both waves enter.	114
Fig. 4.23 Transmission and phase spectra for the mode-splitting metasurface when (a) longitudinal waves and (b) shear waves enter into designed 16 unit cells respectively.....	115
Fig. 4.24 Simulation results for the mode-splitting metasurface when (a) only longitudinal waves (b) only shear waves and (c) both waves enter.	116
Fig. 4.25 (a) Experiment model when there is no metasurface on an aluminum plate. (b) Experiment model when there is a mode-conversion metasurface on an aluminum plate. (c) Raw data of target direction(0°) of the longitudinal wave in the model without the metasurface. (d) Raw data of target direction(17.46°) of the shear wave in the model without the metasurface.	117
Fig. 4.26 Radiation pattern graph for experimental results. The solid line is the simulation result when there is a metasurface, and the dotted line is the simulation result when there is no metasurface. The circle and the cross mark are experimental results.	118
Fig. A.1 (a) Simulation model using effective medium while controlling the phase gradient, thickness, and number of unit cells in the mode-converting metasurface (b) Combination of controlled variables	126

Fig. A.2 The simulation results that plot shear wave field when the phase gradient is small, the smallest thickness w_0 is fixed, and the number of unit cells n is changed. 127

Fig. A.3 The simulation results that plot shear wave field when the phase gradient is small, the smallest thickness w_0 is changed, and the number of unit cells n is fixed. 128

Fig. A.4 The simulation results that plot shear wave field when the phase gradient is large, the smallest thickness w_0 is fixed, and the number of unit cells n is changed. 129

Fig. A.5 The simulation results that plot shear wave field when the phase gradient is large, the smallest thickness w_0 is changed, and the number of unit cells n is fixed. 130

<CHAPTER 1>

INTRODUCTION

1.1 Research Motivation

Elastic ultrasound is very important in modern society, since it is used for biomedical imaging or non-destructive testing. As these technologies using elastic ultrasound are related to safety or human body, ultrasonic waves should be handled more precisely. Since these are techniques that require precision, ultrasound needs to be controlled in the entire process from excitation to reception. In particular, the technique of excitation of ultrasound in a desired direction is really important in the applications.

Metamaterials have recently been studied to dramatically control waves. They are artificial structures that overcome the limitations of wave phenomena created by conventional materials, and create various anomalous wave phenomena such as superlens, cloaking, metasurface and negative refraction/reflection. The medium which has a unique structure is necessary for anomalous wave phenomena that are not presented in conventional materials. Metamaterials are divided into phononic crystal structures and metamaterial structures depending on the size of the unit cell. The phononic crystals are structures that create anomalous wave phenomena by the

periodic arrangement of structures. The size of the phononic crystal unit cell is larger than the wavelength of target waves, and the phononic crystal controls the waves using wave scattering. And metamaterials have effective properties that cannot be realized in natural material through design using special principles such as resonance. Metamaterials designed with subwavelength of the wave are expressed as effective materials. Both the phononic crystal structures and the metamaterial structures occur a variety of anomalous wave phenomena, but have different physical principles. In other words, the phononic crystal creates anomalous wave phenomena only by a periodic structure, and the metamaterial can maximize the efficiency through a periodic arrangement. But the anomalous wave phenomena can appear with a single metamaterial structure.

Meanwhile, there are many studies of metamaterials on elastic ultrasound used for biomedical imaging or non-destructive testing. However, compared to acoustics and electromagnetics, which are other wave fields, multi modes exist in elastic waves, and it is difficult to control elastic ultrasonic waves. Also, since the wave modes affect each other complexly, the technology development of elastic metamaterials is lacked compared to metamaterial technologies in other wave fields. Like other waves in which only one wave mode exists, there are many studies on one wave mode in the elastic metamaterials. Since there are multi modes in elastic waves, the analysis is inaccurate because of undesired mode waves. And due to this problem, there is a serious obstacle in applying the elastic metamaterial to the actual applications.

1.2 Research Objectives

In order to overcome the limitations of the elastic metamaterial aforementioned, this thesis is dedicated to control the direction of the wave while considering the elastic wave mode. The reason why elastic metamaterials have developed as targets for only single mode so far is that it has been difficult to design metamaterials for multiple modes. However, metamaterials that freely convert wave modes have been designed and verified as metamaterials for the modes of elastic waves have recently been studied. Therefore, it is possible to design a metamaterial structure that realizes anomalous wave phenomena through innovative applications of mode controlling metamaterials.

In this dissertation, two methods are presented as methods of controlling the direction of elastic waves. One is a method using a scattering-based phononic crystal structure, which creates anomalous wave phenomena through periodic arrangement of structures. Through analysis based on response, waves of other modes do not propagate at a specific frequency, and only one-mode wave propagates. The refraction angle of the wave is controlled by changing the shape of the periodically arranged structures while the mode is fixed. Furthermore, wave cancellation is realized through appropriate tuning using the controlled waves.

Secondly, a metasurface is used to control the direction of the elastic wave. A metasurface is a metamaterial that changes direction through the phased array of waves, and is a structure which consists of various metamaterial unit cells. The metamaterials constituting the metasurface are designed differently, and the phase

shift is controlled by transmitting or reflecting the wave incident on the metamaterial. In this study, each metamaterial constituting the metasurface conserves or converts the mode of the incident wave and transmits it. In other words, metamaterials having the transmittance of 100% for the converted or conserved wave mode and controlling different phase shifts are designed. Like a phased array transducer, the direction of the transmitted wave is controlled by phase arrangement of designed unit cells properly.

1.3 Outline of Thesis

The thesis is organized as follows.

In <**Chapter 2**>, the theoretical background for elastic waves will be reviewed. First, the Christoffel equation which is an elastic wave equation will be introduced. Next, for the design of metamaterials to control the direction of waves, we will introduce the theory of refraction, transmission, and reflection of waves when waves travel from one medium to another. In addition, we will review the transfer matrix method, which is a simple way to describe the wave transmission. Finally, since metamaterials with periodicity can realize anomalous wave phenomena, we will introduce waves in periodic structures to understand the basic theory of metamaterials.

<**Chapter 3**> describes a study on controlling the direction of waves using an elastic phononic crystal structure designed based on scattering. The phononic crystal has a

unit cell which is longer than the wavelength of the wave, and anomalous wave phenomena appear through the periodic arrangement. In order to understand the wave motion in the periodic structure, the dispersion curve and the Equi-frequency Contour (EFC) are obtained based on the response through finite element analysis simulation. Using EFC, we design the phononic crystal structure so that the wave can be deflected onto the desired direction, and confirm that the direction of the wave is controlled through numerical simulation. And the controlled waves can be cancelled each other. Waves of two different incident angles are controlled to propagate in the same direction by controlling each other, and wave cancellation is realized by appropriately tuning the phase. Finally, it is verified through an experiment to confirm if there is wave cancellation actually. This technology for controlling the wave direction can be implemented through periodic arrangement of simple shapes, and is expected to be applicable in various ways in the future.

In <**Chapter 4**>, the direction of transmitted or reflected waves is controlled using metasurfaces, which are metamaterials that control the direction of waves. Since there are multi modes in the elastic wave, the metasurface is designed in consideration of the wave mode by converting or conserving wave mode. The design of the metasurface requires the design of a metamaterial unit cell that transmits or reflects a wave with a desired phase shift in 1-dimension. The metasurface is composed of phased array of the designed metamaterials. Before designing the metamaterial unit cell, we approach theoretically with transfer matrix method for

finding the principle of controlling the phase of transmitted wave. Next, we design metamaterial unit cells that control the phase shift of transmitted wave by shape optimization design. The designed unit cells transmit the wave with the desired wave mode and the desired phase shift by converting or conserving wave mode at the same time. The metasurface is composed of the designed unit cells, and it is verified that the wave of the desired wave mode propagates in the desired direction through numerical simulation and experiment. It is expected that the metasurface design technique, which simultaneously controls the wave mode and direction of elastic waves, can be applied as actual applications to develop the elastic metamaterial technical level.

In <**Chapter 5**>, the overall conclusion of this dissertation will be presented.

<CHAPTER 2>

THEORETICAL BACKGROUND

2.1 Chapter Overview

In this chapter, we will review the theory of elastic waves used in this dissertation. Because the research objective is a steering technology that considers the mode control of elastic waves, we will first review a theoretical introduction to elastic waves. We introduce the basic equations for elastic waves, refraction and reflection phenomena when waves are incident and transmitted through different media. Next, we introduce refraction and reflection phenomena when waves are incident and transmitted through different media. This is very useful for estimating the refraction angle or inversely designing the wave steering system. Next, we theoretically approach how waves have anomalous behavior in a periodic structure. Analysis of periodic structures has been carried out for decades, and in recent years, it is gaining attention as it has established itself as an appropriate theory for many materials such as composite materials. Although there is a wealth of applied research on periodic structures, this chapter tries to cover a model that uses periodic structures to define elastic metamaterials, especially in terms of waves. In particular, we explain in detail the difference from the wave in the continuum.

Next, we will review the transfer matrix and the scattering matrix, which are powerful tools that can calculate transmitted and reflected waves for waves that pass through different media. The transfer matrix method represents the boundary conditions at the contact surface in the case of waves with different media as a matrix. In general, the amplitude and phase of a wave are expressed by a complex formula representing the wave. However, when calculating the amplitude and phase of reflected or transmitted waves, the common expression is used over and over again, which leads to impediments to the calculation. The transfer matrix is a matrix related to displacement and stress, and it simplifies the calculation process as it can express only essential information about the equation for the boundary condition. Next, the scattering matrix is a matrix of the amplitude and phase of the wave, and by using this, the amplitude and phase of the reflected and transmitted waves can be obtained. In this chapter, we will introduce in detail the general appearance of the two matrices used in this study.

2.2 Waves in an Elastic Media

In order to know the anomalous wave phenomena using metamaterials to be covered in this dissertation, it is necessary to first deal with basic theory about elastic waves. In this section, we will introduce the constitutive equation for the most basic elasticity and the wave equation using it. Next, we will show that how wave reflection and transmission occur when a wave is incident from one medium to another.

2.2.1 Wave Equations for Elastic Bodies

In an elastic body, the elastic force and the displacement field are expressed as a second order tensor. The relationship between elastic force and displacement is expressed by the linearized elastic constitutive equation (or Hooke's law) and is as follows.

$$\sigma_{ij} = c_{ijkl} \varepsilon_{kl} \quad (i, j, k, l = x, y, z) \quad (2.1)$$

Where σ_{ij} is the stress on ij plane, c_{ijkl} is the component of the stiffness matrix C expressed as tensor, and ε_{kl} is the strain on kl plane. The C matrix expressing the relationship between stress and strain is complex because it is generally a 6 by 6 matrix. Each component has a relational expression if the medium through which the wave propagates is isotropic, and has an independent value if it is anisotropic. For a thin plate in which the medium is isotropic and is a plane-stress condition, Eq. (2.1) becomes as follows.

$$\begin{bmatrix} \sigma_{xx} \\ \sigma_{yy} \\ \sigma_{zz} \\ \sigma_{yz} \\ \sigma_{zx} \\ \sigma_{xy} \end{bmatrix} = \frac{E}{1-\nu^2} \begin{bmatrix} 1 & -\nu & -\nu & 0 & 0 & 0 \\ -\nu & 1 & -\nu & 0 & 0 & 0 \\ -\nu & -\nu & 1 & 0 & 0 & 0 \\ 0 & 0 & 0 & 1+\nu & 0 & 0 \\ 0 & 0 & 0 & 0 & 1+\nu & 0 \\ 0 & 0 & 0 & 0 & 0 & 1+\nu \end{bmatrix} \begin{bmatrix} \varepsilon_{xx} \\ \varepsilon_{yy} \\ 0 \\ 0 \\ 0 \\ \varepsilon_{xy} \end{bmatrix} = C \begin{bmatrix} \varepsilon_{xx} \\ \varepsilon_{yy} \\ 0 \\ 0 \\ 0 \\ \varepsilon_{xy} \end{bmatrix} \quad (2.2)$$

In this paper, an anisotropic medium is approached to deal with the most common case. In Fig. 2.1, the equation of motion for a general medium is as follows.

$$\sigma_{ji,j} + b_i = \rho \frac{\partial^2 u_i}{\partial t^2} \quad (2.3)$$

Where b is the body force in the elastic body, and ρ is density of the elastic body.

If no external force is applied, the body force b_i is 0. In the time-harmonic condition where the wave continues to propagate, the displacement u can be expressed as $u_i = U_i \exp\{i(kx - \omega t)\}$, and the Christoffel equation, the elastic wave equation, is derived by using the constitutive equation of Eq. (2.1).

$$k^2 \Gamma \vec{u} = \rho \omega^2 \vec{u} \quad (2.4)$$

Here, Γ is a Christoffel matrix containing stiffness properties of the medium. The Christoffel matrix is expressed as the stiffness tensor C_{ij} . The C matrix seen earlier is expressed as 6 by 6, but the stiffness tensor can be simplified when the wave propagates only along x -axis, which is as follows.

$$\Gamma = \begin{bmatrix} C_{11} & C_{16} & C_{15} \\ C_{61} & C_{66} & C_{56} \\ C_{51} & C_{65} & C_{66} \end{bmatrix} \quad (2.5)$$

And the Christoffel equation can be expressed simply.

$$k^2 \begin{bmatrix} C_{11} & C_{16} & C_{15} \\ C_{61} & C_{66} & C_{56} \\ C_{51} & C_{65} & C_{66} \end{bmatrix} \begin{bmatrix} u_x \\ u_y \\ u_z \end{bmatrix} = \rho \omega^2 \begin{bmatrix} u_x \\ u_y \\ u_z \end{bmatrix} \quad (2.6)$$

The displacement u_i ($i = x, y, z$) for possible waves in a 3D anisotropic material can be written as

$$u_i = \left(\sum_{j=1}^6 A_j P_j^i e^{i\alpha_j x} \right) e^{-i\omega t} \quad (2.7)$$

where A_j is the displacement amplitude of the particles for 3 different eigenwaves propagating along positive and negative i -axis, α_j is the wave number of the eigenwaves with the relation $\alpha_1 = -\alpha_2$, $\alpha_3 = -\alpha_4$, $\alpha_5 = -\alpha_6$, and P_j^i is the mechanical polarization vector component with the relation $P_1^i = P_2^i$, $P_3^i = P_4^i$, $P_5^i = P_6^i$. In Eq. (2.6), in order for u_x and u_y to have non-trivial solution, the characteristic determinant must be 0. The eigenvalue and eigenvector of the matrix Γ can be obtained, and it is possible to know various information such as the wave numbers and mechanical polarization vector.

$$\left| k^2 \Gamma - \rho \omega^2 \mathbf{I} \right| = 0 \quad (2.8)$$

Where \mathbf{I} is the identity matrix. For an isotropic medium, the eigenvalues are obtained as

$$C_{11} = \frac{\rho \omega^2}{k_L^2} \quad (2.9a)$$

$$C_{55} = C_{66} = \frac{\rho \omega^2}{k_S^2} \quad (2.9b)$$

Where k_L and k_S represent the wave numbers of a longitudinal mode and two shear modes, respectively. And the eigenvectors are obtained as

$$\begin{aligned}
P_1^x = P_2^x = 1, P_3^x = P_4^x = P_5^x = P_6^x = 0 \\
P_3^y = P_4^y = 1, P_1^y = P_2^y = P_5^y = P_6^y = 0 \\
P_5^z = P_6^z = 1, P_1^z = P_2^z = P_3^z = P_4^z = 0
\end{aligned} \tag{2.10}$$

2.2.2 Wave Reflection and Refraction at an Interface

As shown in Fig. 2.2, when a wave is generally incident from one medium to another, reflection and refraction of the wave occur. If the boundary condition is known at the interface, the amplitude of the reflected wave and the refracted wave and the angle of refraction can be mathematically calculated. First, the calculation of the angle of refraction can be known by the commonly known Snell's law, and the Snell's law is as follows.

$$\frac{c_l^A}{\sin \alpha_A} = \frac{c_s^A}{\sin \beta_A} = \frac{c_l^B}{\sin \alpha_B} = \frac{c_s^B}{\sin \beta_B} \tag{2.11}$$

Here, c denotes the wave velocity, A and B denote the medium, respectively, and l and s denote the longitudinal and shear modes of the wave. For Snell's law, if you change the speed of a wave to a wave number, the equation changes as follows.

$$\begin{aligned}
k_{\tan}^A &= k_l^A \sin \alpha_A = k_s^A \sin \beta_A \\
&= k_l^B \sin \alpha_B = k_s^B \sin \beta_B = k_{\tan}^B
\end{aligned} \tag{2.12}$$

Here, k means the wavenumber, and equation (2.12) means that k in the tangential direction of the interface does not change while transmitting from one medium of

the wave to another. Next, in order to calculate the amplitude of the refracted wave and the reflected wave, it is first necessary to know the boundary conditions at the interface. The boundary condition can be expressed as the continuity of the displacement and the continuity of the stress at the interface.

As shown in Fig. 2.2, for medium A and B , the displacement in the x direction in each medium is $u_A(x, z)$ and $u_B(x, z)$, and the displacement in z direction is $w_A(x, z)$ and $w_B(x, z)$. Stresses are $\sigma_{xx}^A(x, z)$, $\sigma_{xx}^B(x, z)$, $\sigma_{xz}^A(x, z)$, and $\sigma_{xz}^B(x, z)$. If the boundary condition is expressed as equations, it is as follows.

$$\begin{aligned}
 u_A(x, 0^-) &= u_B(x, 0^+) \\
 w_A(x, 0^-) &= w_B(x, 0^+) \\
 \sigma_{xx}^A(x, 0^-) &= \sigma_{xx}^B(x, 0^+) \\
 \sigma_{xz}^A(x, 0^-) &= \sigma_{xz}^B(x, 0^+)
 \end{aligned} \tag{2.13}$$

Since the medium through which the wave propagates is an elastic medium in which several modes can exist, when the wave is incident on the interface, the reflected and refracted waves have P wave and SV wave, respectively. There are a total of 4 variables, φ_1 , ψ_1 , φ_2 , and ψ_2 , and since equation (2.13) has 4 equations, there are roots, and the magnitude of each wave is calculated. Because the calculation is very complicated, this paper introduces the transmittance and reflectance of the case where the wave is vertically incident ($\alpha_A = 0$). When a longitudinal wave is incident, the transmittance and reflectance of each mode are as follows.

$$\begin{aligned}
A_{\varphi_1} / A_1 &= \frac{\rho_B c_l^B - \rho_A c_l^A}{\rho_B c_l^B + \rho_A c_l^A} \\
A_{\psi_1} / A_1 &= 0 \\
A_{\varphi_2} / A_1 &= \frac{2\rho_B c_l^B}{\rho_B c_l^B + \rho_A c_l^A} \\
A_{\psi_2} / A_1 &= 0
\end{aligned}
\tag{2.14}$$

Different modes are not formed because of normal incidence, and different modes are generated when the wave is obliquely incident. In any case, the size of the refracted wave and the reflected wave can be calculated using the boundary condition of Eq. (2.13).

2.3 Elastic Waves Transmission through an Anisotropic Material

This section covers a transfer matrix that can efficiently calculate the amplitude and phase when waves are propagated and transmitted to other media. The velocity and stress at each point continuously change depending on time and location of the wave, and it is very important to estimate the velocity and stress at a specific location to understand the wave. However, estimating these velocity and stress is mathematically complex, and even more difficult in elasticity where several modes can exist at the same time. To solve this complex equation, we introduce the concept of a transfer matrix. Furthermore, by using velocity and stress, the amplitude and

phase of the wave can be accurately calculated. The matrix used in the relationship between amplitude and phase is called a scattering matrix, and will be introduced at the same time in this section.

2.3.1 Transfer Matrix

In this subsection, a transfer matrix is introduced when a wave propagates in a time-harmonic situation along the x -axis in one direction in 2D. Since the 2-dimensional situation is considered, the variables related z -axis such as u_z are excluded. Figure 2.3 shows a case where a wave propagates in the $+x$ -axis and enters into another medium. Because of Eq. (2.1), the stress of the wave for material A in the figure can be expressed as the amplitude of the particle. The equations to introduce the transfer matrix are written as

$$\sigma = C\varepsilon = C \frac{\partial u}{\partial x}, \quad v = \frac{\partial u}{\partial t}. \quad (2.15)$$

Because the equations are complex to solve, they are expressed by matrices.

$$\begin{bmatrix} v_x \\ v_y \\ \sigma_{xx} \\ \sigma_{xy} \end{bmatrix} = \mathbf{M} \begin{bmatrix} A_1 \\ A_2 \\ A_3 \\ A_4 \end{bmatrix} \quad (2.16)$$

The matrix expressing the relationship between velocity, stress, amplitude, and phase is called \mathbf{M} matrix. The components of the \mathbf{M} matrix are given as

$$M_{11} = -i\omega P_1^x, M_{12} = -i\omega P_2^x, M_{13} = -i\omega P_3^x, M_{14} = -i\omega P_4^x \quad (2.17a)$$

$$M_{21} = -i\omega P_1^y, M_{22} = -i\omega P_2^y, M_{23} = -i\omega P_3^y, M_{24} = -i\omega P_4^y$$

$$M_{31} = i\alpha_1 (C_{11}P_1^x + C_{16}P_1^y), M_{32} = i\alpha_2 (C_{11}P_2^x + C_{16}P_2^y)$$

$$M_{33} = i\alpha_3 (C_{11}P_3^x + C_{16}P_3^y), M_{34} = i\alpha_4 (C_{11}P_4^x + C_{16}P_4^y) \quad (2.17b)$$

$$M_{41} = i\alpha_1 (C_{16}P_1^x + C_{66}P_1^y), M_{42} = i\alpha_2 (C_{16}P_2^x + C_{66}P_2^y)$$

$$M_{43} = i\alpha_3 (C_{16}P_3^x + C_{66}P_3^y), M_{44} = i\alpha_4 (C_{16}P_4^x + C_{66}P_4^y)$$

As the wave propagates in one medium, the amplitude does not change, but the phase changes. In the figure 2.3, the relationship between the phase of the wave at the point **P** and **Q** separated by the distance d is expressed as a matrix as follows.

$$\begin{bmatrix} A_1 \\ A_2 \\ A_3 \\ A_4 \end{bmatrix}_{\mathbf{Q}} = \begin{bmatrix} e^{i\alpha_1 d} & 0 & 0 & 0 \\ 0 & e^{i\alpha_2 d} & 0 & 0 \\ 0 & 0 & e^{i\alpha_3 d} & 0 \\ 0 & 0 & 0 & e^{i\alpha_4 d} \end{bmatrix} \begin{bmatrix} A_1 \\ A_2 \\ A_3 \\ A_4 \end{bmatrix}_{\mathbf{P}} = \mathbf{N} \begin{bmatrix} A_1 \\ A_2 \\ A_3 \\ A_4 \end{bmatrix}_{\mathbf{P}} \quad (2.18)$$

N matrix represents the relationship between amplitude and phase at different points. The **M** and **N** matrices are very important in calculating the transfer matrix and scattering matrix. The transfer matrix is a matrix containing propagation information of a wave with a distance d representing a point **P** and a point **Q**. It is expressed as a linear combination of matrix **M** and matrix **N**, which is as follows.

$$\mathbf{T} = \mathbf{M}\mathbf{N}^{-1} \quad (2.19)$$

And the transfer matrix is used with the velocity and stress matrices as follows.

$$\begin{bmatrix} v_x \\ v_y \\ \sigma_{xx} \\ \sigma_{xy} \end{bmatrix}_{\mathbf{Q}} = \mathbf{T} \begin{bmatrix} v_x \\ v_y \\ \sigma_{xx} \\ \sigma_{xy} \end{bmatrix}_{\mathbf{P}} \quad (2.20)$$

The transfer matrix can be used to express the physical relationship between the point **P** and the point **Q**. Conversely, the transfer matrix can be used to obtain the velocity and stress at any point when the material properties are known. When wave enters into another medium, the boundary condition on the interface is like Eq. (2.13).

$$\begin{bmatrix} v_x \\ v_y \\ \sigma_{xx} \\ \sigma_{xy} \end{bmatrix}_{x=0+} = \begin{bmatrix} v_x \\ v_y \\ \sigma_{xx} \\ \sigma_{xy} \end{bmatrix}_{x=0-} \quad (2.21)$$

On the other hand, in Fig. 2.3, the transfer matrix method can be applied from point **P** to point **R**.

$$\begin{bmatrix} v_x \\ v_y \\ \sigma_{xx} \\ \sigma_{xy} \end{bmatrix}_{\mathbf{R}} = \mathbf{T}_C \mathbf{T}_B \mathbf{T}_A \begin{bmatrix} v_x \\ v_y \\ \sigma_{xx} \\ \sigma_{xy} \end{bmatrix}_{\mathbf{P}} \quad (2.22)$$

Where \mathbf{T}_A , \mathbf{T}_B , \mathbf{T}_C are transfer matrices for materials A, B, and C, respectively. For an isotropic medium and only one wave mode such as longitudinal mode, the transfer matrix is given as

$$\mathbf{T} = \begin{bmatrix} \cos kd & \frac{i}{Z} \sin kd \\ iZ \sin kd & \cos kd \end{bmatrix}, \quad (2.23)$$

where k is the wave number of longitudinal waves, and Z is mechanical impedance of medium.

2.3.2 Scattering Matrix

In this subsection, scattering matrix method, which is very powerful to understand wave propagation similar to the transfer matrix method, is introduced. The transfer matrix uses \mathbf{M} and \mathbf{N} matrices to express the relationship between velocity and stress, whereas the scattering matrix is the amplitude and phase of wave expressed as \mathbf{M} and \mathbf{N} matrices. Using the Eq. (2.16) for the \mathbf{M} matrix and the Eq. (2.20) for the transfer matrix, the scattering matrix is derived.

$$\begin{bmatrix} A_1 \\ A_2 \\ A_3 \\ A_4 \end{bmatrix}_Q = \mathbf{M}^{-1} \begin{bmatrix} v_x \\ v_y \\ \sigma_{xx} \\ \sigma_{xy} \end{bmatrix}_Q = \mathbf{M}^{-1} \mathbf{T} \begin{bmatrix} v_x \\ v_y \\ \sigma_{xx} \\ \sigma_{xy} \end{bmatrix}_P = \mathbf{M}^{-1} \mathbf{T} \mathbf{M} \begin{bmatrix} A_1 \\ A_2 \\ A_3 \\ A_4 \end{bmatrix}_P = \mathbf{S} \begin{bmatrix} A_1 \\ A_2 \\ A_3 \\ A_4 \end{bmatrix}_P \quad (2.24)$$

Scattering matrix \mathbf{S} is written as

$$\mathbf{S} = \mathbf{M}^{-1} \mathbf{T} \mathbf{M}. \quad (2.25)$$

The scattering matrix method is powerful between waves passing through various mediums. As shown in Eq. (2.22), the scattering matrix is defined as follows for the transfer matrix when waves are transmitted in the order of medium A, B, and C.

$$\mathbf{S} = \mathbf{M}_C^{-1} \mathbf{T}_C \mathbf{T}_B \mathbf{T}_A \mathbf{M}_A \quad (2.26)$$

Where \mathbf{M}_A and \mathbf{M}_C are \mathbf{M} matrices of material A and C. Assuming that only longitudinal waves of magnitude 1 are incident in \mathbf{P} , A_j ($j = 1,2,3,4$) satisfies the

following values in order to estimate the transmittance in Fig. 2.3.

$$A_1|_p = 1, A_3|_p = 0, A_2|_Q = A_4|_Q = 0 \quad (2.27)$$

Therefore, the number of remaining variables A_j is 4, and since there are 4 equations, the solution can be obtained. The solution means magnitude and phase of transmitted/reflected waves in the model of Figure 2.3.

2.4 Elastic Wave Propagation in a Periodic Structure

This section reviews the waves in the periodic structure, which is the most important principle in constructing metamaterials. Various previous studies have been conducted on the wave of the periodic structure, and it can be said that metamaterial theory is a basic background theory. The periodic arrangement can make the wave not propagate at a specific frequency, or it can change the speed of the wave at a specific frequency. By applying this, the shape of the periodic structure can be varied, so that the refraction of the wave and even the negative refraction can be realized. In this section, the dispersion curve of the wave is calculated through theoretical analysis in the most basic periodic structure as shown in Fig. 2.4. This is the most basic graph used for metamaterial theory as well as elastic phononic crystal, and it is the most useful method for predicting wave motion.

Figure 2.4 shows the 1-D bi-layered structure. Waves propagate along the positive x -axis, and the periodic structure repeats infinitely. It is assumed that there is a time-harmonic condition for wave propagation. In this case, by using the transfer matrix

and the Bloch-Floquet theorem for the periodic structure, it is possible to find a dispersion relation which is useful for understanding the motion of the wave in the periodic structure. For the unit cell in figure 2.4 (b), the transfer matrix at the left and right interface with periodicity is written as

$$\begin{bmatrix} \vec{v}(x+d) \\ \vec{F}(x+d) \end{bmatrix} = T_b \begin{bmatrix} \vec{v}(x+d_a) \\ \vec{F}(x+d_a) \end{bmatrix} = T_b T_a \begin{bmatrix} \vec{v}(x) \\ \vec{F}(x) \end{bmatrix} = T_{ab} \begin{bmatrix} \vec{v}(x) \\ \vec{F}(x) \end{bmatrix} \quad (2.28)$$

where T_a and T_b are the transfer matrices of material A and B constituting a unit cell. Also, the transfer matrix for an isotropic material is reviewed in 2.3, and the matrix T_{ab} is written as

$$T_{ab} = \begin{bmatrix} \cos \beta_b & \frac{i}{Z_b} \sin \beta_b \\ iZ_b \sin \beta_b & \cos \beta_b \end{bmatrix} \begin{bmatrix} \cos \beta_a & \frac{i}{Z_a} \sin \beta_a \\ iZ_a \sin \beta_a & \cos \beta_a \end{bmatrix} \quad (2.29)$$

where β_i ($i = a, b$) is a dimensionless variable, expressed as the product of k as the wavenumber and d as the distance. With $\beta_i = k_i d_i = \frac{\omega}{c_i} d_i$, β_i means a phase shift in layer i . On the other hand, Bloch-Floquet Theorem, the theory of periodic structure, is written as

$$\begin{bmatrix} \vec{v}(x+d) \\ \vec{F}(x+d) \end{bmatrix} = \lambda \begin{bmatrix} \vec{v}(x) \\ \vec{F}(x) \end{bmatrix} = e^{ikd} \begin{bmatrix} \vec{v}(x) \\ \vec{F}(x) \end{bmatrix} \quad (2.30)$$

where k is effective wave number in the unit cell, and β , called Bloch-phase, is the dimensionless wave number in the unit cell with $\beta = kd$. The dispersion equation of the periodic structure is derived from Eq. (2.28) of the transfer matrix and Eq.

(2.30) of the Bloch-Floquet theorem.

$$\mathbf{T}_{ab} \begin{bmatrix} \vec{v}(x) \\ \vec{F}(x) \end{bmatrix} = \lambda \mathbf{I} \begin{bmatrix} \vec{v}(x) \\ \vec{F}(x) \end{bmatrix}, \quad (2.31)$$

In order for velocity and force to have a non-trivial solution, the characteristic determinant should be 0.

$$\det(\mathbf{T}_{ab} - \lambda \mathbf{I}) = 0 \quad (2.32)$$

The eigenvalue λ , the solution of the equation, is written as

$$\lambda = e^{i\beta} = e^{ikd} = a \pm i\sqrt{1-a^2}. \quad (2.33)$$

Where a is half of the trace of the transfer matrix \mathbf{T}_{ab} ($\text{tr}(\mathbf{T}_{ab}) \triangleq 2a$). From Eq. (2.33), the real and imaginary parts of both sides are as follows.

$$\cos \beta = \cos kd = a \quad (2.34a)$$

$$\sin \beta = \sin kd = \pm \sqrt{1-a^2} \quad (2.34b)$$

Eq. (2.34a) is the dispersion equation analyzed for the wave propagating in the periodic structure. Figure 2.5 shows the dispersion equation of 1D periodic structure.

On the other hand, the value of a can be accurately calculated from the transfer matrix \mathbf{T}_{ab} , and can be expressed as material properties such as the mechanical impedance of material A and B.

$$a = \frac{\cos(\beta_a + \beta_b) - \rho^2 \cos(\beta_a - \beta_b)}{1 - \rho^2}, \quad \rho = \frac{Z_a - Z_b}{Z_a + Z_b} \quad (2.35)$$

Here, since a is a function of frequency ω , the dispersion equation (2.34a) obtained from the periodic structure means the relationship with the effective wavenumber k

and ω .

In Eq. (2.33), if the magnitude of a is greater than 1, then β is not a real number but an imaginary number or a complex number. In this case, the wave does not propagate, and the band gap phenomenon due to the periodic structure occurs. Furthermore, if the magnitude of a is less than 1, then β becomes a real number and a pass band is formed.

In addition, as can be seen in Eq. (2.33), in the dispersion equation, β is in the cosine function. Satisfying the following equation, dispersion curves are periodic in β with a period 2π .

$$\cos(\beta + 2\pi) = \cos \beta = a(\omega) \quad (2.36)$$

When the dispersion relation is analyzed in the range of $-\pi < \beta < \pi$, the dispersion curve can be plotted for all regions by periodicity, and this range is called the first Brillouin zone. For other ranges, it is called the higher Brillouin zone.

In Figure 2.6 (a), structures are periodically arranged in two dimensions instead of one. The unit cell, which is the basis of the periodic structure, is described in figure 2.6 (b). This unit cell can be also analyzed using the Bloch-Floquet Theorem and the transfer matrix method in the direction in which the periodic structure is repeatedly arranged. The dispersion surface obtained through the analysis depends on the direction of the wave vector of the wave. That is, for a periodic structure arranged in two dimensions, the dispersion equation is drawn in three dimensions including k_x - k_y plane and frequency ω -axis as shown in Figure 2.7. This is a very powerful tool

for understanding the wave in the periodic structure because it informs the relationship between the frequency and the wave number in the direction of the wave.

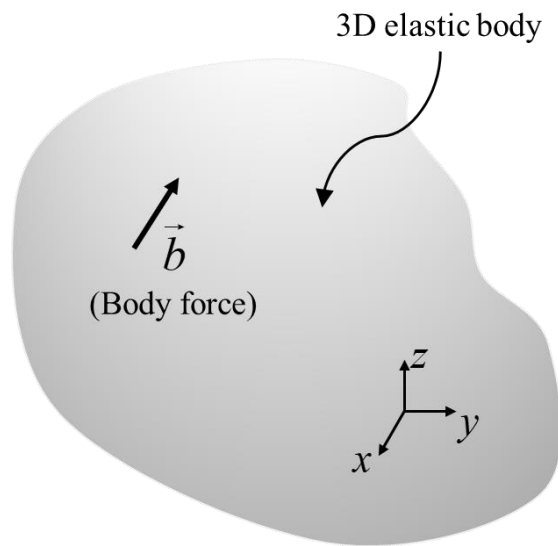


Fig. 2.1 3D elastic body with body force.

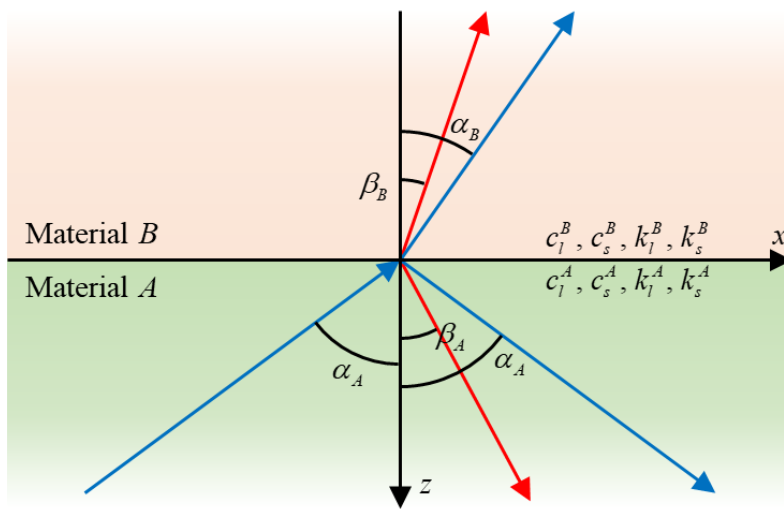


Fig. 2.2 Refraction and reflection of wave which enters from material A to material B.

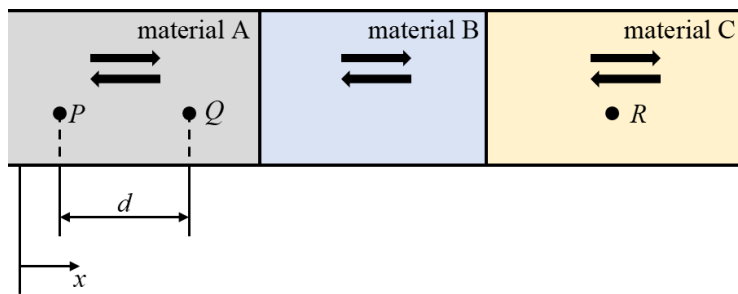


Fig. 2.3 Wave propagation along $+x$ -axis from material A to material C.

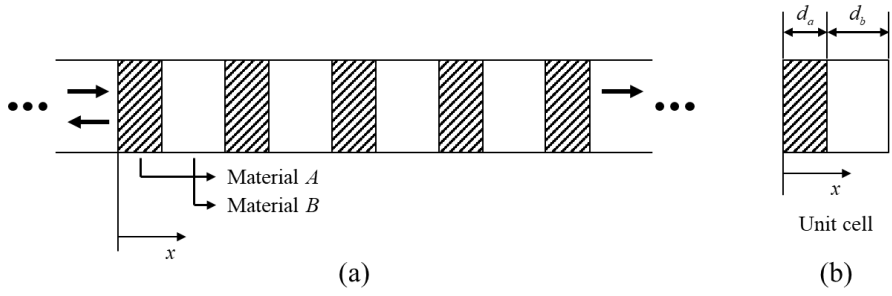


Fig. 2.4 (a) 1-dimensional periodic structure model. (b) The unit cell of the periodic structure.

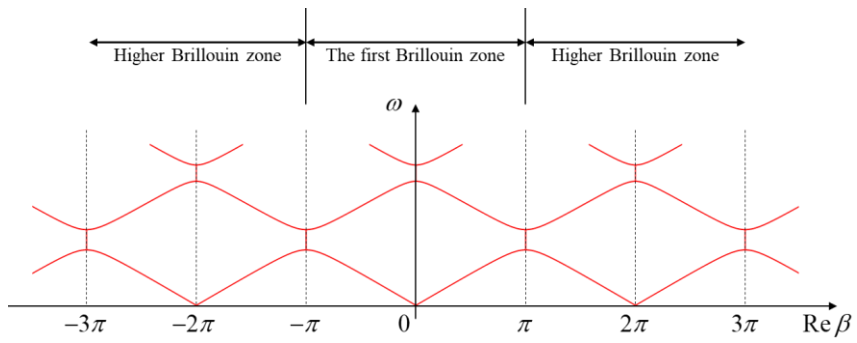


Fig. 2.5 Dispersion relation of the 1D periodic structure.

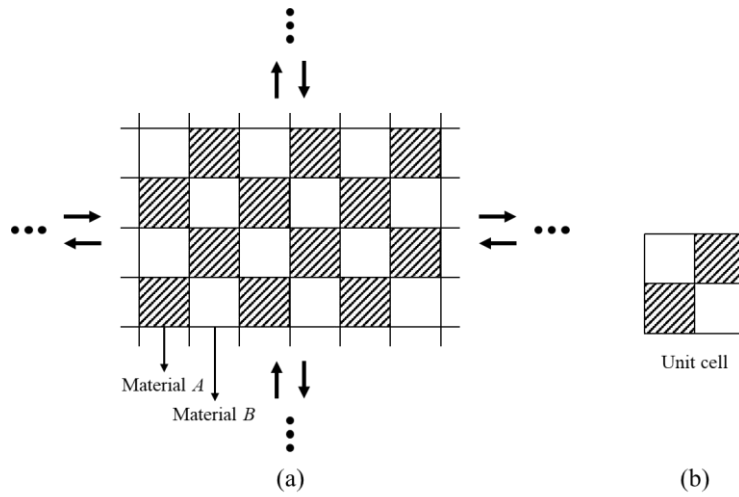


Fig. 2.6 (a) 2-dimensional periodic structure model composed of material A and B. (b) The unit cell of the periodic structure.

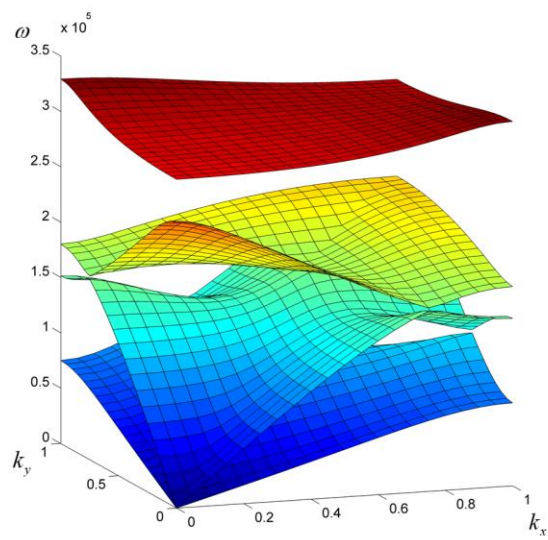


Fig. 2.7 Dispersion surface for the 2-dimensional lattice of the first Brillouin zone. The dispersion surface is symmetric about k_x -axis and k_y -axis.

<CHAPTER 3>

WAVE STEERING

USING EQUI-FREQUENCY CONTOUR

OF ELASTIC PHONONIC CRYSTALS

3.1 Chapter Overview

In this section, we aim to increase the design flexibility and overcome the limitation of existing methods that are confined to only one-directional wave cancellation; we utilize phononic crystals (PCs) to cancel two differently refracted waves that have negative and positive refraction angles, respectively. PCs are artificially designed structures with periodic holes or other substances inserted in their matrices, bringing about extraordinary wave phenomena. Typically, PCs can make band-gaps, negative refraction [4-12] and bi-refraction phenomena [13-18]. Applying these unusual wave phenomena, a few researches on cancelling beams that have multiple incident angles have been reported very recently [19-20]. However, these researches performed only simulation work dealing with fluidic media and there is no further experimental verification in elastic media. Therefore, for the first time, we demonstrate the wave cancellation phenomenon by using PCs in elastic field and confirm the phenomenon

by experiments.

To perform wave cancellation experiments, we use a PC prism embedded in an isotropic plate. Guided by the recent work [21] reporting the splitting of an incident beam into multiple beams, the unit cell of the PC prism is chosen to be a square unit cell made by drilling circular holes in a base isotropic plate. In this study, we will use the multiple beam splitting phenomenon reversely so that multiple beams incident on a PC prism can cancel each other when they exit the PC prism. For the wave cancellation, unlike for the multiple beam splitting, there are important design issues to be considered. We will discuss these issues in details.

Assume that two waves are incident onto the hypotenuse of a selected PC prism (shown in Fig. 3.1) with incident angles of θ_p and θ_n . Obviously, we should select an appropriate frequency (here, 220 kHz for the lowest shear-horizontal (SH0) mode) and a prism angle ($\alpha = 26.57^\circ$, i.e., $\tan \alpha = \frac{1}{2}$) to ensure multiple beam splitting through the PC prism. Apparently, it will be more convenient if the angles of incidence are much different; so, we choose a positive angle of θ_p and a negative angle of θ_n . We will call the incident source beams with θ_p and θ_n by positive and negative source beams, respectively. With these underlying assumptions, the following issues for successful experiments must be addressed. Firstly, θ_p and θ_n should be so chosen as to make the transmitted waves inside the PC prism propagate along the same path with the same direction. Secondly, the two beams

incident into the prism must have the same widths when they exit to the base plate for complete beam cancellation. The beam widths of the incident positive and negative source beams will be denoted by b_p and b_n , respectively. Thirdly, the differences in the phase and amplitudes of the two incident waves should be so tuned as to cancel each other when they exit. One can adjust the amplitudes by adjusting the magnitudes of the input elastic signals to transducers. On the other hand, the phase control can be realized by controlling the distances (d_p , d_n) from the positive and negative beam sources to the target point on the hypotenuse of the PC prism. After presenting the design procedure for the wave cancellation experiment by analysis, the experimental results will be given. As mentioned earlier, the SH0 wave mode at 220 kHz will be used for the present study, as the dispersion analysis on this wave mode at this frequency is readily available in the existing literature [21].

3.2 Elastic Phononic Crystal Prism Model

Figure 3.1 sketches how to realize wave cancellation using two waves incident onto the hypotenuse of a right-angle triangle PC prism ($\tan \alpha = 0.5$) embedded in a base aluminum plate (Young's modulus $E = 70$ GPa, density $\rho = 2700$ kg/m³, Poisson's ratio $\nu = 0.33$, shear wave speed $v_s = 3130$ m/s) of thickness $t = 2$ mm. The PC is made of 8 mm×8 mm square unit cells with circular holes of diameter $d = 6.4$ mm. Two beams incident from the base plate onto the oblique side CD of the

PC prism are denoted by I_p and I_n where the subscripts p and n denote those associated with the positive and negative beam sources. Inside the PC prism, I_p and I_n will turn into transmitted waves T_p and T_n , respectively. Note that in the PC prism, an infinite number of Bloch wave modes form T_p and T_n although they were sketched as if they consisted of single waves in Fig. 3.1. When T_p and T_n exit the PC prism and enter the base plate, they will turn into single waves, O_p and O_n . As mentioned in Chapter Overview, O_p and O_n can cancel each other if the beam sizes, phases, amplitudes and incident angles of I_p and I_n are appropriately tuned.

3.3 Wave Steering Simulation using EFC of Elastic Phononic Crystals

We design incident waves which enter the PC prism for wave steering and wave cancellation. Before determining the beam sizes, phases, amplitudes, and incident angles of I_p and I_n , we must know the dispersion curves and the equi-frequency contours (EFCs) at 220 kHz of the SH0 mode.

3.3.1 Dispersion curve of phononic crystals

As done in Ref. [22], the finite element analysis of the dispersion curve in the first Brillouin zone was performed and the result is shown in Fig. 3.2. It shows that the SH0 wave at 220 kHz has a negative phase velocity, resulting in negative refraction. Other branches correspond to different wave modes (such as symmetric Lamb wave modes that are not used in the present experiment). Because the periodic nature of the Bloch waves in the PC, we need to examine the EFCs not only in the first Brillouin zone but also in higher zones.

There are 2 branches passing through 220 kHz as shown in Fig. 3.2 (a). One branch is utilized in our research and the other branch is irrelevant because this branch belongs to the lowest anti-symmetric Lamb mode (A0 mode) which has out-of-plane dominant motion. Figure 3.2 shows the mode shapes of (b) the branch (SH0 mode) used in our research, of (c) the other branch (A0 mode). The branch passing through “(b)” in Fig. 3.2 (a) corresponds to the SH mode because the unit cell deforms in the x-y plane and the branch passing through “(c)” in Fig. 3.2 (a), to the A0 mode because the unit cell deforms in the z-x plane. Both in the simulation and the experiment, the A0 mode wave was ignored because we only applied in-plane shear force and shear strain; in this case, no A0 mode could be excited.

3.3.2 Design Analysis using EFC

The small black circles in Fig. 3.3 denote the EFCs for the PC at 220 kHz; they are

plotted in the range of $-\frac{3\pi}{a} < k_x < \frac{3\pi}{a}$ and $-\frac{3\pi}{a} < k_y < \frac{3\pi}{a}$ where k_x and k_y denote wavevector components in the x and y directions. On the other hand, the large blue circle centered at $(k_x, k_y) = (0, 0)$ represents the EFC for the base aluminum plate.

Now, let us explain how to determine θ_p and θ_n , the incidence angles of the source waves I_p and I_n . The key equation to find θ_p and θ_n is from the Snell-Descartes law requiring that the tangential wavevector components on the interface of two dissimilar media must be continuous, i.e.,

$$k_{\tan}^{\text{incident}} = k_{\tan}^{\text{transmitted}} \quad (3.1)$$

For the exiting waves (O_p and O_n) from the PC to the base plate to cancel each other, they must propagate along the same direction. Here, we choose the negative y direction as the propagation direction. In this case, we can identify the wave components (marked by T 's) inside the PC which can turn into O_p and O_n when they exit the PC. The point corresponding to O_p and O_n in the EFC of the aluminum plate at 220 kHz is marked by a symbol "O". The direction of the arrow at "O" indicates the negative y direction, which is the propagation direction of the wave. Actually, it is the group velocity direction that is normal to the EFC at the point.

To find T 's in EFCs of Fig. 3.3, a vertical line passing through "O" is first drawn;

along this line, Eq. (3.1) can be satisfied. There are three possible T 's marked by T_4 , T_5 , and T_6 . Because the SH0 wave in the PC has the negative phase velocity, some care must be taken in selecting the correct locations of T 's in the EFCs, as given here. Other possible T 's are marked by $T_1 - T_3$, and $T_7 - T_9$ resulting from the periodic nature of the Bloch waves in the PC; they can be similarly identified by drawing vertical lines that are displaced by $\pm n\pi / a$ (n : integer). (In fact, there are an infinite number of T 's but only those that can interact with the EFC of the base aluminum plate are shown in Fig. 3.3.)

To find I_p and I_n generating some of these T 's, we consider the conservation law (Eq. (3.1)) along CD, which is the interface between the PC prism and the base plate when waves are incident upon the hypotenuse of the PC prism. The conservation lines of the tangential wavevector component are the dotted lines making the angle of $\frac{\pi}{2} - \alpha$. There are three feasible points (Q_1 , Q_2 , and Q_3) on the EFC of the base plate that overlap with the dotted lines, and we select only two points; Q_1 and Q_2 . The propagation directions of the incident waves at Q_1 and Q_2 are the group velocity directions. At Q_1 and Q_2 , one can determine the positive (θ_p) and negative (θ_n) angles of incidence, respectively. In the present case, it is found that $\theta_p = 42.2^\circ$ and $\theta_n = 7.8^\circ$.

3.3.3 Verification of the EFC analysis by time-transient simulations

We designed the refracted wave to propagate in the $-y$ direction by the EFC analysis. According to the EFC analysis, the refracted wave is formed along the $-y$ direction immediately after the incident beam enters the PC. Figure 3.4 shows the time transient simulations, which explains the cancellation phenomenon in detail. Figure 3.4 shows the propagation of (a) a positive source and (b) a negative source over time. It can be clearly seen that the refracted wave propagates in the $-y$ direction immediately after the incident beam enters the PC.

3.4 Wave Cancellation of two waves through a Phononic Crystal Prism

3.4.1 Calculate the widths of the incident source beams

Now, we should determine the widths of the incident source beams. Note that once the incident waves are transmitted into the PC, they must propagate along the negative y direction. Because the beam widths of the transmitted waves must be the same for wave cancellation, the incident waves must satisfy the following geometric condition:

$$\frac{b_p}{\cos \theta_p} = \frac{b_n}{\cos \theta_n} = \frac{b}{\cos \alpha} \quad (3.2)$$

where b is the beam width of O_p and O_n . We selected $b = 4$ cm so that $b_p = 3.3$ cm and $b_n = 4.4$ cm. The widths b_p and b_n will be controlled in the

experiment when designing the transducers generating the desired wave sources.

3.4.2 Calculate the phases of the incident source beams

Finally, the phase difference between I_p and I_n required for wave cancellation can be controlled by adjusting the distances (d_p , d_n) between the sources to the target point on the hypotenuse on the PC prism. If the magnitude of the wavevector along the incidence direction is denoted by k , the phase difference ϕ_{diff} between I_p and I_n when they arrive at the target point on the hypotenuse on the PC prism becomes

$$k|d_p - d_n| = \frac{2\pi f}{v_s}|d_p - d_n| = \phi_{diff} \quad (3.3)$$

where f is the excitation frequency. If $\phi_{diff} = (2n - 1)\pi$ (n : integer), the two incident waves have different signs, possibly cancelling each other. By choosing $n = 1$ in Eq. (3.3), the following values are determined: $d_p = 18.696\text{cm}$ and $d_n = 17.985\text{cm}$.

3.4.3 Numerical Simulation Verification

Before carrying out actual experiments, we performed numerical simulations of wave cancellation first by using the determined values of (θ_p , b_p , d_p , θ_n , b_n , d_n). COMSOL Multiphysics [23] was used for the simulations under the plane stress

condition. To ensure the unidirectional wave propagation, 4 excitation lines were used to form the wave source. Shear-horizontal waves can be generated from the source if time-harmonic forces tangential to the source lines are used. When the same tangential force was applied to each source, the obtained output ratio for positive and negative refraction was 3.5986:3.7720. In other words, when the magnitude of each source is inversely tuned to exhibit the same output value, complete wave cancellation can occur. Accordingly, we applied the line loads of strength equal to 3.772 N/m and 3.5986 N/m for the positive and negative sources, respectively.

Figure 3.5 and 3.6 show the wave simulation results. The plane stress condition is used for wave propagation simulation because the base plate is very thin. Figure 3.5 shows time-harmonic simulation to see the entire cancellation. When the positive and negative sources are incident alone on the PC prism, the results are shown in Fig. 3.5 (a) and (b), respectively. The color level denotes the magnitude of the displacement component of the shear-horizontal waves. Figure 3.5 (c) shows the result for the simultaneous incidences of the two wave sources with adjusted magnitudes given above. Compared with Figs. 3.5 (a,b), Fig. 3.5 (c) shows that the exiting wave from the PC is vanishingly small. This confirms the validity of our design for the wave cancellation. Figure 3.6 shows time transient simulation to ascertain this phenomenon and the graphs shown in Fig. 3.6 mean the displacements of the waves along the red line in the simulation over time. The red line is located at $x = 0$ and it is 7 cm long in the y -direction. We extracted the shear displacement data from the simulation. As shown in Fig. 3.6, it can be confirmed that the cancellation

occurs immediately after the waves exit the PC structure.

3.5 Experimental Validation

The experimental setup for verifying the feasibility of wave cancellation is presented in Fig. 3.7 (a). The PC prism is fabricated by the designed parameters and condition. To realize experimentally the wave cancellation phenomenon designed by the numerical simulation and analysis, the two incident beams must have good directivity and mode tunability. To fulfil this condition, we used PSA-OPMTs (planar solenoid array-type orientation adjustable patch-type magnetostrictive transducers) that are capable of the aforementioned conditions [24].

As shown in the inset of Fig. 3.7 (a), the PSA-OPMT consists of a pair of permanent magnets and solenoids. The gap between the solenoids is set to be 7 mm, which is about half of the wavelength, for good beam directivity. To generate the SH0 wave along the y axis, dynamic magnetic field induced by solenoids and static magnetic field by permanent magnets must be perpendicular to each other [24, 25]. Specifically, when the electric signal entering the transducer is converted to the properly designed magnetic field, a desired wave mode can be generated due to changes in strain induced by the magnetostrictive effect of nickel patch. The width of each nickel patch is the same as that of positive and negative sources. Therefore, the patch sizes are 3.3 cm \times 2.5 cm and 4.4 cm \times 2.5 cm for positive and negative sources, respectively. Also, by using the same PSA-OPMT, we can measure the SH0 mode wave by the reverse mechanism mentioned above [25].

For generation and measurement of SH0 waves in the PC prism embedded in an aluminum plate, we used total of three PSA-OPMTs. The experimental setup with two generating transducers and one receiving transducer is shown in Fig. 3.7 (a). This setup is suitable for controlling the phase and amplitudes of the incident waves. The basic principle of this experiment is explained as follows. The electric signal generated by a function generator (Agilent 33220A) is amplified by a power amplifier (AG 1017L) and then sent to the transducers for ultrasonic wave generation. For the measurement, the transmitted wave is converted into an electric signal by a transducer receiver, and this signal is measured by an oscilloscope (LeCroy WaveRunner 620Zi) after being amplified by a pre-amplifier (SR560 low-noise pre-amplifier). Here, we utilized a modulated Gabor pulse (see, e.g., [26]) as the input pulse because of its good frequency localization.

Now let us explain the details of the experimental procedures. To generate two waves that have different amplitudes but the same phase, we used a T-connector to divide a signal from the function generator into two same signals. Each signal is amplified by a different power amplifier to actively control the voltage of electric signals entering each transducer. The main reason of independent tuning is that the magnitude of the actual emitted wave can be highly sensitive due to several parameters (i.e., patch characteristics, couplant condition, and different transducers performance) that disturb accurate performance of transducers. In other words, by independently tuning the voltage for each transducer, the magnitude of the actually generated elastic wave can be actively manipulated.

We first located and fixed the source transducers to satisfy the out-of-phase condition that were derived from the numerical analysis ($d_p = 18.696\text{cm}$, $d_n = 17.985\text{cm}$). Here, by actively manipulating the magnitudes (by the aforementioned method with two independent power amplifiers) of each incident wave, the refracted beams can have the same magnitude (shown in Fig. 3.7 (b)) for wave cancellation. Specifically, the raw data for the positive (negative) sources shown in Fig. 3.7 (b) were obtained when only the left (right) source was turned on. When both sources were turned on, the waves were successfully cancelled as shown in the last plot of Fig. 3.7 (b). There are some wiggles at the front and the rear of the wave in experiment. They appeared because of slight distortion of the waveform that originates from the internal wave reflection within the magnetostrictive patch [27]. Geometrical errors from fabrication of the phononic crystal prism are also responsible for the presence of the wiggles.

With the same setup for the 3 cases (when only positive source, only negative source, and both sources are turned on), we measured total of 15 points for the verification of the wave cancellation. The measurement points are at least $H = 13\text{ cm}$ away from the center of the hypotenuse of the PC prism, and make up a rectangular shape. The area that the measurement points cover is ($h = 3\text{ cm}$) \times ($s = 1\text{ cm}$). We measured 15 points for the 3 cases that are the same with simulation (using positive source, negative source, and both sources).

Figure 3.7 (b) presents the raw data for the 3 cases at the red point ($x = 0$, $y = h$) shown in Fig. 3.7 (a). Here, the peak-to-peak value of the measured signal by using

both input sources is decreased almost by half compared with that by using only one input source. For more accurate analysis on the raw data, we used the short-time-Fourier-transforms (STFT) method. The STFT values at the arrival time, which is $120 \mu\text{s}$, were extracted and are shown in Fig. 3.8 (b), which is compared with the simulation result in Fig. 3.8 (a).

Figure 3.8 (b) presents the contours of results from STFT of the experiment data and Fig. 3.8 (a), the amplitude value from simulation having the same axis as in Fig. 3.7 (a). If we compare the amount of decrease numerically, when two sources are turned on, the magnitudes of the refracted waves decreased about 64% at the red point ($x = 0, y = h$) of Fig. 3.7 (a) in the simulation, and about 65% at the same point in the experiment. Consequently, the wave cancellation phenomenon is verified as demonstrated in Fig. 3.8, and also confirmed that the phenomenon can occur at a wide range instead of a narrow range.

3.6 Summary

Through this study, we reported the first experimental result of the elastic wave cancellation using the phononic crystal prism embedded in a thin aluminum plate. Two elastic wave sources of 220 kHz generating the lowest shear-horizontal wave mode were used for the experiment, one of which was incident onto the PC prism with a positive incidence angle while the other, with a negative incidence angle. The procedure to select key design parameters such as the incidence angle, phase differences and beam widths was presented and its validity was checked by

numerical simulations and experiments. Although the present work was mainly concerned with the demonstration of wave cancellation with two wave sources, the results from this study may be used in some applications, such as the cancellation of ultrasonic (guided) waves when one of doubly excited wave modes exists above the cutoff frequency and should be eliminated.

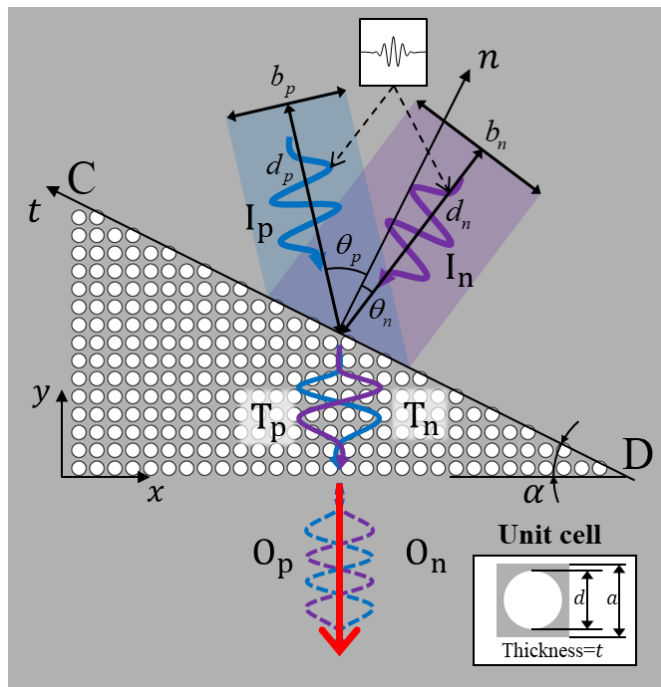


Fig. 3.1 A schematic configuration to verify wave cancellation phenomenon with an elastic phononic crystal.

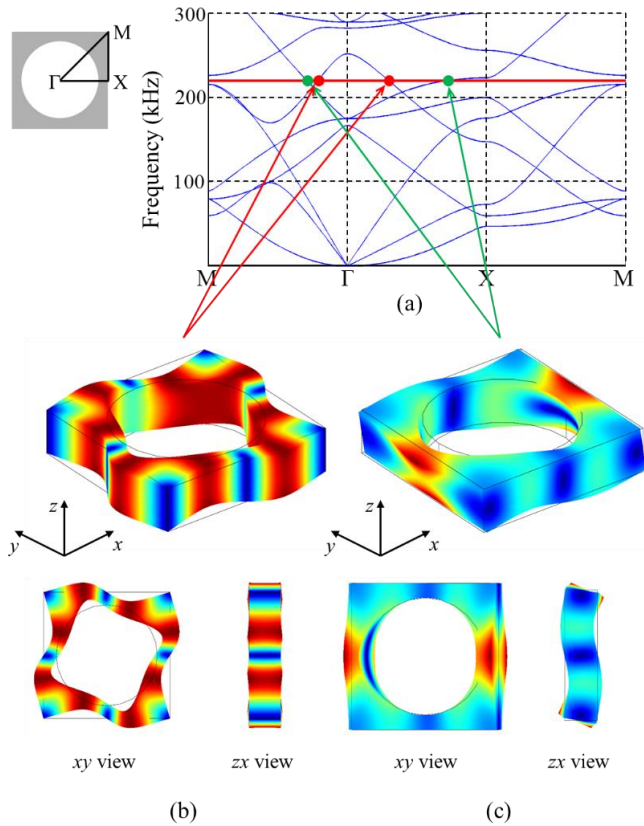


Fig. 3.2 (a) Dispersion curves of utilized PC structure, (b) the mode shape of the branch(SH0 mode) used in our research with red points of dispersion curves, (c) the mode shape of the other branch (A0 mode) with green points of dispersion curves.

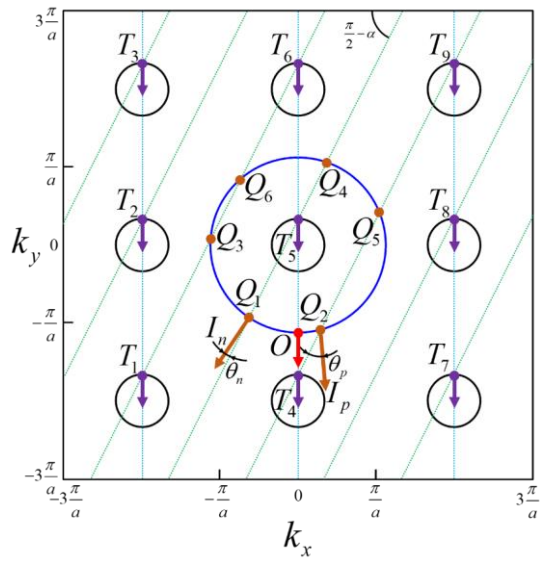


Fig. 3.3 Analysis of the refraction mechanism by using EFCs.

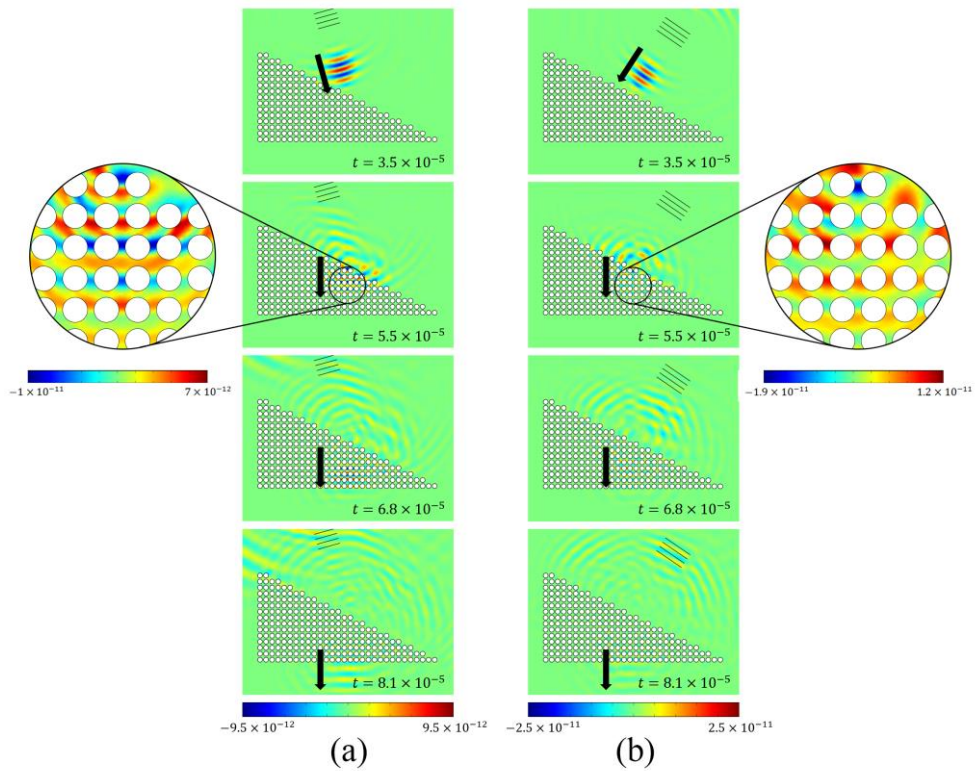


Fig. 3.4 The snapshots of wave field by (a) positive source and (b) of negative source at different time steps. (The color level denotes the magnitude of the displacement field.)

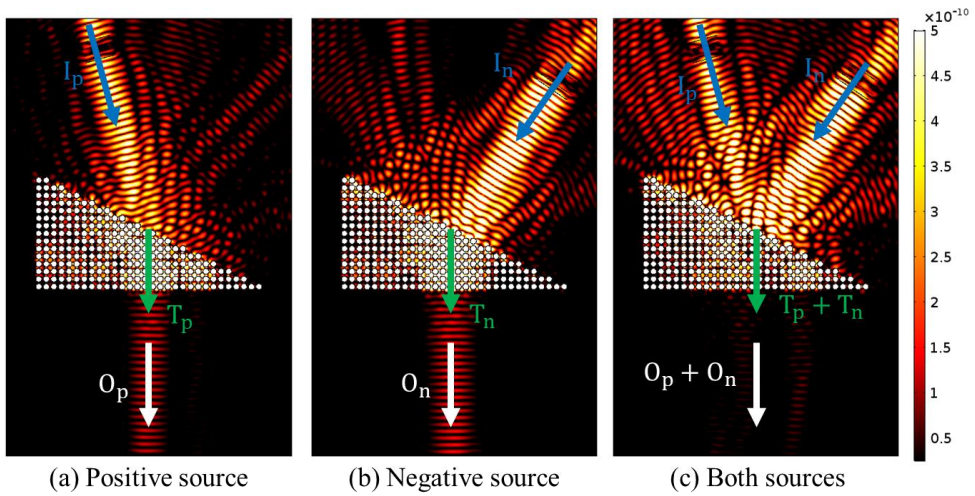


Fig. 3.5 Shear displacement plot time-harmonic simulation for (a) positive, (b) negative and (c) both sources.

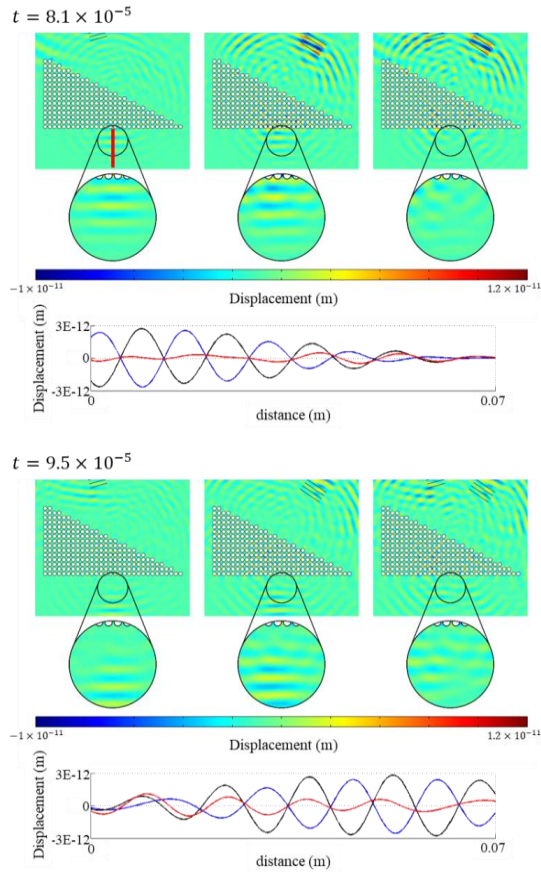


Fig. 3.6 Time transient simulation of the displacement component yielding shear stress for each case and displacements of refracted waves (blue line: positive, black line: negative and red line: both sources) along the red line in the simulation. The red line is located at $x = 0$ and it is 7 cm long in the y -direction. (For interpretation of the references to colour in this figure legend, the reader is referred to the web version of this article.)

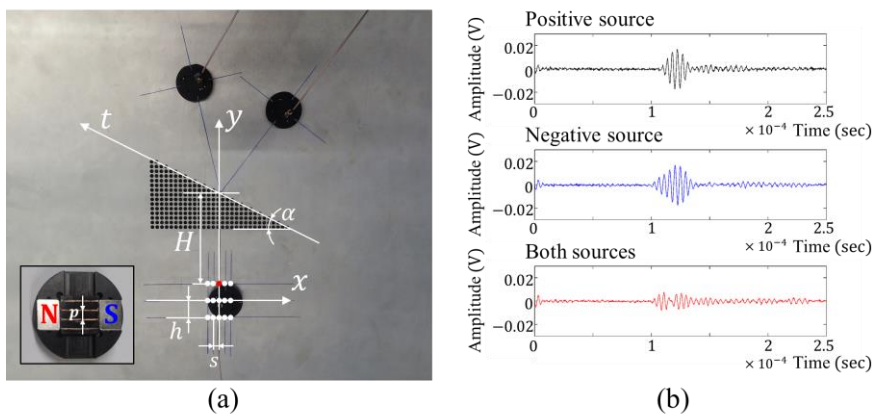


Fig. 3.7 (a) The experimental setup and a PSA-OPMT configuration. (b) Raw data for 3 cases at the red point in Fig. 3.7 (a).

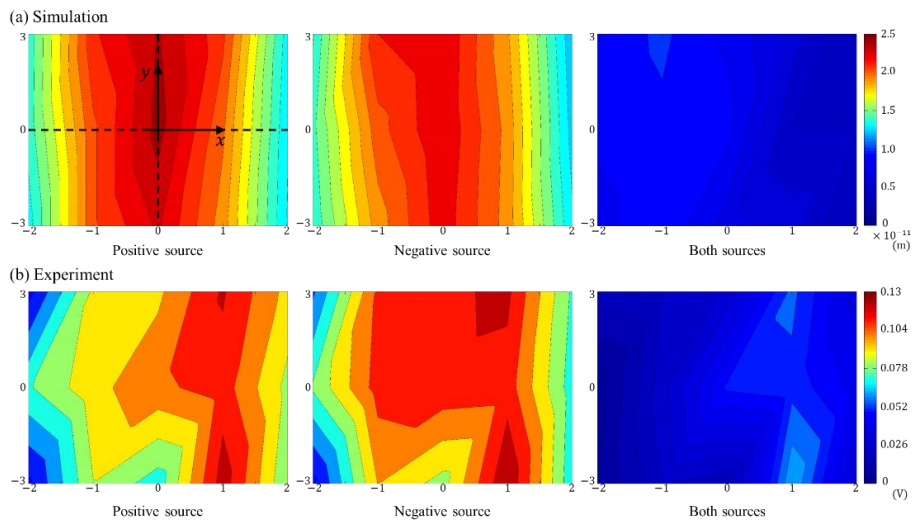


Fig. 3.8 Contour plots of acquired data obtained from (a) the numerical simulation and (b) the experiments.

<CHAPTER 4>

MONOLAYER FULL-TRANSMISSIVE ELASTIC METASURFACES WITH PERFECT MODE CONTROL

4.1 Chapter Overview

In this chapter, we use metasurfaces as a way to control the direction of waves. A metasurface is a metamaterial structure that deflects transmitted waves or reflected waves through a phased array of target transmitted waves or reflected waves, and has been studied in various wave fields such as not only elastics but also electromagnetics and acoustics. In addition, there is an advantage in that a variety of applications such as metalenses that focus transmitted waves or reflected waves at one point is possible by various phased arrays properly.

Metasurfaces have a special point in elastics because, unlike other wave fields such as electromagnetics and acoustics, there are several wave modes in elastics. Since several wave modes are dependent on each other, even if the elastic metasurface is designed for a single target mode, unintended waves of the target mode transmit or reflect, resulting in a decrease in transmittance or reflectance of the target mode.

Previously, there were metasurface studies for elastic metasurfaces, but some of these studies considered elastic multiple modes, but most of them did not consider multiple modes. Metasurfaces designed for a single mode propagate waves of different modes. There is also a study on the mode conversion metasurface, but energy efficiency is low because the principle is not direct mode conversion, but indirect mode conversion. Therefore, in these studies, it can be said that the energy efficiency of the target transmitted wave or reflected wave is inferior regardless of mode conversion and mode conservation.

In this study, we intend to design metasurfaces that considers multiple modes at the same time. Accordingly, we intend to design metasurfaces that performs mode conversion and metasurfaces that performs mode conservation as shown in Fig. 4.1. Unlike previous studies, each unit cell of metasurfaces is designed directly that performs a mode conversion or mode conservation, and performs phase controlling at the same time. The mode conversion and mode conservation metasurfaces implemented as a result is characterized in that it is more energy efficient.

First, a method capable of controlling the phase with high energy efficiency is theoretically calculated using effective material properties and transfer matrix method. Then, according to the theory, the unit cells are designed through shape optimization design, and various metasurfaces are designed using the designed unit cells. Finally, the performance of the designed metasurface is verified through theoretical analysis, numerical simulation, and experiment.

4.2 Research Background: Generalized Snell's Law for Multi-Mode waves in Elastic Metasurfaces

Metasurfaces can be designed for phase gradients according to the generalized Snell's Law (GSL). However, since commonly known GSL is described for the same medium and the same wave mode, the generalized Snell's law for multi-mode waves has not been derived for the mode conversion metasurface where the speed of the wave on both sides of the metasurface is different. The method of deriving the generalized Snell's law is to approach the wavefront of the wave with respect to the wave entering and passing through the metasurface as shown in Fig. 4.2. In Figure 4.2, the velocity of the wave in material 1 is c_1 , the velocity of the wave in the material 2 is c_2 , and the velocity in the metasurface is $c(x)$. When the width of the wave incident on the metasurface is L , and the incident angle and the refraction angle are θ_i , θ_r , the transmission time from the wavefront A-A' to the wavefront B-B' of the wave incident along the purple line is as follows.

$$t(x) = \frac{\left(\frac{L}{2} + x\right) \sin \theta_i}{c_1} + \frac{d}{c(x)} + \frac{\left(\frac{L}{2} - x\right) \sin \theta_r}{c_2} \quad (4.1)$$

The phase can be calculated depending on the speed of the wave in the metasurface and the thickness of the metasurface. The elapsed time $t(x)$ from wavefront A-A' to wavefront B-B' has a constant value regardless of the incident position x , and can be applied to the red lines at both ends as well.

$$t\left(\frac{L}{2}\right) = t\left(-\frac{L}{2}\right) \quad (4.2)$$

Meanwhile, it is possible to induce a phase through the speed and path inside the metasurfaces, and the relational expression is as follows.

$$\phi(x) = \omega \frac{d}{c(x)} \quad (4.3)$$

Since the phase and velocity arrangement are uniform inside the metasurfaces, the average slope of the phase and the instantaneous slope coincide. Using the above points, the GSL can be derived concisely.

$$\frac{1}{c_2} \sin \theta_{r2} = \frac{1}{c_1} \sin \theta_{i1} + \frac{1}{\omega} \frac{\partial \Phi}{\partial x} \quad (4.4)$$

Therefore, the GSL for mode conservation and the GSL for mode conversion can be summarized as follows.

$$\text{L to L: } \sin \theta_{rL} = \sin \theta_{iL} + \frac{1}{k_L} \frac{\partial \Phi_L}{\partial x} \quad (4.5a)$$

$$\text{L to S: } \sin \theta_{rS} = \frac{c_S}{c_L} \sin \theta_{iL} + \frac{1}{k_S} \frac{\partial \Phi_S}{\partial x} \quad (4.5b)$$

$$\text{S to S: } \sin \theta_{rS} = \sin \theta_{iS} + \frac{1}{k_S} \frac{\partial \Phi_S}{\partial x} \quad (4.5c)$$

$$\text{S to L: } \sin \theta_{rL} = \frac{c_L}{c_S} \sin \theta_{iS} + \frac{1}{k_S} \frac{\partial \Phi_S}{\partial x} \quad (4.5d)$$

Where L is longitudinal wave mode, S is shear wave mode. The subscript of the angle θ , i , means incidence, r means refraction. The contents in the left side of the

equation mean the various situation of mode conservation and conversion. For example, L to S means the generalized Snell's law when the mode is converted from a longitudinal wave to a shear wave. This expands the existing GSL theory and summarizes the GSL theory for various modes.

4.3 Research Background: Lens Equation for Mode-converting metalens

As summarized in 4.2, in addition to GSL for refracting the direction of the wave in the desired direction, various wave phenomena can be created through the phase arrangement. As a representative example, there is a lens phenomenon in which waves converge into one point, and in this section, we intend to derive a phase arrangement equation to create a lens phenomenon. The overall derivation method is similar to the GSL for multi-mode waves derived in 4.2, but the detailed equation is different because the phenomenon is different. As shown in Figure 4.3, when the focal length is a distance p from the metasurface, the time taken along the purple line from the wavefront A-A' is as follows.

$$t(x) = \frac{\left(\frac{L}{2} + x\right) \sin \theta_i}{c_1} + \frac{d}{c(x)} + \frac{\sqrt{x^2 + p^2}}{c_2} \quad (4.6)$$

This equation is summarized using Eq. (4.2) and Eq. (4.3) as in 4.2, and the following phased array equation can be obtained. Unlike metasurfaces that create a constant phase gradient and describe GSL, which is the relationship between the angle of

incidence and the angle of refraction, in the metalens, the phase arrangement equation for creating a lens effect in which waves are collected at a desired focal length is directly described and is as follows.

$$\phi(x) = k_2 \left(p - \sqrt{x^2 + p^2} \right) \quad (4.7)$$

4.4 Amplitude and Phase of Transmitted Wave through an Anisotropic Material Layer

We approach using the concept of effective material and transfer matrix in anisotropic materials to see if there is a way to control the phase shift in the mode conversion theory. In the original effective material, consider a C tensor containing 6 by 6, a total of 36 C_{ij} 's. However, if you approach only longitudinal and shear waves in one dimension as shown in Fig. 4.4 (a), you do not need to pay attention except for waves propagating along the x -axis, so you can reduce many variables and access them more simply. Therefore, i and j exist only 1 and 6, and can be viewed as a C tensor with three variables of C_{11} , C_{16} ($=C_{61}$), and C_{66} . If the expression is described using the transfer matrix in Fig. 4.4 (a) without considering the background material, it is as follows.

$$\begin{bmatrix} u \\ v \\ \sigma_{xx} \\ \sigma_{xy} \end{bmatrix}_{x=L} = \mathbf{T}_{meta} \begin{bmatrix} u \\ v \\ \sigma_{xx} \\ \sigma_{xy} \end{bmatrix}_{x=0} \quad (4.8)$$

In the above equation, \mathbf{T}_{meta} is the transfer matrix for the anisotropic metamaterial designed. Also, as in 2.4, each transfer matrix can be divided into an \mathbf{M} matrix representing the relationship between the amplitude of the wave, the displacement of the medium, and the stress, and an \mathbf{N} matrix representing the phase shift depending on the propagation of the wave. Using the Scattering matrix ($\mathbf{S} = \mathbf{M}^{-1}\mathbf{T}\mathbf{M}$), the equation shown in the case of Fig. 4.4 (a) is summarized as follows.

$$\begin{bmatrix} A_{longi}^{trans} \\ 0 \\ A_{shear}^{trans} \\ 0 \end{bmatrix} = \mathbf{S}_{meta} \begin{bmatrix} A_{longi}^{inc} \\ A_{longi}^{ret} \\ A_{shear}^{inc} \\ A_{shear}^{ref} \end{bmatrix} = \mathbf{M}_{al}^{-1} \mathbf{T}_{meta} \mathbf{M}_{al} \begin{bmatrix} A_{longi}^{inc} \\ A_{longi}^{ret} \\ A_{shear}^{inc} \\ A_{shear}^{ref} \end{bmatrix} \quad (4.9)$$

Using the above equation, a condition for mode conversion or a condition for mode preservation while the transmittance becomes 1 is derived. In order to have a transmittance of 100%, a reflectance of 0% is used according to the energy conservation law. Since the mode conversion phenomenon was previously revealed by quarter-wave impedance matching, in the mode conversion metasurface, the principle of the phase shift is found through the mode conversion condition. In the mode conservation metasurface, we derive the condition for mode conservation using transfer matrix method, and then find the principle of phase shift in mode conservation.

4.5 Design a Mode-converting Metasurface

Our study is to design a non-resonant single-layer metasurface that controls the

angles while changing modes for waves of two different modes, longitudinal and shear waves, as described above. The design of the metasurface requires the design of the elements constituting the metasurface, that is, the design of a unit cell that can control the phase shift, and the phase arrangement according to the generalized Snell's law.

Figure 4.5 is mode conversion designed metamaterial model for shape optimization. As shown in the figure, the metamaterial is designed as a monolayer. If a periodic structure repeated several times in the x direction is used, the size of the effective medium is determined by the periodicity in the analysis of the effective physical properties of the designed metamaterial structure. However, since monolayer metamaterials do not have periodicity in the x direction, the size of the effective medium and design area of the monolayer metamaterial may differ from each other. [119] In order to design the metasurface, we control the phase by designing metamaterials with different effective medium sizes while having a certain design area using a monolayer unit cell.

4.5.1 Phase control condition with mode-conversion

In this section, we theoretically approach which variable should be controlled to control the phase in the mode conversion phenomenon. Since the conditions for the mode conversion phenomenon have been previously suggested, unlike the scattering matrix equation established in 4.4, the transfer matrix equation in consideration of the background material in Figure 4.4 (b) is as follows.

$$\begin{bmatrix} u \\ v \\ \sigma_{xx} \\ \sigma_{xy} \end{bmatrix}_{x=d} = \mathbf{T}_1 \mathbf{T}_{meta} \mathbf{T}_2 \begin{bmatrix} u \\ v \\ \sigma_{xx} \\ \sigma_{xy} \end{bmatrix}_{x=0} \quad (4.10)$$

In the above equation, \mathbf{T}_1 and \mathbf{T}_2 are the transfer matrices for the background material (=Aluminum) on the right and left of the metamaterial area, respectively, and the transfer matrix for the anisotropic metamaterial designed by \mathbf{T}_{meta} . Each transfer matrix can be divided into a \mathbf{M} matrix representing the relationship between the amplitude of the wave, the displacement of the medium, and the stress, and a \mathbf{N} matrix representing the phase shift depending on the propagation of the wave. The equations for matrix \mathbf{M} and matrix \mathbf{N} are described in the theoretical background, and using $\mathbf{T} = \mathbf{M}\mathbf{N}\mathbf{M}^{-1}$, the equation shown in the case of Figure 4.4 (b) is summarized as follows.

$$\mathbf{M}_{al} \begin{bmatrix} A_{longi}^{trans} \\ 0 \\ A_{shear}^{trans} \\ 0 \end{bmatrix} = \mathbf{M}_{al} \mathbf{N}_{al}^{right} \mathbf{M}_{al}^{-1} \mathbf{T}_{meta} \mathbf{M}_{al} \mathbf{N}_{al}^{left} \mathbf{M}_{al}^{-1} \mathbf{M}_{al} \begin{bmatrix} A_{longi}^{inc} \\ A_{longi}^{ret} \\ A_{shear}^{inc} \\ A_{shear}^{ref} \end{bmatrix} \quad (4.11)$$

Here, \mathbf{M}_{al} is the \mathbf{M} matrix of aluminum as the background material, and \mathbf{N}_{right} and \mathbf{N}_{left} are the \mathbf{N} matrices described on the right and left of the effective medium, respectively. A is the amplitude, and is divided depending on the incident, reflection, and transmission of the longitudinal wave and the shear wave. The above equation can be simplified by using scattering matrix ($\mathbf{S} = \mathbf{M}^{-1}\mathbf{T}\mathbf{M}$).

$$\begin{bmatrix} A_{longi}^{trans} \\ 0 \\ A_{shear}^{trans} \\ 0 \end{bmatrix} = \mathbf{N}_{al}^{right} \mathbf{S}_{meta} \mathbf{N}_{al}^{left} \begin{bmatrix} A_{longi}^{inc} \\ A_{longi}^{ret} \\ A_{shear}^{inc} \\ A_{shear}^{ref} \end{bmatrix} \quad (4.12)$$

Meanwhile, according to Ref. [117], the condition of the mode conversion phenomenon applies the quarter-wave impedance matching mode-converting condition previously studied, and the conditions are as follows.

1. $d = n_{FS} \frac{\lambda_{FS}}{4}$, $d = n_{SS} \frac{\lambda_{SS}}{4}$, $\frac{n_{SS}}{2} - \frac{n_{FS}}{2} = \text{odd}$
2. $C_{11} = C_{66}$
3. $\rho_0 \sqrt{C_{11}^0 C_{66}^0} = \rho \sqrt{C_{11} C_{66} - C_{16}^2}$ (Bimodal impedance matching condition)
4. $C_{16} / C_{11} \rightarrow 0$

Using the above conditions, it is possible to calculate \mathbf{S}_{meta} , which is the scattering matrix of the metamaterial region for mode conversion. The scattering matrix of the metamaterial that satisfies the mode conversion condition is as follows.

$$\mathbf{S}_{meta} = j\rho c_l \begin{bmatrix} 0 & 0 & \frac{1}{\rho_0 c_l^0} & 0 \\ 0 & 0 & 0 & -\frac{1}{\rho_0 c_l^0} \\ \frac{1}{\rho_0 c_s^0} & 0 & 0 & 0 \\ 0 & -\frac{1}{\rho_0 c_s^0} & 0 & 0 \end{bmatrix} \quad (4.13)$$

Where ρ is density of metamaterial, c_l is velocity of longitudinal wave in metamaterial, ρ_0 is density of background material, c_l^0 is velocity of longitudinal wave in background material, and c_s^0 is velocity of shear wave in background material.

The scattering matrix of the metamaterial for mode conversion is substituted into the transfer matrix, and amplitude values of incident and reflected waves can be determined in a mode conversion situation in which a longitudinal wave is incident and transformed into a shear wave at the same time. Therefore, when $A_{longi}^{inc} = 1$ and the other A 's are 0, the amplitude and phase of the transmitted wave can be calculated.

$$A_{longi}^{trans} = 0, A_{shear}^{trans} = j \frac{\rho c_l}{\rho_0 c_s^0} e^{j(k_l^0 b + k_s^0 a)} \quad (4.14)$$

Here, k_l^0 is the wavenumber of longitudinal wave in the background medium, and k_s^0 is the wavenumber of shear wave in the background medium. The phase of the shear mode transmitted wave, which is the mode-converted wave, can be calculated, and the phase is as follows.

$$\phi = k_l^0 b + k_s^0 a + \frac{\pi}{2} = k_l^0 d - (k_l^0 - k_s^0) L_0 + \frac{\pi}{2} - \frac{(k_l^0 + k_s^0)}{2} L \propto L \quad (4.15)$$

It can be seen that the phase of the shear mode transmitted wave transformed in this way is not related to the material properties of the metamaterial, and is linearly proportional only to the size.

4.5.2 Design of Phase-controlling Unit Cells with Mode-conversion

Using the phase shift equation derived in 4.5.1, the difference in the size of the effective medium for designing two monolayer anisotropic metamaterials with the desired phase difference can be obtained. In this study, when the background material is aluminum and target frequency is 100 kHz, the size difference for 90° phase difference is as follows.

$$\Delta L = \frac{2}{k_l^0 + k_s^0} \Delta\phi = \frac{\pi}{k_l^0 + k_s^0} \approx 0.01 \text{ m} \quad (4.16)$$

Since the difference in the size of the effective medium is determined, if the size of the effective medium of one model is determined, the size of the effective medium of Model B, which differs by 90° from it, can be determined. When the effective medium and excitation frequency are determined, the properties that satisfy the quarter-wave impedance matching condition can be calculated. The properties values for Model A and Model B are as follows: Model A: effective size: 53.4 mm, density $\rho_A = 3068.8 \text{ kg/m}^3$, $C_{11} = C_{66} = 42.23 \text{ GPa}$, $C_{16} = 13.72 \text{ GPa}$, Model B: effective size: 63.6 mm, density: $\rho_B = 2576.6 \text{ kg/m}^3$, $C_{11} = C_{66} = 50.37 \text{ GPa}$, $C_{16} = 16.34 \text{ GPa}$. The unit cell that satisfies the above properties was designed through shape optimization applying COMSOL Multiphysics and mma optimization, and the design model has two types of slits as shown in Fig. 4.5. The shape of the model is the same as the unit cell previously designed in the study of mode conversion metamaterials. [119] Figure 4.6 shows the designed results through shape

optimization. The detailed value of unit cells are as follows: $d = 26$ mm, $L_y = 13$ mm. Table 4.1 is the detailed values of lengths, widths, and angles of slits in 2 designed unit cells.

Figures 4.7 shows how much effective material properties are satisfied through simulation of the designed metamaterial unit cells and effective material properties, and compared them. A divergence field and a curl field are plotted for the x -direction displacement and y -direction displacement. Each field represents a longitudinal wave and a shear wave by Helmholtz decomposition. It can be seen that the metamaterial unit cells are well-designed in accordance with the effective physical properties that can produce as much phase shift as desired from the incident, reflected, and transmitted fields that match exactly.

4.5.3 Transmission and Phase Spectra for 4 Unit Cells

In order to design a mode conversion metasurface, it is necessary to design a unit cell capable of implementing all phase changes from 0 to 2π while maintaining a constant amplitude of the mode conversion wave. We construct a metasurface by using models A and B where the previously designed phase shift is different by 90° . In the mode conversion phenomenon, there is one efficient and intuitive way to control the phase shift, and by using that method, it is possible to secure 4-unit cells handling the phases from 0 to 2π with only models A and B.

As shown in Figure 4.8 (a), the wave incident on model A moves in the longitudinal wave, that is, in the $+x$ direction, and the motion of the particle moves in the $\pm x$

direction. And on the right side of the model, the transmitted wave that has undergone mode conversion proceeds in the $+x$ direction, and the particle movement moves in the $\pm y$ direction. One interesting thing about the phase of the mode conversion phenomenon is that if model is flipped upside down, the phase of transmitted wave is changed while maintaining the mode conversion phenomenon. If model A with x -axis symmetry is used as shown in figure 4.8 (b), it is possible to easily get a metamaterial unit cell that can realize the same phenomenon as the phase of model A changes by 180° . This is commonly applied to all mode conversion metamaterials as well as models A and B, and it is possible more efficiently in terms of getting a unit cell for constructing a metasurface. Since this method creates an additional phase shift, it is possible to design a unit cell that handles the phases only from 0 to π in order to construct the mode conversion metasurface. By applying this feature to models A and B, phase difference 0 and $\pi/2$ as well as π and $3\pi/2$ can be implemented, and as a result, 4 unit cells covering phase shift of 2π are formed as shown in figure 4.9.

4.5.4 Various Numerical Simulation of Metasurfaces

The metasurfaces are constructed using 4-unit cells that control phase shift. We verify the designed metasurfaces through simulation or experiment, and theoretical analysis with the generalized Snell's law for multi-mode derived earlier.

Figure 4.10 shows one supercell of a metasurface composed of 4-unit cells. Since each mode conversion is realized in a periodic condition in the y -axis direction, each

unit cell is composed of two to realize a sufficient mode conversion phenomenon with designed phase shift, and a supercell is composed of a total of eight cells as shown in figure 4.10. In this case, the phase slope($d\phi/dx$) is 60.415 (1/m), and from the generalized Snell's law for the wave mode conversion, the shear wave propagates in the case of normal incidence of the longitudinal wave and has a refraction angle of 17.46°.

Figures 4.11 (a) and 4.11 (b) are simulation verification using the designed metasurface. Figure 4.11 (a) plots the longitudinal wave field and Fig. 4.11 (b) plots the shear wave field. Through simulation verification, it can be confirmed that the longitudinal wave is incident and converted into a shear wave, and the angle is 17.46°, confirming that the designed metasurface satisfies the generalized Snell's law. In addition, since the unit cells constituting the designed metasurface are non-resonant anisotropic metamaterials, mode conversion can be performed in a desired phase in a wide frequency domain. Therefore, it can be seen that the metasurface composed of unit cells designed in a wide frequency band also performs mode conversion and angle conversion well at the same time in a wide frequency band of 90 kHz to 120 kHz, as shown in Figure 4.12.

Since the metamaterial designed to compose the mode conversion metasurface is reciprocal, it is not only converted into a shear wave when a longitudinal wave is incident, but is converted into a longitudinal wave when the shear wave is incident. Similarly, by using the transfer matrix, by adding $A_{shear}^{inc} = 1$ to the equation (Eq. (4.12)) calculated by the scattering matrix, the phase of the longitudinal wave that is

mode-transformed when the shear wave is incident can be calculated.

$$\phi = k_s^0 b + k_l^0 a + \frac{\pi}{2} = k_s^0 d - (k_s^0 - k_l^0) L_0 + \frac{\pi}{2} - \frac{(k_l^0 + k_s^0)}{2} L \propto L \quad (4.17)$$

Like the longitudinal wave incidence, it can be seen from the above equation that in the case of the shear wave incident, the phase of the mode-converted longitudinal wave is controlled depending on the length of the effective medium. Also, since model A and model B are designed depending on the size of the effective medium, the phase of the mode-converted wave differs by 90° in the case of lateral wave incident as well as longitudinal incident.

When the metasurface is constructed, the relationship between the incident angle of the shear wave and the transmission angle of the longitudinal wave can be theoretically calculated by using the generalized Snell's law for mode conversion. Since the same metasurface is used, the phase slope ($d\phi/dx$) has the same value as 60.415 (1/m). In this case, when the shear wave enters vertically, the transmission angle of the longitudinal wave is theoretically 31.22° . Figure 4.13 (a) is the longitudinal wave field of the simulation, and Fig. 4.13 (b) is the shear wave field of the simulation. It can be seen that the shear wave undergoes mode conversion and angle conversion into a longitudinal wave, and it can be verified that the angles agree with the theoretically calculated values.

We designed metasurfaces at different frequencies to show that the design method of metasurfaces is not only at 100 kHz. Figure 4.14 and Fig. 4.15 are the process of designing a metasurface for 125 kHz unlike the previously designed metasurface.

For 125 kHz, the properties of the two models with as much phase difference can be calculated. In addition, the models are designed to have the same size as the models A and B that are designed to compose the 100 kHz metasurface, and the models are designed by shape optimization as shown in Figure 4.14 (a). Accordingly, using the models designed at 125 kHz, there are transmission and phase spectra with 4-unit cells as shown in Fig. 4.14 (b). Similar to metasurface for 100 kHz, 1 supercell of the metasurface was composed of a total of 8-unit cells, and the simulation verification for it can be confirmed in Fig. 4.15. Since the size of the unit cell is designed to be the same size as the previously secured models A and B, the 100 kHz metasurface and the 125 kHz metasurface have the same phase slope. Therefore, the same refraction angle (17.46°) is calculated from the generalized Snell's law for mode conversion. It can be seen that the simulation and the theoretical content are consistent.

Figure 4.16 shows the simulation results for the case of oblique incidence to the mode conversion metasurface that is designed for normal incidence. Figure 4.16 (a) shows the case where the incident angle is 10° and Fig. 4.16 (b) shows the case where the incidence angle is 30° . When longitudinal wave is obliquely incident, the wave mode is converted into a shear wave and the refraction angle is also changed by the metasurface. On the other hand, if the refraction angle for oblique incidence is calculated theoretically using the generalized Snell's law, the angle is 11.52° for 10° incidence and 0.62° for 30° incidence. In Fig. 4.16, it can be seen that the modal-transformed wave propagates at the theoretically calculated angle, which means that

the metasurface works well for oblique incidence.

We conduct simulation verification of normal and oblique incidence of longitudinal waves in the mode-converting metasurface. As in the previous elastic metasurface studies, unwanted-mode waves propagate. Each unit cell performs well in desired transmission and desired phase shift in one dimension with periodic condition, but nevertheless, when a 2D metasurface is constructed, waves of non-target modes propagate. In other words, each unit cell transmits only the shear wave through mode conversion of the incident longitudinal waves, but the metasurface transmits not only the shear wave but also the longitudinal waves. We calculated the transmission coefficient of longitudinal and the shear waves with and without the metasurface for each incident angle, as shown in Table 4.2. As designed for shear waves, unwanted longitudinal waves propagate relatively weakly. For normal incidence, the transmission coefficient of the mode-converted shear wave is 70.89%, showing the best efficiency, and for oblique incidence, the transmission coefficient gradually decreases as the incident angle increases.

By using phase control through a phased array, it is possible to create a metalens phenomenon as well as a metasurface that changes the direction of a plane wave. The metalens is designed by appropriately arranging the models designed using the phased array equation derived theoretically.

The metalens is designed by two cases, which are as follows: 1. Mode conversion from longitudinal wave to shear wave, focal length 50 cm, 2. Mode conversion from shear wave to longitudinal wave, focal length 30 cm. In figures 4.17, it is a metalens

that converts the mode from a longitudinal wave to a shear wave. Figure 4.17 (a) shows the phase gradient graph with phase equation derived in 4.3, and Fig. 4.17 (b) and (c) show the longitudinal wave field and the shear wave field, respectively. From Fig. 4.17 (c), it can be confirmed that the incident longitudinal waves are converted into the shear waves and the waves focus on designed point. Figures 4.18 is metalens simulation that convert wave modes from shear waves to longitudinal waves. Figure 4.18 (b) plots the longitudinal wave field and Fig. 4.18 (c) plots the shear wave field, indicating that the incident shear wave is converted into longitudinal wave. Figure 4.18 (b) shows longitudinal wave focusing, and it can be seen that the wave is well controlled as designed.

4.6 Design a Mode-conserving Metasurface

In this section, like the mode conversion metasurface of 4.5, a metasurface that preserves the wave mode is designed. Here, mode preservation means controlling the direction of various modes present in the acoustic wave at the same time without changing the mode. In other words, the mode-conserving metasurface can change the refraction angle for the two mode waves through the phased array of the transmitted waves at the same time for the longitudinal and shear waves. Designing a metasurface requires designing a unit cell capable of controlling a phase shift.

4.6.1 Phase Control condition with Mode-conservation

In this section, the conditions for mode conservation are calculated. The condition for mode conservation can be calculated using the formula derived in 4.4. First, when the longitudinal wave enters and the transmittance of the longitudinal wave becomes 100%, $A_{longi}^{inc} = 1$ is substituted for Eq. (4.9), and 0 is substituted for the other A 's. Also, since the transmittance is 100%, the size of the transmitted longitudinal wave must be 1.

$$\begin{bmatrix} A_{longi}^{trans} \\ 0 \\ 0 \\ 0 \end{bmatrix} = M_{al}^{-1} T_{meta} M_{al} \begin{bmatrix} 1 \\ 0 \\ 0 \\ 0 \end{bmatrix}, \quad |A_{longi}^{trans}| = 1 \quad (4.18)$$

From the above equation, it is possible to determine the sect-mode preservation condition, which varies depending on whether mode-coupling occurs ($C_{16} \neq 0$) or not ($C_{16} = 0$) in the metamaterial. There are three conditions for the transmittance to be 100%, and the conditional expression and the transmittance at that time are summarized as follows.

$$\rho c_l = Z_l^0 \rightarrow A_{longi} = \cos k_l L + j \sin k_l L \quad (C_{16} = 0) \quad (4.19a)$$

$$\sin k_l L = 0 \rightarrow A_{longi} = 1 \quad (C_{16} = 0) \quad (4.19b)$$

$$\sin k_l L = \sin k_s L = 0 \rightarrow A_{longi} = 1 \quad (C_{16} \neq 0) \quad (4.19c)$$

In the three condition equations, the first equation is an impedance matching condition for having 100% transmittance, and the transmittance is controlled by

controlling the speed inside the metamaterial. Next, the second equation is a Fabry-Perot interference condition to have 100% transmittance, and transmitted waves of the same phase propagate from the boundary of the metamaterial. Finally, the third equation is a condition in which mode-coupling occurs and transmittance becomes 100% at the same time. It has a formula similar to Fabry-Perot interference, and transmitted waves of the same phase propagate from the boundary of the metamaterial.

Since what we want to do in this study is 100% transmission of waves in both longitudinal and shear waves, the following conditions can be established by expanding the above theoretical analysis.

$$\rho c_l = Z_l^0, \rho c_s = Z_s^0 \quad (4.20a)$$

$$\sin k_l L = \sin k_s L = 0 \quad (C_{16} = 0) \quad (4.20b)$$

$$\sin k_l L = \sin k_s L = 0 \quad (C_{16} \neq 0) \quad (4.20c)$$

In this study, the second condition of these three equations is used. The reason is that the method that satisfies the impedance matching condition is a method that has been dealt with in many metasurface studies, and there is no metasurface designed by Fabry-Perot interference yet.

In order to determine the material properties that satisfy the condition, it is approached through the Christoffel equation described in the theoretical background. Conditions to cause Fabry-Perot interference in both modes at the same time are as follows.

$$\begin{aligned}
L &= n_l \frac{\lambda_l}{2} \\
L &= n_s \frac{\lambda_s}{2}
\end{aligned} \tag{4.21}$$

Where λ_l , λ_s is wavelength of longitudinal waves and shear waves in metamaterial, respectively. And, n_l , n_s are integers. Then, from the Christoffel equation, we can calculate the relationship between the properties of the metamaterial.

$$\frac{(C_{11} + C_{66}) \pm \sqrt{(C_{11} - C_{66})^2 + 4C_{16}^2}}{2} = \rho \frac{\omega^2}{k^2} = \rho f^2 \lambda^2 = \rho f^2 \left(\frac{2L}{n} \right)^2 \tag{4.22}$$

This equation can be simplified as follows.

$$\begin{aligned}
(C_{11} + C_{66}) &= 4\rho L^2 f^2 \left(\frac{1}{n_l^2} + \frac{1}{n_s^2} \right) \\
\sqrt{C_{11}C_{66} - C_{16}^2} &= 4\rho L^2 f^2 \frac{1}{n_l n_s}
\end{aligned} \tag{4.23}$$

The above conditional expression depends on the presence or absence of mode-coupling. First, if there is no mode coupling ($C_{16} = 0$), it is simply summarized as follows.

$$\rho = \left(\frac{n_l}{2fL} \right)^2 C_{11} = \left(\frac{n_s}{2fL} \right)^2 C_{66} \tag{4.24}$$

Since there are three variables (ρ , C_{11} , C_{66}) and two equations, the number of solutions that simultaneously satisfy Fabry-Perot interference for both modes can exist indefinitely.

On the other hand, in the case of mode-coupling, since one more variable is added, the conditional expression cannot be arranged. The roots can be expressed by adding a specific conditional expression. For example, if bi-modal impedance matching is considered as in the mode conversion phenomenon discussed in 4.5, the solutions can be rearranged.

$$\begin{aligned}
C_{11} = C_{66} &= \frac{Z_0}{2\rho} \left(\frac{n_s}{n_l} + \frac{n_l}{n_s} \right) \\
C_{16} &= \frac{Z_0}{2\rho} \left(\frac{n_s}{n_l} - \frac{n_l}{n_s} \right) \\
\rho &= \frac{\sqrt{Z_0 n_l n_s}}{2fd}
\end{aligned} \tag{4.25}$$

In addition to this, in the case of mode-coupling, there are numerous solutions. In this study, to solve a simpler problem, we approach the case without mode-coupling. Meanwhile, in order to control the phase under the condition that the transmittance is 1 for both modes, the background material is considered together. The transfer matrix and scattering matrix at that time are as follows.

$$\begin{bmatrix} u \\ v \\ \sigma_{xx} \\ \sigma_{xy} \end{bmatrix}_{x=d} = T_1 T_{meta} T_2 \begin{bmatrix} u \\ v \\ \sigma_{xx} \\ \sigma_{xy} \end{bmatrix}_{x=0} \tag{4.26}$$

$$\begin{bmatrix} A_{longi}^{trans} \\ 0 \\ A_{shear}^{trans} \\ 0 \end{bmatrix} = N_{al}^{right} S_{meta} N_{al}^{left} \begin{bmatrix} A_{longi}^{inc} \\ A_{longi}^{ret} \\ A_{shear}^{inc} \\ A_{shear}^{ref} \end{bmatrix} \quad (4.27)$$

As in the mode conversion metasurface, the scattering matrix A for the metamaterial that preserves the mode is as follows.

$$S_{meta} = M_0^{-1} T M_0 = \begin{bmatrix} (-1)^{n_l} & 0 & 0 & 0 \\ 0 & (-1)^{n_l} & 0 & 0 \\ 0 & 0 & (-1)^{n_s} & 0 \\ 0 & 0 & 0 & (-1)^{n_s} \end{bmatrix} \quad (4.28)$$

Using the calculated scattering matrix, the phase of the transmitted wave at which the transmittance becomes 100% as in the mode conversion metasurface is calculated. The longitudinal wave transmitted when the longitudinal wave is incident is first considered as follows.

$$A_{longi}^{trans} = (-1)^{n_l} e^{j(k_l^0 b + k_l^0 a)} = \pm e^{j(k_l^0 b + k_l^0 a)} \quad (4.29)$$

The phase of transmitted wave is as follows.

$$\phi_l = k_l^0 (a + b) = k_l^0 (d - L) = m_l L + n_l \propto L \quad (4.30)$$

This can be similarly developed when the shear wave is incident, and the phase of the transmitted shear wave is as follows.

$$\phi_s = k_s^0 (a + b) = k_s^0 (d - L) = m_s L + n_s \propto L \quad (4.31)$$

In this way, the phase of the transmitted wave preserved in the mode is irrelevant to the physical properties of the metamaterial regardless of the incidence of the

longitudinal wave and the shear wave. In addition, it can be seen that it is linearly proportional only to the size of the metamaterial.

4.6.2 Design of Phase-controlling Unit Cells with mode-conservation

From the phases of the waves derived in 4.6.1, in order for the longitudinal wave and the shear wave to simultaneously undergo Fabry-Perot interference and phase shift, the effective size must be changed regardless of the properties of the metamaterial. Similar to the mode conversion metasurface, the shape optimization design is proceeded using a monolayer metamaterial structure as well. However, the model of the unit structure used for shape optimization design is different. As shown in Figure 4.19, in the mode-conserving metasurface, more slits are used than the mode conversion metasurface in order to control phase shifts for both modes at the same time. The detailed values of unit cells are as follows: $L_x = 39$ mm, $L_y = 13$ mm. Also, the shape of the unit structure is vertically symmetric so that mode-coupling does not occur. Therefore, the angle of the slit is fixed at 0° or 90° , and the length and thickness of the slit are variables, and the design proceeds with a total of eight variables. This unit cell structure has a higher degree of freedom. At the same time, for theoretical interpretation, we use a monolayer metamaterial whose effective size can change.

4.6.3 Transmission and Phase Spectra for 16 Unit Cells

First, we determine the size of the composed supercell that can handle both

longitudinal and shear waves at the same time. For single target mode, simply control the phase by 2π as shown in Figure 4.20 (a) for the target mode. However, considering multi-mode at the same time, if the phase is controlled by 2π for only one mode, the other mode is not sufficiently controlled to form a metasurface. Therefore, as shown in Fig. 4.20 (b), one supercell must be able to control the phase as much as an integer multiple of 2π for longitudinal and shear waves, respectively. According to Eq. (4.30) and Eq. (4.31), the phase differences $\Delta\phi_l$ and $\Delta\phi_s$ of each mode are calculated for two adjacent unit structures. Next, assuming that a supercell is composed of a total of n unit cells, the phase shift must occur for each mode by an integer multiple of 2π , so it can be summarized as follows.

$$n\Delta\phi_l = -nk_l^0\Delta L = 2\pi M \quad (4.32)$$

$$n\Delta\phi_s = -nk_s^0\Delta L = 2\pi N$$

Where M and N are integers, meaning a multiple of 2π . Using the above equation, the ratio of M and N can be calculated. When the background material is aluminum and target frequency is 100 kHz, the ratio is written as

$$N = \frac{k_s^0}{k_l^0} M = \sqrt{\frac{2}{1-\nu^0}} M \approx 1.73M, \quad (4.33)$$

where ν^0 is the Poisson's ratio of the background material. Since M and N must be integers, it can be approximated by $N \approx 7$ when it is $M = 4$ from Eq. (4.33). Therefore, when the longitudinal wave has a total phase shift of 8π , the shear wave constitutes a supercell so that the total phase shift is 14π .

Next, we determine the number of unit cells. Since the magnitude of the phase shift for each mode in one supercell is determined, the phase difference occurring in each adjacent unit cell varies depending on the number of unit cells. Since the phase of the wave has a range of $0 \sim 2\pi$, $\Delta\phi$, whose phase difference of the transmitted wave in the adjacent unit cell is greater than π is meaningless because it has the same phase as $\Delta\phi - 2\pi$. In addition, $\Delta\phi$, whose phase difference is less than 0, is similarly meaningless because it may vary depending on the arrangement order of the unit structures. Accordingly, the significant phase difference $\Delta\phi$ has the following range.

$$0 \leq \Delta\phi < \pi \quad (4.34)$$

In this study, a total of 16-unit cells are used, and adjacent unit cells have a phase difference of $\frac{1}{2}\pi$ in longitudinal wave and $\frac{7}{8}\pi$ in shear wave. Based on the first unit cell, the phases that the remaining 15-unit cells should have can be arranged as shown in Table 4.3.

Figure 4.21 is the result of designing the unit structure with the phase shift of Table 4.3 using the design method introduced in 4.6.2. Table 4.4 is the detailed values of lengths, widths, and angles of 4 slits in the 16 designed unit cells. As a result, a total of 16-unit cells are designed to have high transmittance and phase gradient for longitudinal waves as shown in figure 4.21 (a). As shown in Fig. 4.21 (b), we succeeded in designing a unit cell having a desired phase for shear waves at the same time.

4.6.4 Various Numerical Simulation of Metasurfaces

We construct the metasurface using the 16-unit cells that control the phase of transmitted waves in 4.6.3. We verify through numerical simulation that the metasurface using the designed unit cells can work well, and also theoretically verify through the generalized Snell's law for multi-mode waves.

First, as previously designed, the metasurfaces are constructed by arranging them in the order of Table 4.3. Like the mode conversion metasurface, each designed unit cell can perform phase control in the periodic condition in the y -axis direction. Therefore, in order to realize a sufficient mode conservation phenomenon, each unit cell is arranged three at a time, and a supercell is composed of a total of 48-unit cells. In this case, the phase slope ($d\phi/dx$) for the longitudinal wave is 40.277 (1/m). According to the generalized Snell's law, when a longitudinal wave enters the metasurface vertically (incident angle: 0°), the transmitted longitudinal wave has a refraction angle of 20.228° . Also, the phase slope ($d\phi/dx$) for the shear wave is 70.484 (1/m). According to the generalized Snell's law, when a shear wave enters the metasurface vertically (incident angle: 0°), the transmitted shear wave has a refraction angle of 20.501° . The angle of refraction is almost the same for each mode. This is because, when determining M and N for the supercell, $N \approx 7$ was approximated. In fact, the relationship between M and N is $N = \frac{k_s^0}{k_l^0} M$, so using the above equation, the angle of refraction has exactly the same value.

$$\begin{aligned}
\theta_{rl} &= \sin^{-1} \left(\frac{1}{k_l^0} \frac{\partial \phi_s}{\partial x} \right) = \sin^{-1} \left(\frac{1}{k_l^0} \frac{2\pi M}{L_{\text{supercell}}} \right) \\
&= \sin^{-1} \left(\frac{1}{k_s^0} \frac{2\pi N}{L_{\text{supercell}}} \right) = \sin^{-1} \left(\frac{1}{k_s^0} \frac{\partial \phi_s}{\partial x} \right) = \theta_{rs}
\end{aligned} \tag{4.35}$$

Figure 4.22 is the numerical simulation results of the designed metasurface. In Fig. 4.22 (a), only longitudinal waves are incident on the metasurface, and in Fig. 4.22 (b), only shear waves are incident on the metasurface. And figure 4.22 (c) shows the case where the longitudinal wave and the shear wave are incident on the metasurface at the same time. The arrows drawn in each figure mean the transmitted wave propagating in the direction of the theoretically calculated refraction angle. When only the longitudinal wave is incident in Fig. 4.22 (a), it can be seen that the transmitted wave is well propagating in the direction of the arrow. In addition, it can be seen that it shows fine displacement at the shear wave field, but does not form a wave. Next, as shown in Fig. 4.22 (b), it can be confirmed that the transmitted wave propagates well along the arrow in the shear wave field, similarly to the case where the shear wave is incident. And it can be seen that there is no wave at the longitudinal wave field. Finally, in Fig. 4.22 (c), the incident longitudinal wave and shear wave are each well bent to the desired angle.

Quantitative performance using transmission coefficient is also verified in mode-conserving metasurfaces. For the metasurface, since longitudinal wave incidence, shear wave incidence, and simultaneous longitudinal and shear waves are simulated, the transmission coefficients are compared for each case. The transmission

coefficients of the longitudinal and shear waves for each case are summarized in Table 4.5. When only the longitudinal wave is incident, the transmission coefficient of the longitudinal wave is 69.47% and that of the shear wave is 7.98%, so the unwanted wave hardly propagates. Similarly, even when only shear wave is incident, the transmission coefficients of the longitudinal and shear waves are 3.38% and 45.36%, respectively. Lastly, when longitudinal and shear waves are incident at the same time, the transmission coefficients are 66.98% and 67.55%, respectively.

Next, a completely different metasurface can be designed by changing the phased array of 16-unit cells. If the unit cells designed as shown in Table 4.6 are properly rearranged, a mode-separating metasurface that changes propagation direction for each mode can be designed. In Fig. 4.23, the designed unit cells are rearranged. By rearranging, we change the phase slope of the shear wave while keeping the phase slope of the longitudinal wave. The longitudinal phase slope ($d\phi/dx$) in this metasurface is 40.277 (1/m), the same as the previously designed metasurface. The phase slope of the shear wave has a value less than 0 because it is arranged in reverse order, and its value is -50.346 (1/m). When the two modes of wave are vertically incident, the angle of refraction of the longitudinal wave is 20.228° , and the angle of refraction of the shear wave is -14.487° .

Figure 4.24 is simulation verification for the mode-separating metasurface. In Fig. 4.24 (a), only longitudinal waves are incident on the metasurface, and in Fig. 4.24 (b), only shear waves are incident on the metasurface. And figure 4.24 (c) shows the case where the longitudinal wave and the shear wave are incident on the metasurface

simultaneously. The arrows drawn in each figure mean the transmitted wave propagating in the direction of the theoretically calculated refraction angle. As shown in Fig. 4.24 (a), when only the longitudinal wave is incident, the transmitted longitudinal wave propagates well in the longitudinal wave field. And Waves are not propagating in the shear wave field. Next, as shown in Fig. 4.24 (b), the transmitted shear wave propagates well along the arrow in the shear wave field. Also, waves do not propagate at the longitudinal wave field. Finally, in Fig. 4.24 (c), it can be seen that the incident longitudinal wave and shear wave each bend to a desired angle. Overall, we verified that the mode-separating metasurface works well through simulation.

4.7 Experimental Validation

In this study, we verify through experiments whether the designed metasurface is actually perform well. We verify the metasurface with a refraction angle of 17.46° , which is the first case among the designed metasurfaces. As shown in Figure 4.25 (a) and (b), when there is a metasurface and when there is no metasurface, the radiation pattern of the wave of each mode is measured. The transducer we used is a Piezo electric transducer, which has 20 cycles of sine wave as a line source. Measurement is performed by separating longitudinal and shear waves using a magnetostrictive patch transducer (MPT) and an electromagnetic acoustic transducer (EMAT). We start from 5° in the radiation pattern and measure at 10° intervals, and additionally measure the special angle that is calculated theoretically. Since the longitudinal wave

propagates at 0° , the special angle is 0° when there is no metasurface. Figure 4.25 (c) is raw data measuring longitudinal wave in the 0° direction in case there is no metasurface. Figure 4.25 (d) is raw data measuring shear waves in the 17.46° direction in the case of metasurface. In both figures, it can be seen that the desired mode wave is measured at the arrival time, considering the distance and wave velocity.

Through the experiment, the radiation pattern is shown in Fig. 4.26 (a) and (b). Since there is a difference in sensitivity for each transducer, the radiation pattern is plotted for each mode using the same transducer. Figure 4.26 (a) is a graph of the energy of the measured longitudinal wave for two cases with and without a metasurface, and Fig. 4.26 (b) is a graph of the energy of the measured shear wave. The red and black lines in Fig. 4.26 (a) are simulation results for the absence and presence of a metasurface, respectively. The circle mark and the cross mark are experimental results for each situation. In the figure 4.26 (b) representing the shear wave, the blue and magenta line are the simulation results for the absence and presence of a metasurface, respectively. Likewise, the circle mark and the cross mark are experimental results for each situation. From the experimental results measured with the radiation pattern, it can be confirmed that the metasurface follows the simulation quite well at the target frequency, and that mode conversion and direction control are good.

4.8 Summary

In this chapter, we theoretically approach the phase controlling method while transmitting the desired mode with high transmittance by using the transfer matrix method for the elastic wave. We design the unit cells that can cause the desired phase shift of the wave of the desired mode and match it with the theoretical analysis. In addition, we successfully design metasurfaces that perform mode conversion and mode conservation by phased array the designed phase control unit cells. This metasurface design technology for wave steering is used as the most intuitive way to control the direction of the wave, and it is significant that it is implemented for difficult elasticity because there are many wave modes. Our future research interest will focus on applying this work to the fabrication of practicable forms that can be used for actual inspection situation. Wave steering technology using metasurfaces is expected to be a powerful way to manipulate ultrasonic waves in more intuitive ways.

Table 4.1 Values of lengths, widths, and angles of slits in designed models.

Model A	l_1	10.465 mm
	h_1	5.018 mm
	θ_1	19.641°
	l_2	11.336 mm
	h_2	7.020 mm
	θ_2	23.929°
Model B	l_1	14.885 mm
	h_1	9.178 mm
	θ_1	27.566°
	l_2	7.787 mm
	h_2	2.600 mm
	θ_2	21.545°

Table 4.2 Transmission coefficient of L to S mode-converting metasurface for each incident angle.

Incident angle (°)	t_L (%)	t_S (%)
0 (normal incidence)	14.84	70.89
10	10.42	69.38
30	18.36	56.97

Table 4.3 Phase shift values of unit cells when longitudinal and shear waves are incidence.

Unit cell #	Phase shift of longitudinal wave (rad)	Phase shift of shear wave (rad)
1	0	0
2	0.5π	0.875π
3	π	1.750π
4	1.5π	0.625π
5	$2\pi (= 0)$	1.500π
6	0.5π	0.375π
7	π	1.250π
8	1.5π	0.125π
9	$2\pi (= 0)$	π
10	0.5π	1.875π
11	π	0.750π
12	1.5π	1.625π
13	$2\pi (= 0)$	0.500π
14	0.5π	1.375π
15	π	0.250π
16	1.5π	1.125π

Table 4.4 The detailed values of slits in designed unit cells.

Unit cell #	Slit 1	Slit 2	Slit 3	Slit 4
	$(l_1, r_1) / L_y$	$(l_2, r_2) / L_y$	$(l_3, r_3) / L_y$	$(l_4, r_4) / L_y$
	θ_1 (rad)	θ_2 (rad)	θ_3 (rad)	θ_4 (rad)
1	(0.487,0.045)	(0.361,0.127)	(0.236,0.014)	(0.236,0.014)
	0.5π	0.5π	0.5π	0.5π
2	(0.439,0.010)	(0.339,0.028)	(0.155,0.108)	(0.155,0.108)
	0.5π	0.5π	0.5π	0.5π
3	(0.690,0.150)	(0.157,0.105)	(0.541,0.207)	(0.541,0.207)
	0	0	0	0
4	(0.454,0.053)	(0.401,0.289)	(0.573,0.087)	(0.684,0.021)
	0.5π	0	0.5π	0.5π
5	(0.501,0.048)	(0.377,0.117)	(0.160,0.064)	(0.160,0.064)
	0.5π	0.5π	0.5π	0.5π
6	(0.395,0.076)	(0.175,0.124)	(0.153,0.100)	(0.153,0.100)
	0.5π	0.5π	0.5π	0.5π
7	(0.010,0.023)	(0.196,0.010)	(0.178,0.017)	(0.178,0.017)
	0.5π	0.5π	0.5π	0.5π
8	(0.609,0.011)	(0.325,0.285)	(0.468,0.019)	(0.695,0.013)
	0.5π	0	0.5π	0.5π
9	(0.450,0.057)	(0.390,0.120)	(0.478,0.051)	(0.478,0.051)
	0.5π	0.5π	0.5π	0.5π
10	(0.400,0.078)	(0.215,0.147)	(0.076,0.013)	(0.076,0.013)
	0.5π	0.5π	0.5π	0.5π
11	(0.471,0.047)	(0.153,0.097)	(0.161,0.098)	(0.161,0.098)
	0	0	0	0
12	(0.590,0.015)	(0.380,0.292)	(0.471,0.016)	(0.683,0.024)
	0.5π	0	0.5π	0.5π
13	(0.461,0.025)	(0.583,0.010)	(0.161,0.104)	(0.161,0.104)
	0.5π	0.5π	0.5π	0.5π
14	(0.631,0.169)	(0.219,0.109)	(0.125,0.081)	(0.125,0.081)
	0	0.5π	0.5π	0.5π
15	(0.700,0.111)	(0.198,0.088)	(0.230,0.143)	(0.230,0.143)
	0	0	0	0
16	(0.609,0.025)	(0.381,0.293)	(0.488,0.010)	(0.700,0.010)
	0.5π	0	0.5π	0.5π

Table 4.5 Transmission coefficient of mode-conserving metasurface for each mode of incident wave.

Incident waves	t_L (%)	t_S (%)
Longitudinal wave	69.47	7.98
Shear wave	3.38	45.36
Longitudinal & Shear waves	66.98	67.55

Table 4.6 Unit cells rearranged for the mode-splitting metasurface. And phase shift values when longitudinal and shear waves are incidence.

Unit cell #	Phase shift of longitudinal wave (rad)	Phase shift of shear wave (rad)
1	0	0
14	0.5π	1.375π
11	π	0.750π
8	1.5π	0.125π
5	$2\pi (= 0)$	1.500π
2	0.5π	0.875π
15	π	0.250π
12	1.5π	1.625π
9	$2\pi (= 0)$	π
6	0.5π	0.375π
3	π	1.750π
16	1.5π	1.125π
13	$2\pi (= 0)$	0.500π
10	0.5π	1.875π
7	π	1.250π
4	1.5π	0.625π

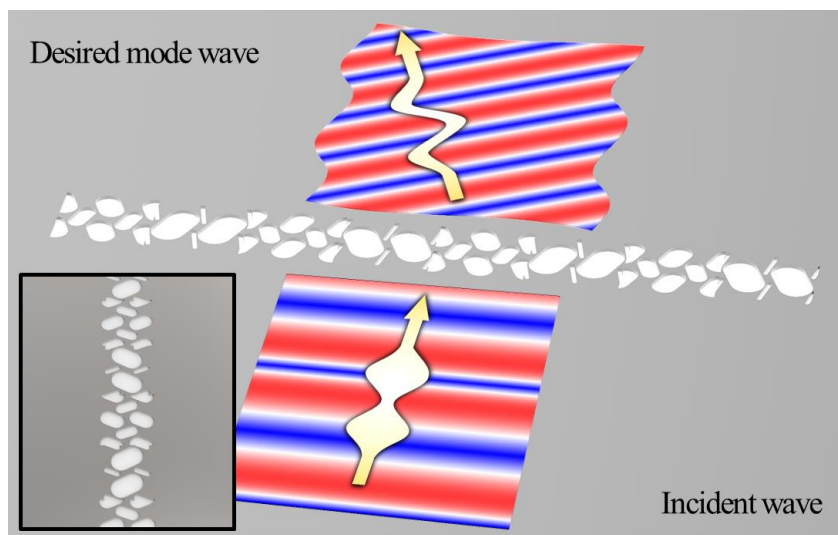


Fig. 4.1 A schematic diagram of elastic mode-control metasurface.

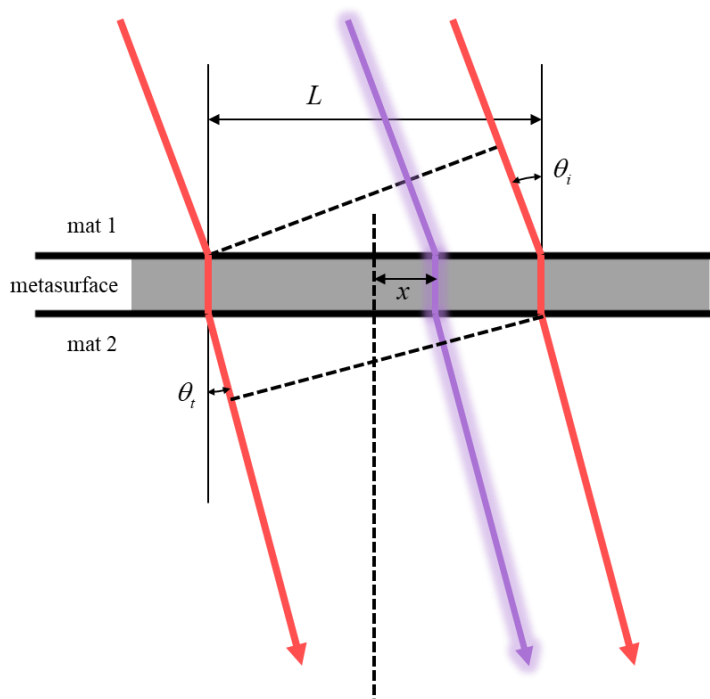


Fig. 4.2 The diagram of wave path from material 1 to material 2 to derive generalized Snell's law for multi-mode. There is a metasurface between two materials.

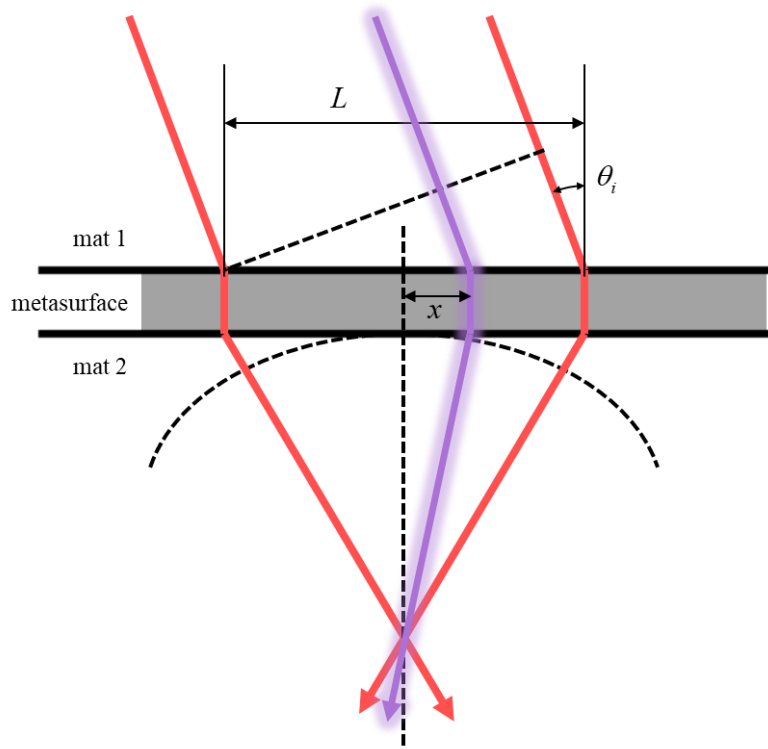


Fig. 4.3 The diagram of wave path from material 1 to material 2 to derive phase equation for wave focusing. There is a metalens between two materials.

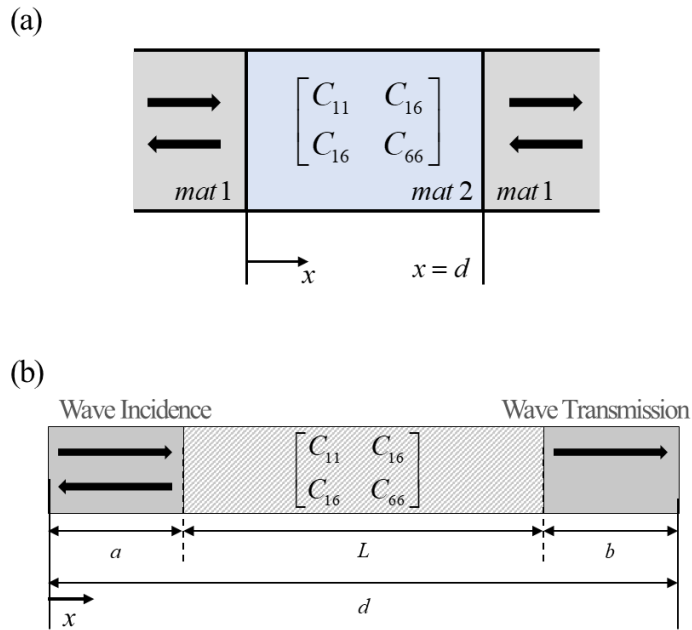


Fig. 4.4 The model for applying transfer matrix method consider (a) the only metamaterial layer and (b) background medium. The left and right medium is a background medium and the center medium is a metamaterial.

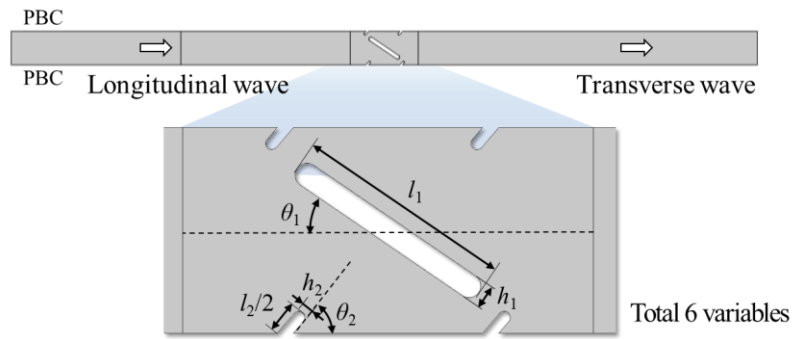


Fig. 4.5 Shape optimization model with 6 variables for mode-converting metamaterial.

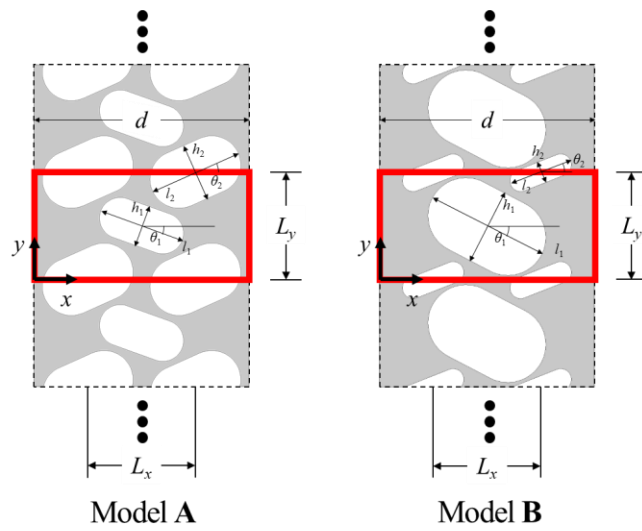


Fig. 4.6 2 mode-converting unit cells designed by shape optimization. The detailed values of lengths, widths, and angles of slits are written in Table. 4.1.

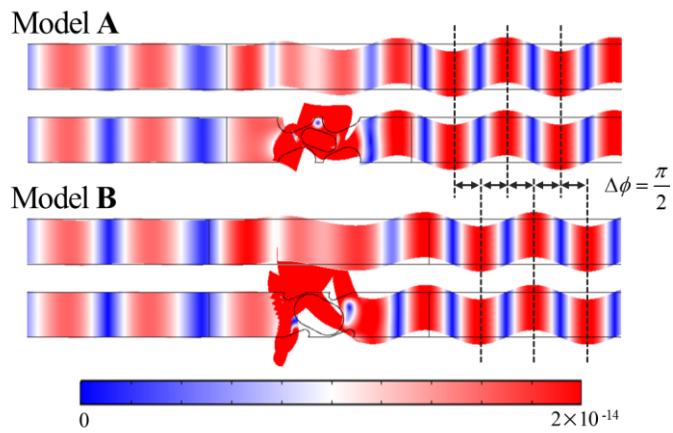


Fig. 4.7 Simulation verification of designed unit cells. The two simulation results in Model A are the simulation results for the effective medium and the designed unit cell from above. Similarly, the two simulation results in Model B are the simulation results for the effective medium and the designed unit cell from above.

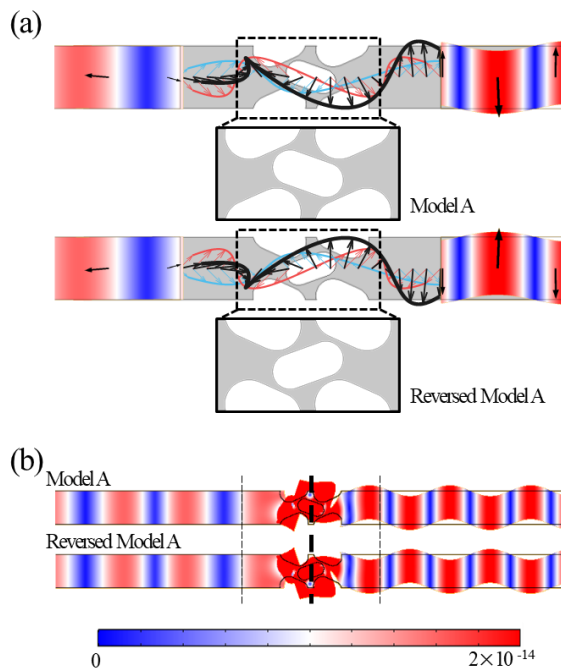


Fig. 4.8 (a) The phase shift of the transmitted shear wave is controlled by using the flipped model A. An incident longitudinal wave is shown on the left side of the unit cell, and a transmitted shear wave is shown on the right side. (b) Simulation results over a wider area is shown to check the phase shift in more detail.

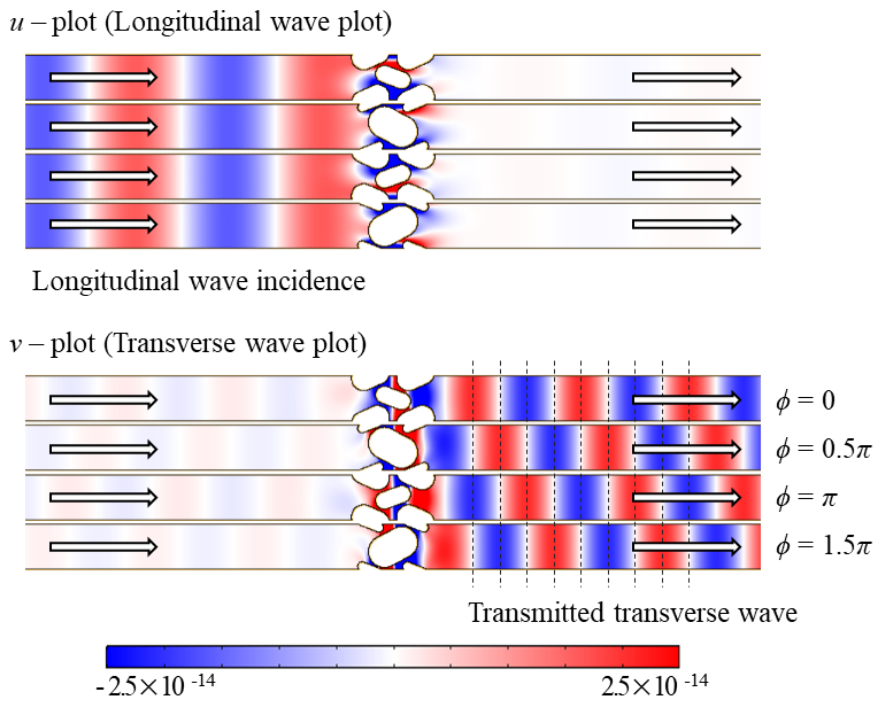


Fig. 4.9 Transmission and phase spectra of the transmitted shear waves using model A, model B, and the reversed models.

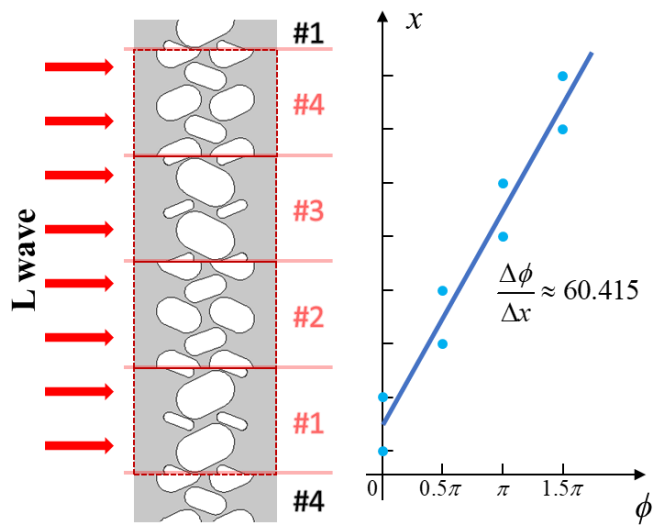


Fig. 4.10 Metasurface and phase gradient graph constructed using designed models.

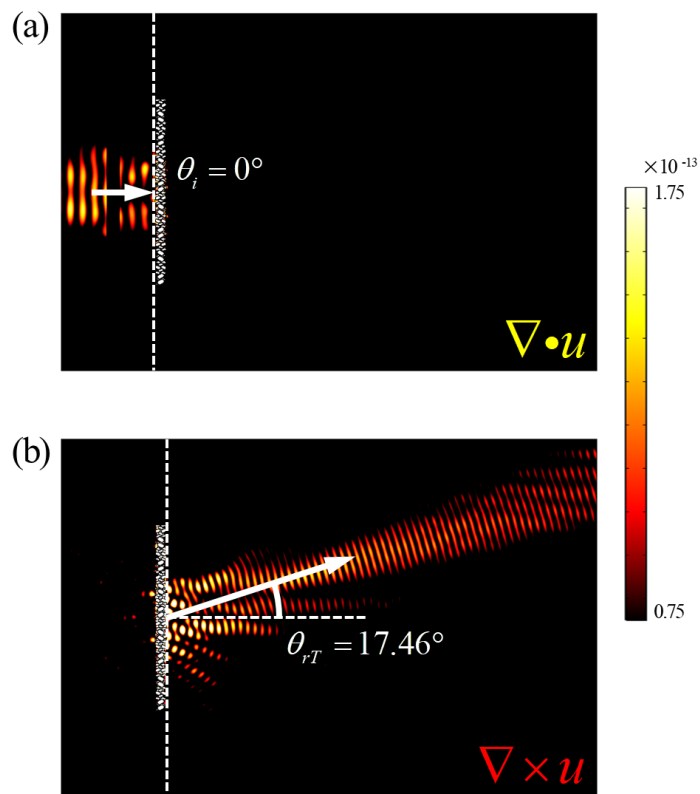


Fig. 4.11 Simulation results when a longitudinal wave enters into the mode-conversion metasurface. (a) Longitudinal wave field and (b) shear wave field are plotted respectively.

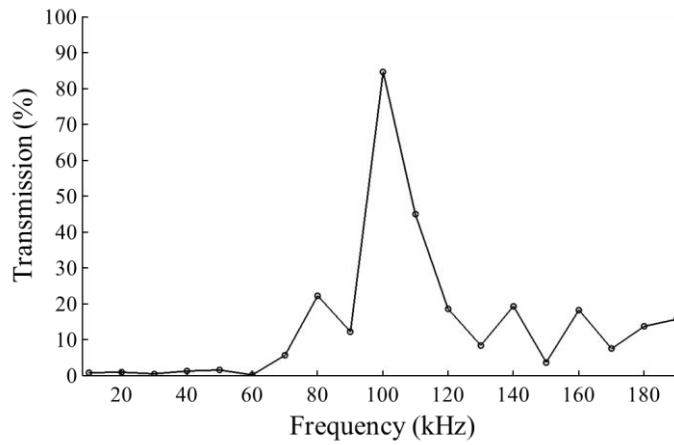


Fig. 4.12 The results of frequency sweeps when a longitudinal wave enters into the designed metasurface.

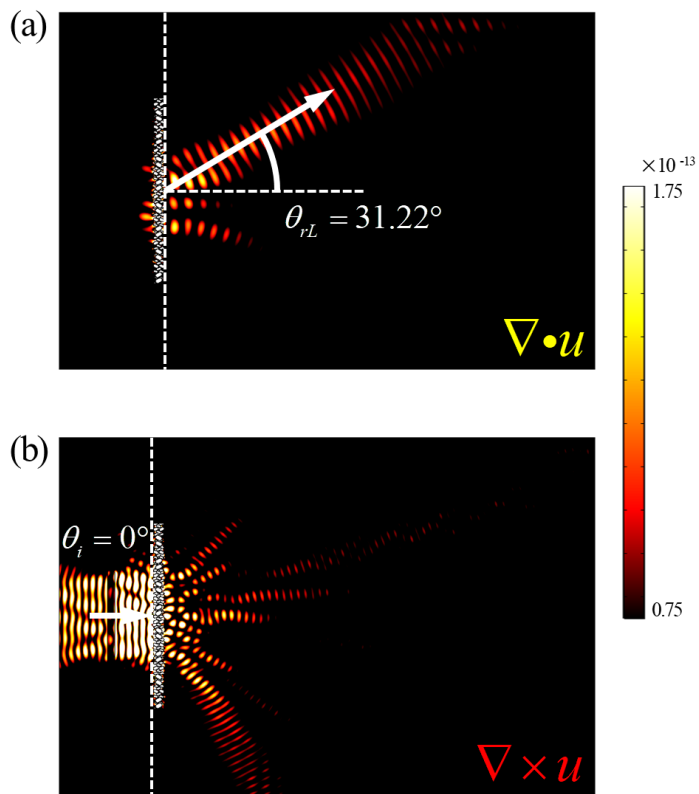


Fig. 4.13 Simulation results when a shear wave enters into the mode-conversion metasurface. (a) Longitudinal wave field and (b) shear wave field are plotted respectively.

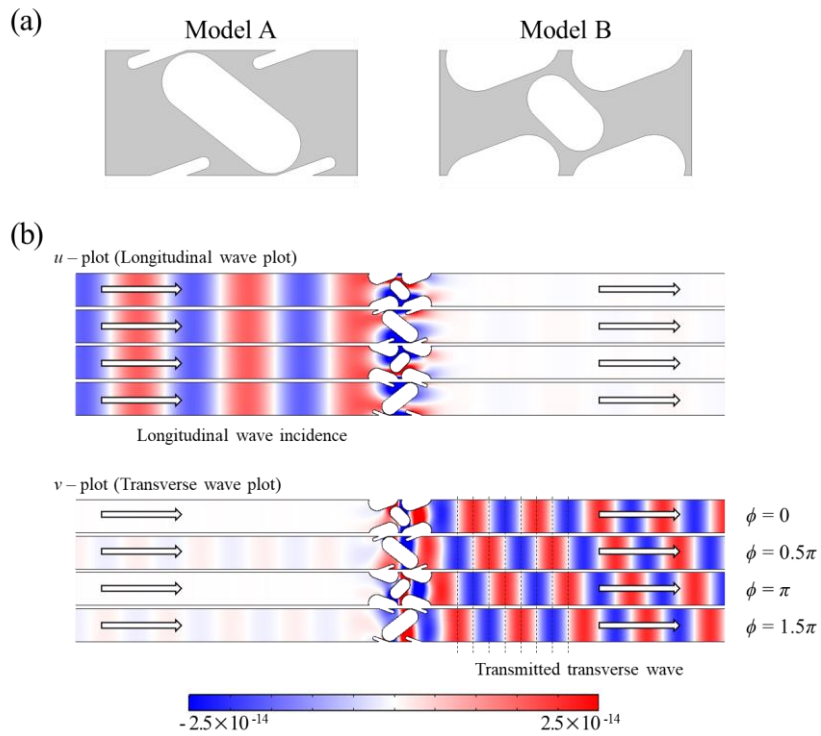


Fig. 4.14 (a) Designed unit cells with target frequency of 125 kHz. (b) Transmission and phase spectra using two designed models.

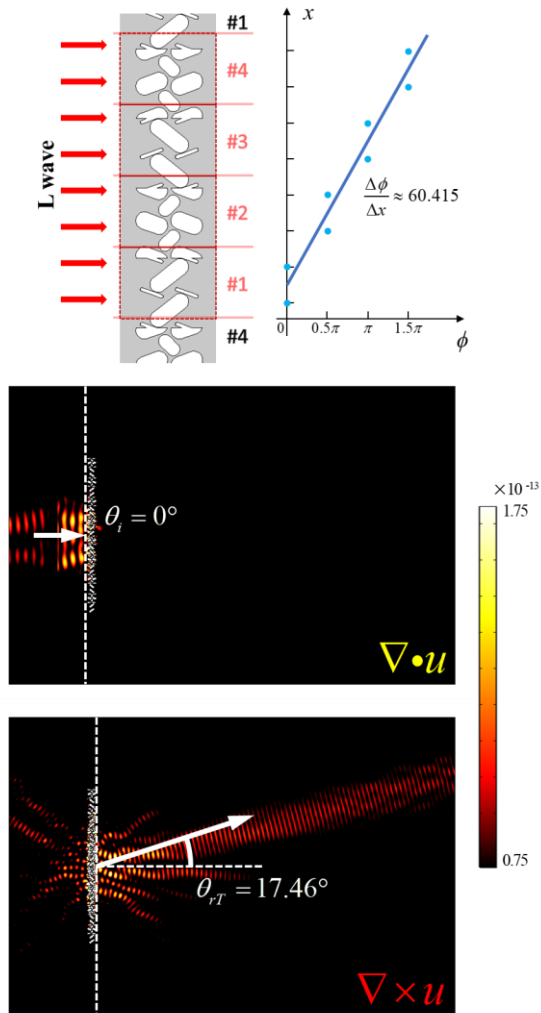


Fig. 4.15 Metasurface configuration at 125 kHz and simulation results when longitudinal waves are incident.

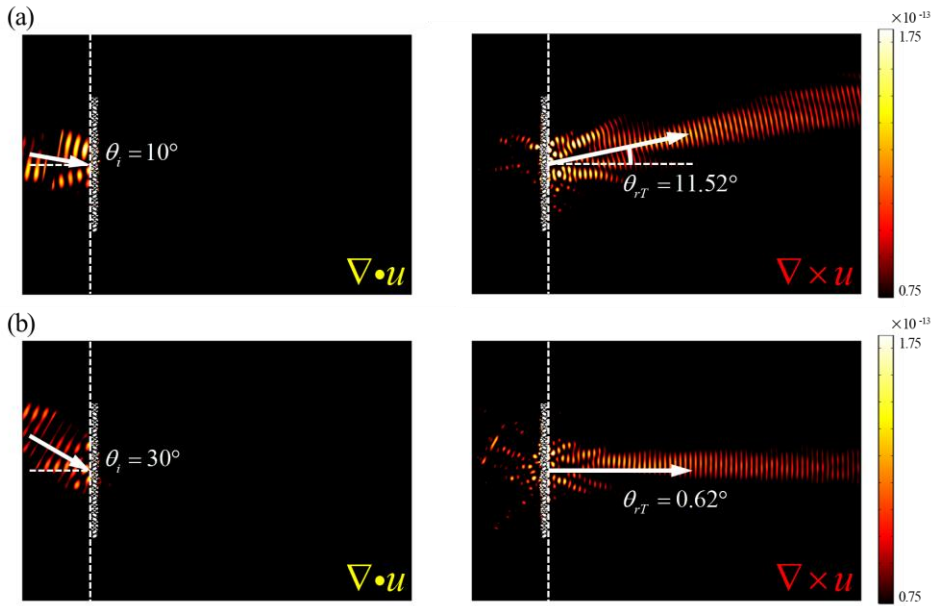


Fig. 4.16 Simulation results when the longitudinal wave oblique incidence with incidence angle (a) 10° and (b) 30° in the metasurface designed at 100 kHz.

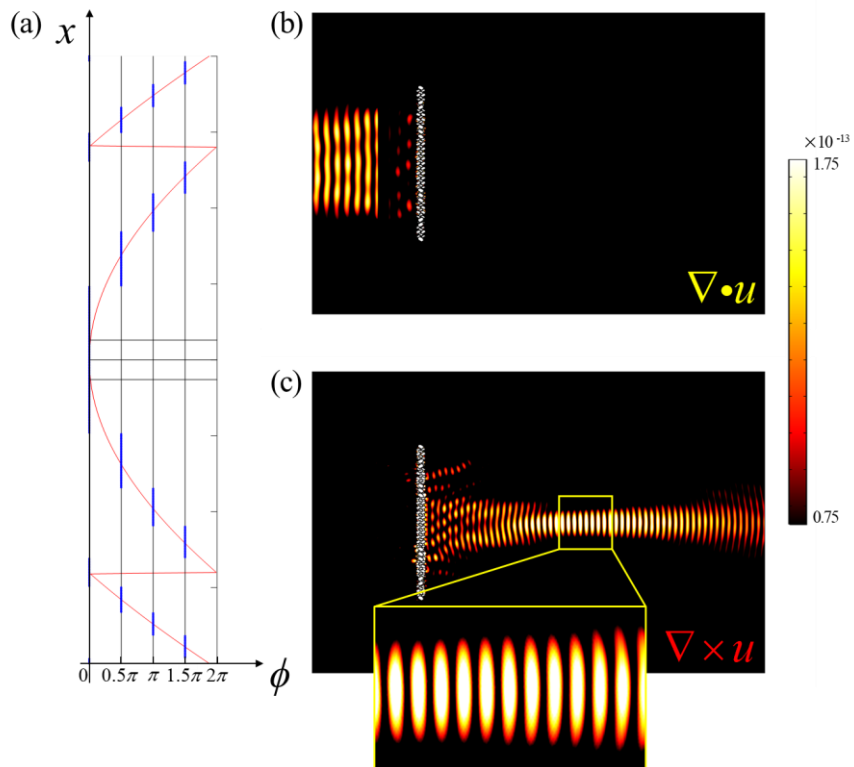


Fig. 4.17 (a) Phase gradient graph(Φ - x) for L to S metalens with focal point $p = 0.5$ m and simulation result when longitudinal wave is incident. (b) Longitudinal wave field and (c) shear wave field are plotted respectively.

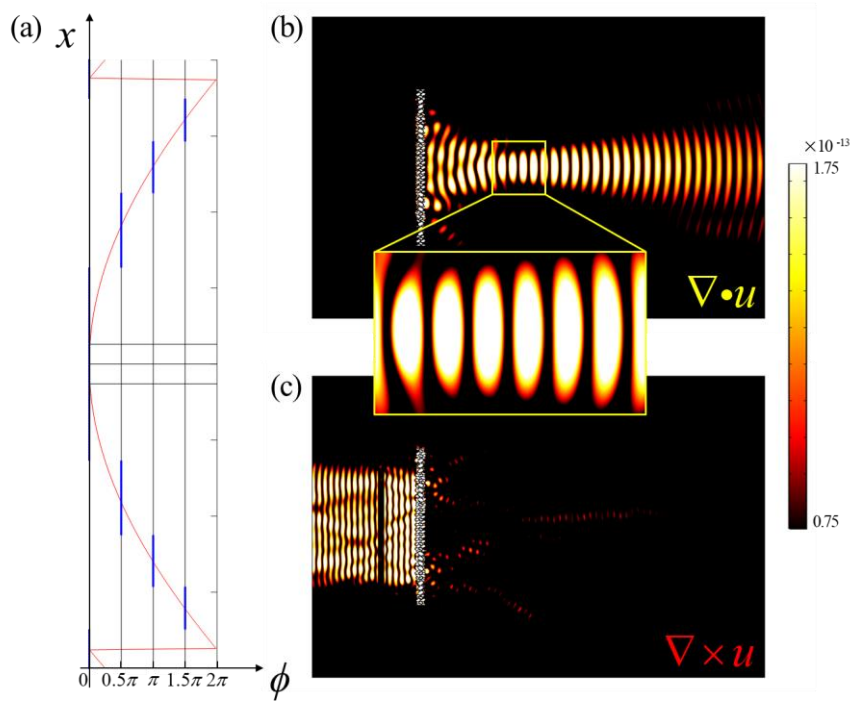


Fig. 4.18 (a) Phase gradient graph(Φ - x) for S to L metalens with focal point $p = 0.3$ m and simulation result when shear wave is incident. (b) Longitudinal wave field and (c) shear wave field are plotted respectively.

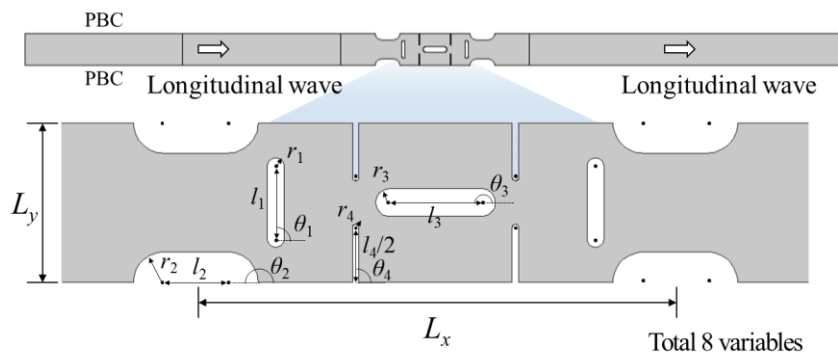


Fig. 4.19 Shape optimization model with 8 variables for mode-conserving metamaterial.

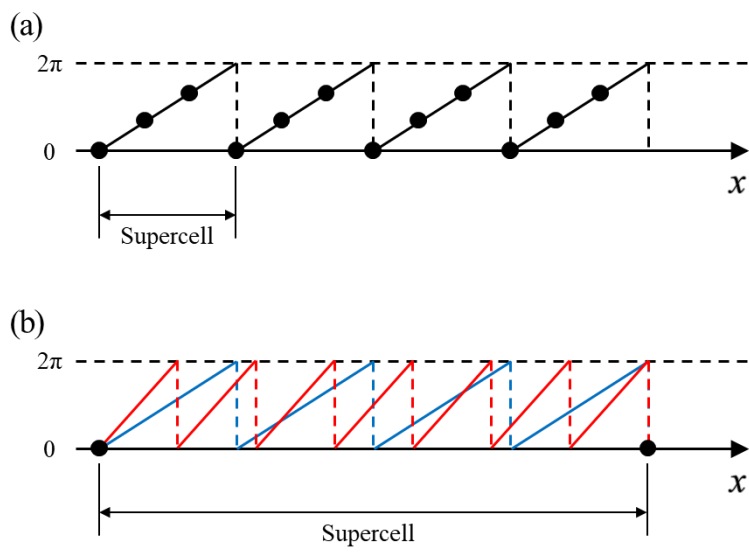


Fig. 4.20 Supercell of metasurface for (a) only one wave mode (b) multi-mode.

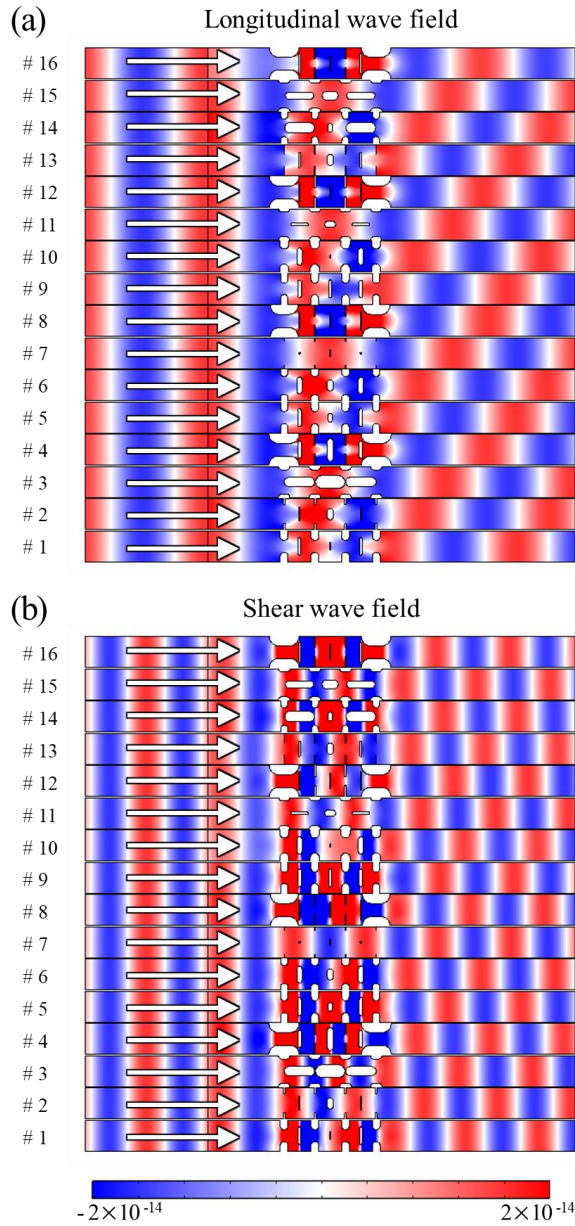


Fig. 4.21 Transmission and phase spectra for the mode-conservation metasurface when (a) longitudinal waves and (b) shear waves enter into designed 16 unit cells respectively.

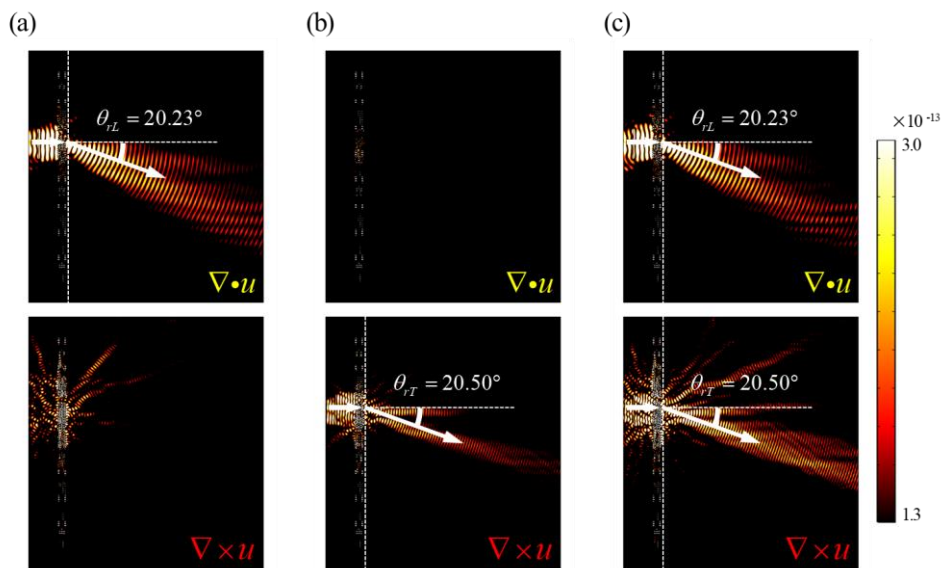


Fig. 4.22 Simulation results for the mode-conservation metasurface when (a) only longitudinal waves (b) only shear waves and (c) both waves enter.

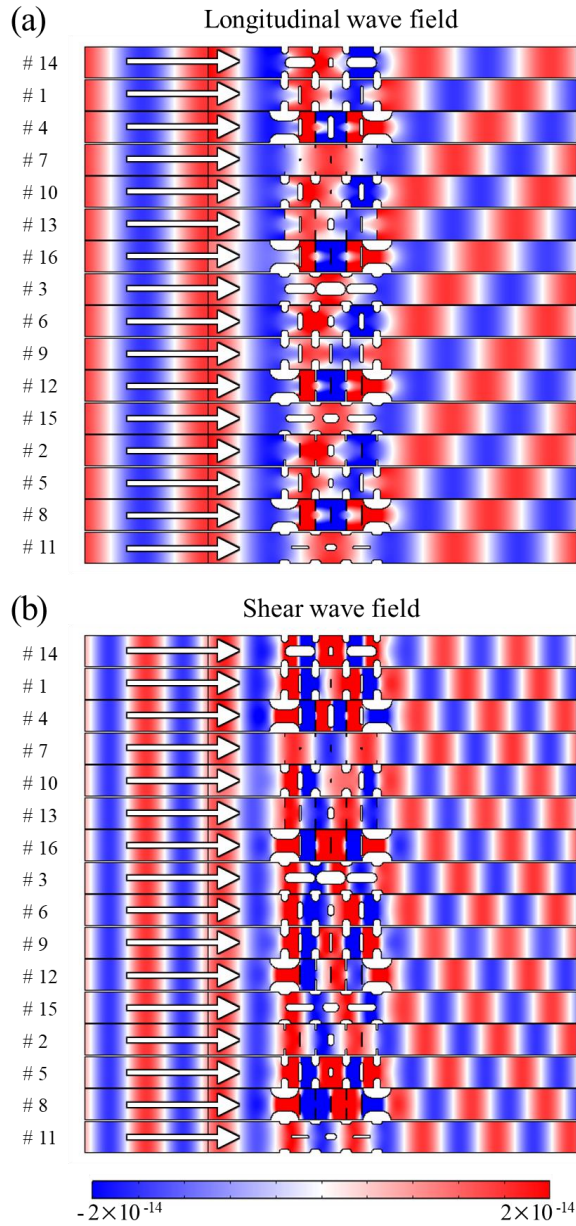


Fig. 4.23 Transmission and phase spectra for the mode-splitting metasurface when (a) longitudinal waves and (b) shear waves enter into designed 16 unit cells respectively.

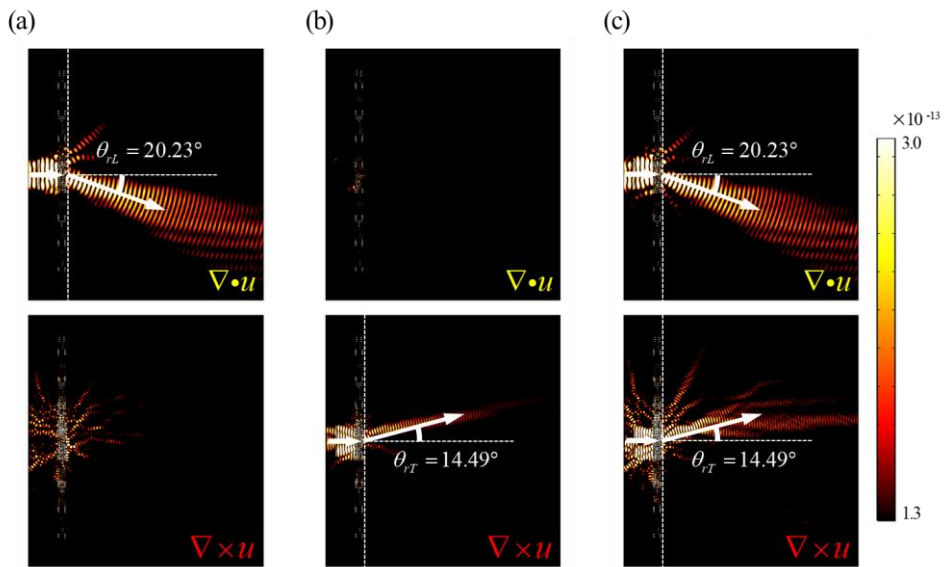


Fig. 4.24 Simulation results for the mode-splitting metasurface when (a) only longitudinal waves (b) only shear waves and (c) both waves enter.

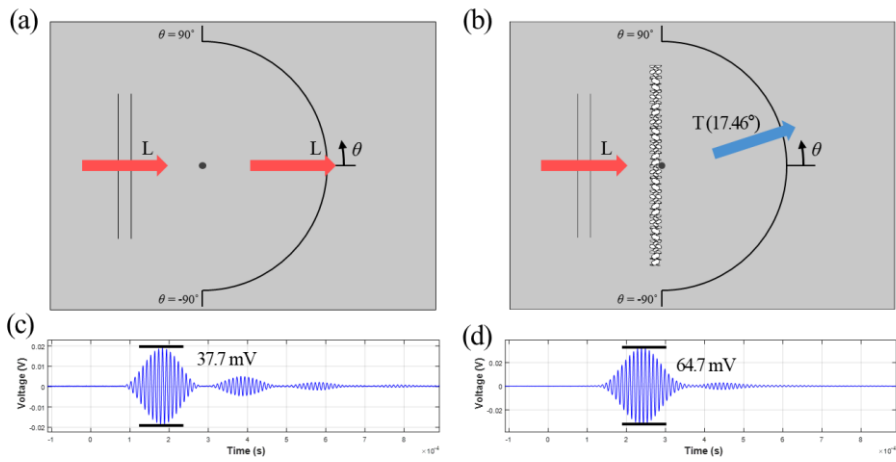


Fig. 4.25 (a) Experiment model when there is no metasurface on an aluminum plate. (b) Experiment model when there is a mode-conversion metasurface on an aluminum plate. (c) Raw data of target direction(0°) of the longitudinal wave in the model without the metasurface. (d) Raw data of target direction(17.46°) of the shear wave in the model without the metasurface.

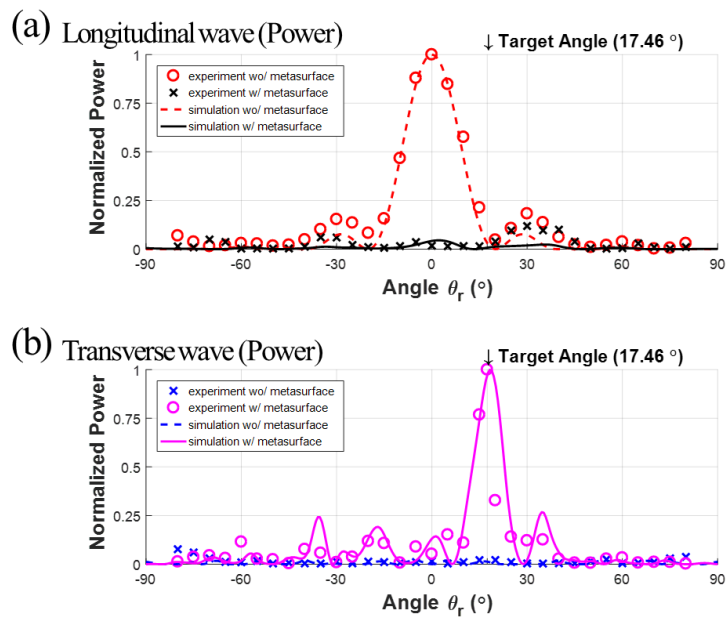


Fig. 4.26 Radiation pattern graph for experimental results. The solid line is the simulation result when there is a metasurface, and the dotted line is the simulation result when there is no metasurface. The circle and the cross mark are experimental results.

<CHAPTER 5>

CONCLUSIONS

In this dissertation, metamaterials that control the direction by considering the elastic wave mode was presented through theoretical analysis, numerical simulation, and experimental verification. In particular, the multi-mode existing in the elastic wave is difficult, which makes it difficult to study many elastic metamaterials. We controlled the elastic waves in the desired wave mode with the transmittance of 100% and the waves in the desired direction. Furthermore, various wave phenomena such as wave cancellation or wave mode separation could be implemented by controlling wave direction in consideration of multi-mode. In this dissertation, the wave can be controlled largely by the method using EFC of phononic crystals and transfer matrix of metamaterials which compose the metasurface, and the detailed investigation of this study can be summarized as follows.

First, the response-based EFC using finite element analysis for the phononic crystal structure is useful for estimating the relationship between the incident angle and the refraction angle. Because the wave number in the tangential direction is maintained while the wave is incident and transmitted, the direction of the wave at all points can be estimated using EFC. All points mean include inside the phononic crystal structure and after passing through the phononic crystal structure. In this way, the

method of EFC has a great advantage that it is simple and easy to control the wave direction.

Using EFC of the elastic phononic crystal prism, it was found that only one mode wave propagates at a specific frequency within the phononic crystal structure. And we were able to control the incident waves at different angles of incidence in the same direction. The direction in which the incident wave enters within the phononic crystal prism and the direction after passing through the prism can be determined. Furthermore, two incident waves with transmission propagating in the same direction were well tuned to cancel the waves from each other. We verified wave direction control and wave cancellation through simulation and experiment.

Next, we theoretically approach metamaterials and metasurfaces using the transfer matrix method. Transfer matrix method is a really powerful method when we want to estimate the waves motion in a medium with known material properties or when we want to calculate the material properties of an effective medium where the wave that moves desired. The transfer matrix method shows the relationship between displacement and stress only, so that the physical behavior within the model can be calculated. In addition, it calculates the dynamic material properties of the unit cell that controls the amplitude and phase of transmitted waves. Dynamic material properties are great useful because using them can grasp dynamic situations in which motions of particles in the model are constantly changing, such as waves.

We designed metamaterial structures that have the dynamic properties obtained from the transfer matrix method. We found a model that could sufficiently control the wave, and designed it using shape optimization. In other words, it can be said that the metamaterial structures designed using the transfer matrix method and shape optimization were verified through theoretical analysis and numerical simulation. We designed not only at one frequency, but also at other frequencies using the proposed metamaterial structure design. Therefore, it was shown that the proposed design can be tuned to some extent and can freely respond to a given situation.

We constructed various metasurfaces by properly phased array of the designed metamaterial structures. Since metasurfaces have been mainly dealt with for single mode, we derived generalized Snell's law for multimode waves, which is not well known, and metasurfaces were theoretically and simulated verified. We designed it by dividing it into a mode conversion metasurface and a mode conservation metasurface by considering the multimodes in the elastic wave. For each metasurface, it was verified that the theoretically derived transfer matrix and the actually designed metamaterial structure. Finally, the metasurfaces which consist of designed unit cells were verified by theoretical analysis, simulation, and experiment.

In conclusion, this dissertation deals with two methods that control the direction of the wave considering elastic wave mode. The metamaterial structures, designed by

two powerful methods, EFC and the transfer matrix method, worked well to deflect the elastic waves in the desired direction in the desired wave mode. The overall results are expected to be remarkably useful in various elastic ultrasound applications such as non-destructive testing and bio-medical monitoring system, because it is a metamaterial design technology that solves the inherent difficulties in elastic waves with multi-mode. As these models are applied to actual applications, their practicality should be maximized in fields that require the direction control of elastic ultrasonic waves.

APPENDIX A.

Variables affecting the efficiency of metasurfaces

Variables affecting the efficiency of metasurfaces have been explored in previous metasurface studies. Here, the efficiency of the metasurface is qualitatively determined by the intensity of the wave in the desired direction from the simulation result. As a known method of controlling the metasurface efficiency, the efficiency varies depending on the phase gradient of the metasurface, the thickness of the metasurface, and the number of unit cells constituting the metasurface. In order to increase the efficiency of the metasurface, it is necessary to have a small phase gradient, a small thickness, and a large number of unit cells.

However, compared with previous works, the metasurfaces designed in this dissertation are composed of anisotropic materials and the physical behavior is different. And as the unit cells have different effective sizes, the shape of the metasurface made of the effective medium is also different. Therefore, as shown in Fig. A.1 (a), we examine how the efficiency of the metasurface changes through simulation while controlling the phase gradient, thickness, and number of unit cells in the mode-converting metasurface of longitudinal wave incidence and shear wave transmission. Since it is difficult to design unit cells that satisfy each condition, we use the effective medium that performs the desired physical behavior. Detailed values for each variable are shown in Fig. A.1 (b). The phase gradient is 60.415 (1/m) for refraction angle 17.46° in this study and 100.629 (1/m) for refraction angle 30° .

The smallest thickness w_0 of unit cell among the unit cells is 1, 2, 3, 4, 5 cm. And the number of unit cells n is 4, 8, 16, 32, 64.

In order to obtain the effective properties of each effective medium, the effective length of the effective medium is calculated. The effective length of the i -th effective medium is written as

$$w_i = w_0 + \Delta w(i-1) \quad (\text{A.1})$$

where i is a natural number up to $n/2$, Δw is the length difference of adjacent unit cells, and can be calculated using the phase different from Eq. 4.15.

$$\Delta w = \frac{2}{k_l^0 + k_s^0} \Delta \phi = \frac{2}{k_l^0 + k_s^0} \frac{2\pi}{n} \quad (\text{A.2})$$

In the mode conversion metamaterial, since the unit cell is turned upside down and C_{16} is changed to $-C_{16}$, the metasurface can be configured by calculating the effective properties for half of the total number of unit cells. The effective properties of the mode conversion metamaterial can be calculated when the effective length is determined, and the values are written as [117]

$$\begin{aligned} \rho &= \frac{\sqrt{\tilde{Z}_0 n_{FS} n_{SS}}}{4fw_i} \\ C_{11} = C_{66} &= \frac{\tilde{Z}_0}{2\rho} \left(\frac{n_{SS}}{n_{FS}} + \frac{n_{FS}}{n_{SS}} \right) \\ C_{16} &= \frac{\tilde{Z}_0}{2\rho} \left(\frac{n_{SS}}{n_{FS}} - \frac{n_{FS}}{n_{SS}} \right) \end{aligned} \quad (\text{A.3})$$

where f is the frequency, \tilde{Z}_0 is the bimodal impedance. And n_{FS} and n_{SS} are integers that satisfy the condition $n_{SS}/2 - n_{FS}/2 = \text{odd}$. In this simulation, $n_{FS} = 5$ and $n_{SS} =$

7 are used as values that satisfy condition.

First, Fig. A.2 and Fig. A.3 are simulation results for two variables of w_0 , n for a small phase gradient. Figure A.2 plots the shear wave field as the number of unit cells n changes when the w_0 is 1 cm. And Fig. A.3 shows the shear wave field of the simulation results as the smallest thickness w_0 changes when the number of unit cells in one supercell n is 8. From two figures, it can be seen that the thinner the metasurface and the larger the number of unit cells, the higher the metasurface efficiency.

Next, Fig. A.4 and Fig A.5 are simulation results for two variables of w_0 , n for a large phase gradient. Like Fig. A.2, Fig. A.4 plots the shear wave field of the simulation results as the number of unit cells n changes when w_0 is 1 cm. And Fig. A.5 plots the shear wave field for the change of the smallest thickness w_0 when the number of unit cells n is 8. As with a small phase gradient, the thinner the metasurface and the larger the number of unit cells, the higher the efficiency. In addition, compared to Fig. A.2 and Fig. A.3, metasurfaces with a smaller phase gradient show high efficiency compared to metasurfaces with a larger phase gradient, so the smaller the phase gradient, the higher the metasurface's efficiency.

The comprehensive summary of metasurface efficiency for various variables is as follows. Even if the metasurface is composed of anisotropic metamaterials with mode coupling, the smaller the phase gradient, the thinner the metasurface, and the larger the number of unit cells constituting the metasurface, the better the efficiency of the metasurface.

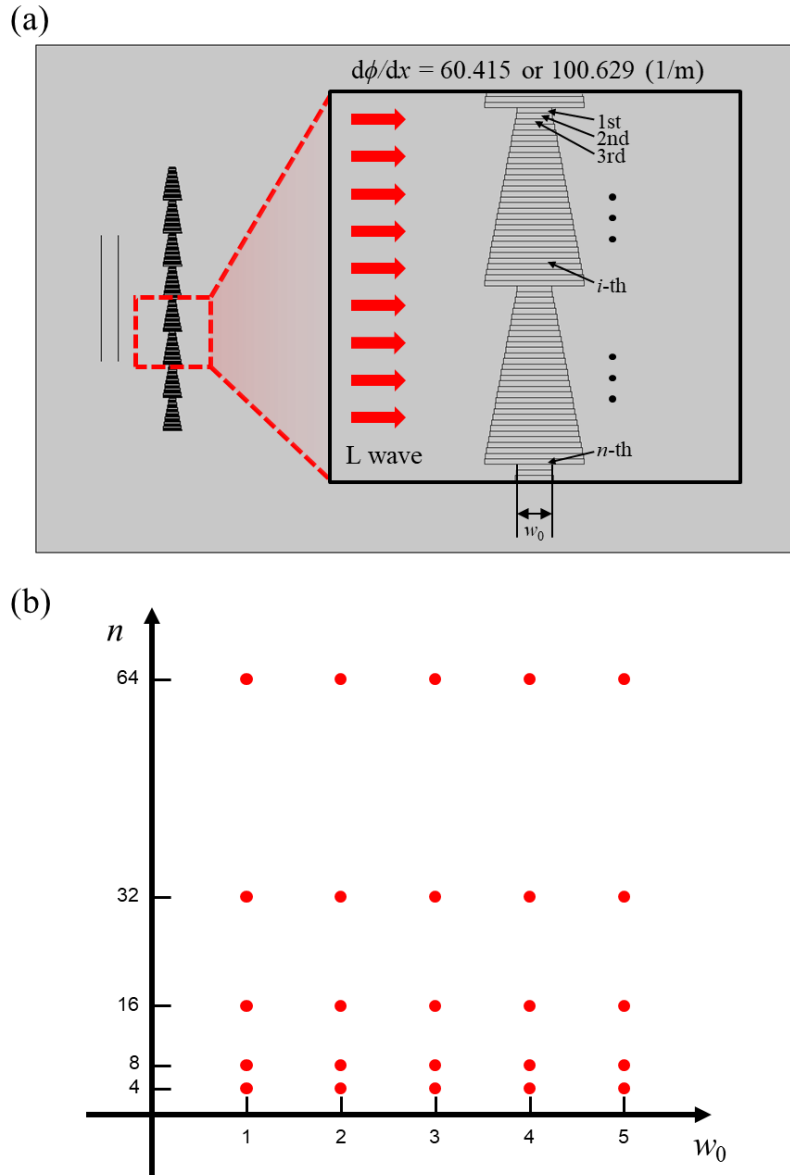


Fig. A.1 (a) Simulation model using effective medium while controlling the phase gradient, thickness, and number of unit cells in the mode-converting metasurface (b) Combination of controlled variables

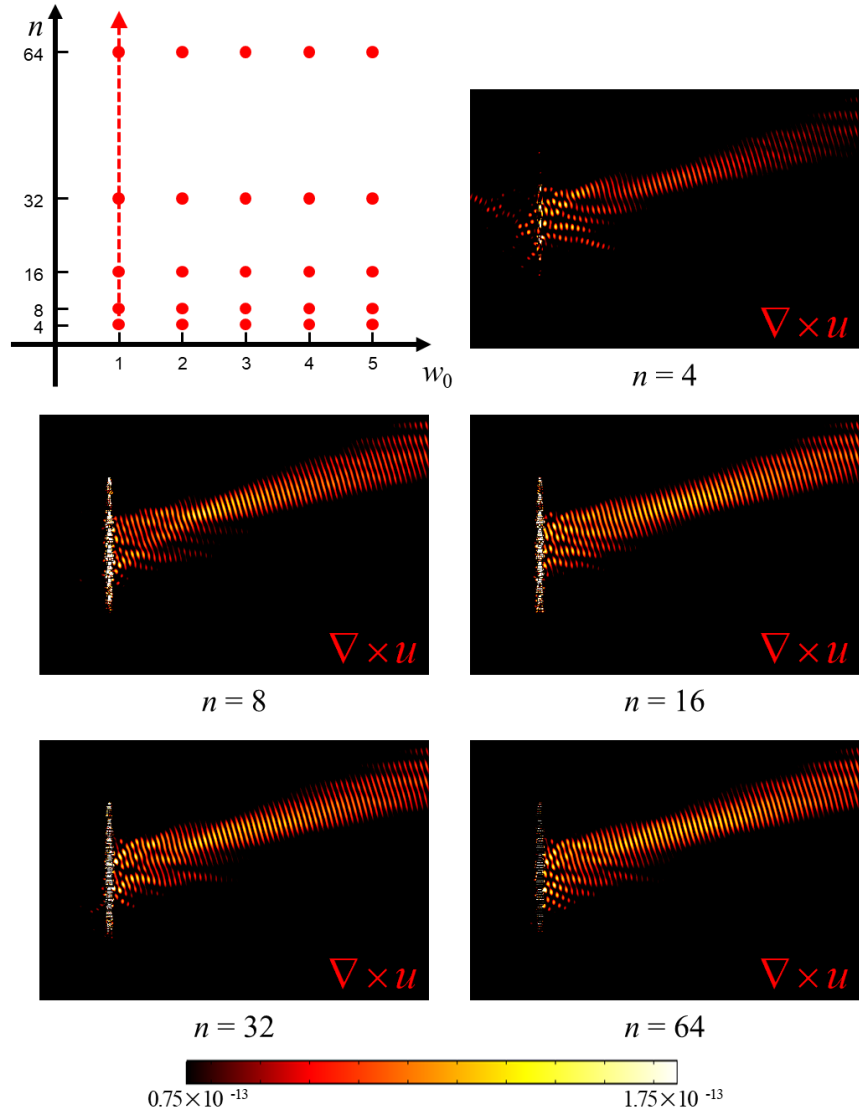


Fig. A.2 The simulation results that plot shear wave field when the phase gradient is small, the smallest thickness w_0 is fixed, and the number of unit cells n is changed.

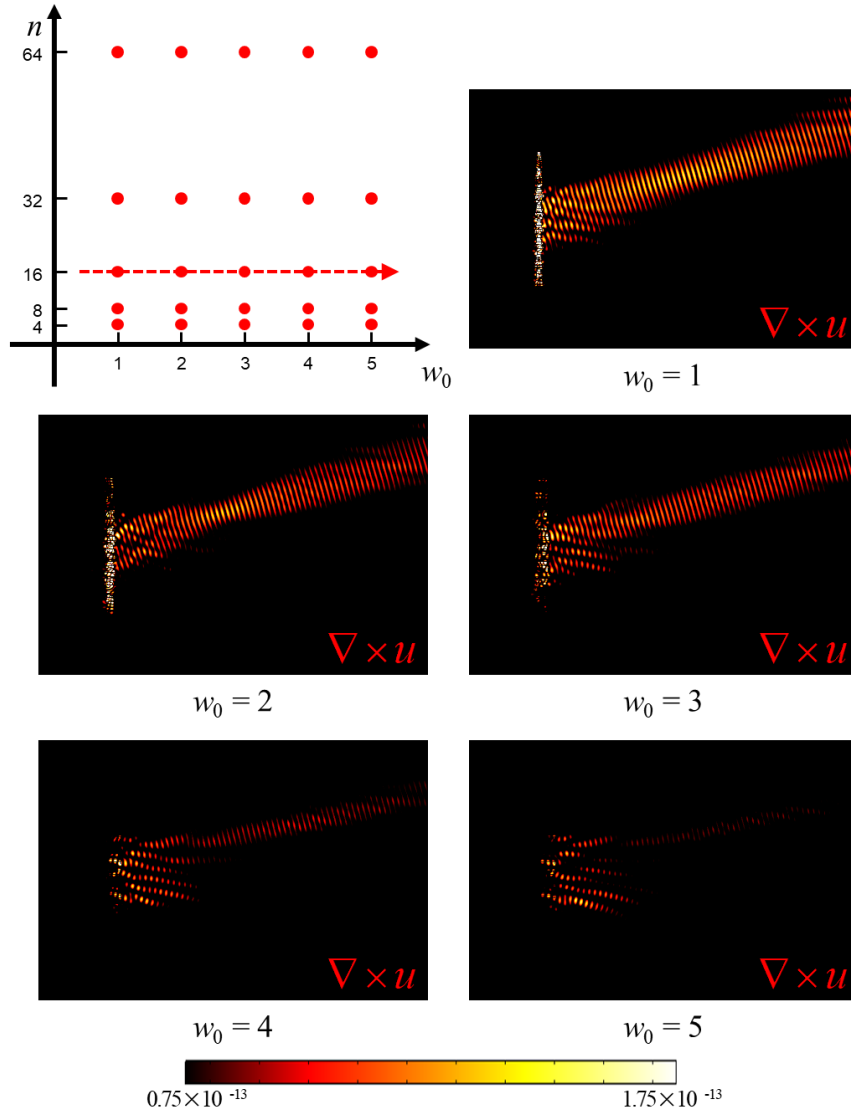


Fig. A.3 The simulation results that plot shear wave field when the phase gradient is small, the smallest thickness w_0 is changed, and the number of unit cells n is fixed.

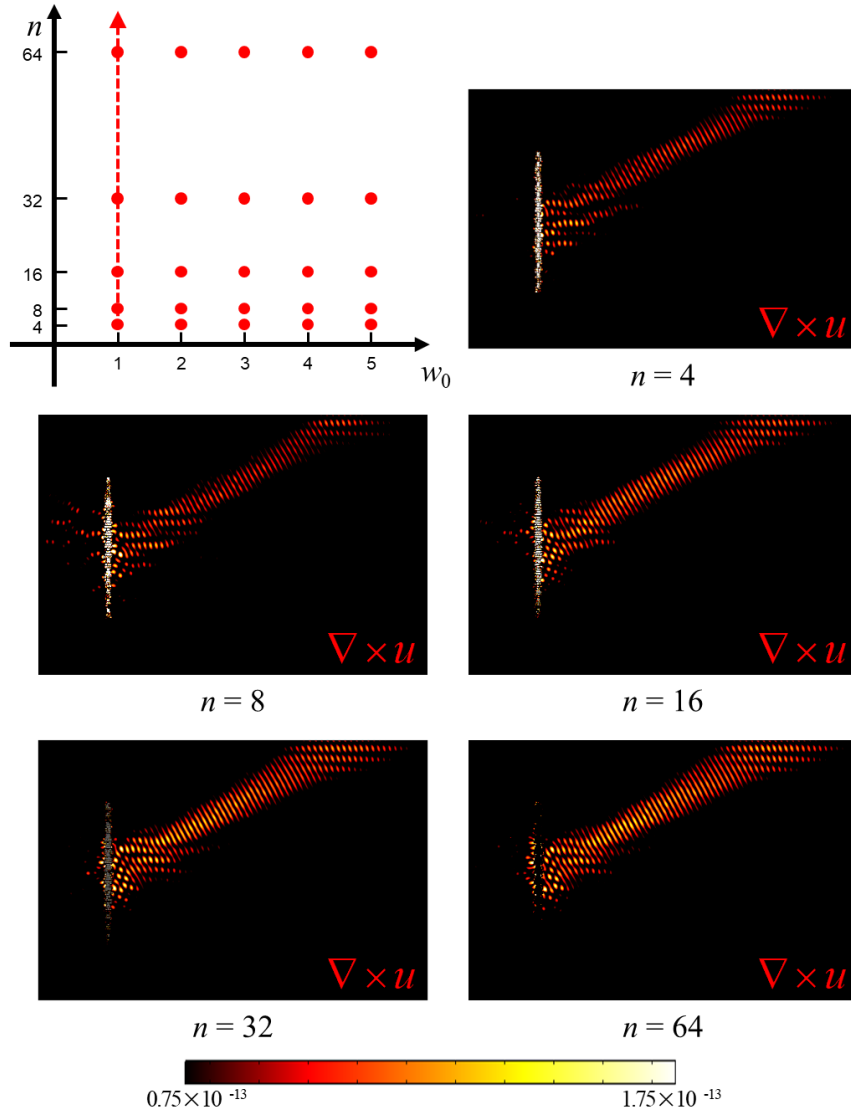


Fig. A.4 The simulation results that plot shear wave field when the phase gradient is large, the smallest thickness w_0 is fixed, and the number of unit cells n is changed.

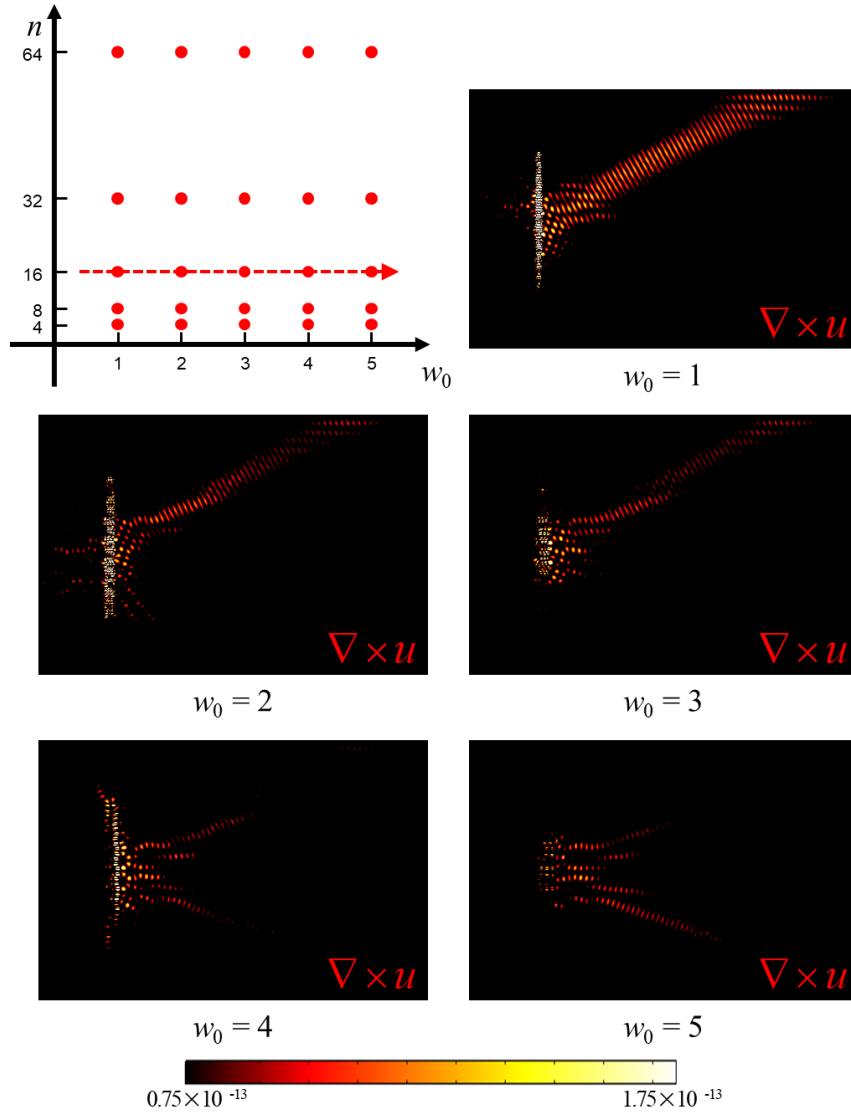


Fig. A.5 The simulation results that plot shear wave field $\nabla \times u$ when the phase gradient is large, the smallest thickness w_0 is changed, and the number of unit cells n is fixed.

REFERENCES

- [1] H. W. Kim, Y. E. Kwon, J. K. Lee, Y. Y. Kim, "Higher torsional mode suppression in a pipe for enhancing the first torsional mode by using magnetostrictive patch transducers", *IEEE Trans. Ultrason. Ferroelectr. Freq. Control* 60 (2013) 562-572.
- [2] P. Cawley, D. N. Alleyne, C. W. chan, "Inspection of pipes", *U.S. Patent* (2000) 6148672
- [3] D. N. Alleyne, B. Pavlakovic, M. J. S. Lowe, P. Cawley, "Rapid long-range inspection of chemical plant pipework using guided waves", *Insight* 43 (2001) 93-96
- [4] M. Torres, F. R. Montero de Espinosa, "Ultrasonic band gaps and negative refraction", *Ultrasonics* 42 (2004) 787-790.
- [5] M. Ke, Z. Liu, C. Qiu, W. Wang, J. Shi, W. Wen, P. Sheng, "Negative-refraction imaging with two-dimensional phononic crystals", *Phys. Rev. B* 72 (2005) 064306.
- [6] J. Li, Z. Liu, C. Qiu, "Negative refraction imaging of acoustic waves by a two-dimensional three-component phononic crystal", *Phys. Rev. B* 73 (2006) 054302.
- [7] A.-C. Hladky-Hennion, J. R. Vasseur, B. Dubus, B. Djafari-Rouhani, D. Ekeom, B. Morvan, "Numerical analysis of negative refraction of transverse waves in an elastic material", *J. Appl. Phys.* 104 (2008) 064906.
- [8] J. Li, Z. Liu, C. Qiu, "Negative refraction imaging of solid acoustic waves by two-dimensional three-component phononic crystal", *Phys. Lett. A* 372 (2008) 3861-3867.
- [9] B. Morvan, A. Tinel, A.-C. Hladky-Hennion, J. R. Vasseur, B. Dubus, "Experimental demonstration of the negative refraction of a transverse elastic wave in a two-dimensional solid phononic crystal", *Appl. Phys. Lett.* 96 (2010) 101905.
- [10] J. Pierre, O. Boyko, L. Belliard, J. R. Vasseur, B. Bonello, "Negative refraction of zero order flexural lamb waves through a two-dimensional phononic crystal", *Appl. Phys. Lett.* 97 (2010) 121919.
- [11] C. Croëne, E. D. Manga, B. Morvan, A. Tinel, B. Dubus, J. R. Vasseur, A.-C. Hladky-Hennion, "Negative refraction of longitudinal waves in a two-dimensional solid-solid phononic crystal", *Phys. Rev. B* 83 (2011) 054301.
- [12] M. K. Lee, P. S. Ma, I. K. Lee, H. W. Kim, Y. Y. Kim, "Negative refraction experiments with guided shear-horizontal waves in thin phononic crystal plates", *Appl. Phys. Lett.* 98 (2011) 011909.
- [13] X. Zhang, Z. Liu, "Negative refraction of acoustic waves in two-dimensional phononic crystals", *Appl. Phys. Lett.* 85 (2004) 341.
- [14] M. H. Lu, C. Zhang, L. Feng, J. Zhao, Y. F. Chen, Y. W. Mao, J. Zi, Y. Y. Zhu, S. N. Zhu, N. B. Ming, "Negative birefraction of acoustic waves in a sonic crystal", *Nat. mater.* 6 (2007) 744-748.
- [15] A. Sukhovich, L. Jing, J. H. Page, "Negative refraction and focusing of ultrasound in two-dimensional phononic crystals", *Phys. Rev. B* 77 (2008) 014301.
- [16] J. Bucay, E. Roussel, J. R. Vasseur, P. A. Deymier, A.-C. Hladky-Hennion, Y. Pennec, K. Muralidharan, B. Djafari-Rouhani, B. Dubus, "Positive, negative, zero

- refraction, and beam splitting in a solid/air phononic crystal: theoretical and experimental study", *Phys. Rev. B* 79 (2009) 214305.
- [17] C. Croëne, B. Morvan, J. R. Vasseur, B. Dubus, A.-C. Hladky-Hennion, "Analysis of elastic waves transmitted through a 2-D phononic crystal exhibiting negative refraction", *IEEE Trans. Ultrason. Ferroelectr.* 58 (2011) 178-186.
- [18] J. R. Vasseur, B. Morvan, A. Tinel, N. Swintek, A.-C. Hladky-Hennion, P. A. Deymier, "Experimental evidence of zero-angle refraction and acoustic wave-phase control in a two-dimensional solid/solid phononic crystal", *Phys. Rev. B* 86 (2012) 134305.
- [19] S. Bringuier, N. Swintek, J. R. Vasseur, J.-F. Robillard, K. Runge, K. Muralidharan, P. A. Deymier, "Phase-controlling phononic crystals: realization of acoustic boolean logic gates", *J. Acoust. Soc. Am.* 130 (2011) 1919-1925.
- [20] N. Swintek, J.-F. Robillard, S. Bringuier, J. Bucay, K. Muralidharan, J. R. Vasseur, K. Runge, P. A. Deymier, "Phase-controlling phononic crystal", *Appl. Phys. Lett.* 98 (2011) 103508.
- [21] H. Lee, J. H. Oh, Y. Y. Kim, "Multiple beam splitting in elastic phononic crystal plates", *Ultrasonics* 56 (2015) 178-182.
- [22] P. Langlet, A.-C. Hladky-Hennion, J.-N. Decarpigny, "Analysis of the propagation of plane acoustic waves in passive periodic materials using the finite element method", *J. Acoust. Soc. Am.* 98 (1995) 2792-2800.
- [23] Comsol Multiphysics, COMSOL Multiphysics Modeling Guide: Version 3.5a, COMSOL AB, Burlington MA, 2008.
- [24] J. S. Lee, Y. Y. Kim, S. H. Cho, "Beam-focused shear-horizontal wave generation in a plate by a circular magneto-strictive patch transducer employing a planar solenoid array", *Smart Mater. Struct.* 18 (2009) 015009.
- [25] Y. Y. Kim, Y. E. Kwon, "Review of magnetostrictive patch transducers and applications in ultrasonic nondestructive testing of waveguides", *Ultrasonics* 62 (2015) 3-19.
- [26] J. C. Hong, K. H. Sun, Y. Y. Kim, "The matching pursuit approach based on the modulated Gaussian pulse for efficient guided-wave damage inspection", *Smart Mater. Struct.* 14 (2005) 548-560.
- [27] H. W. Kim, S. H. Cho, Y. Y. Kim, "Analysis of internal wave reflection within a magnetostrictive patch transducer for high-frequency guided torsional waves", *Ultrasonics* 51.6 (2011) 647-652.
- [28] A. Sukhovich, L. Jing, J. H. Page, "Negative refraction and focusing of ultrasound in two-dimensional phononic crystals", *Phys. Rev. B* 77 (2008) 014301
- [29] H. J. Lee, J. K. Lee, Y. Y. Kim, "Elastic metamaterial-based impedance-varying phononic bandgap structures for bandpass filters", *J. Sound Vibr.* 353 (2015) 58-74
- [30] J. H. Oh, I. K. Lee, P. S. Ma, Y. Y. Kim, "Active wave-guiding of piezoelectric phononic crystals", *Appl. Phys. Lett.* 99 (2011) 083505
- [31] J. H. Oh, H. W. Kim, P. S. Ma, H. M. Seung, Y. Y. Kim, "Inverted bi-prism phononic crystals for one-sided elastic wave transmission applications", *Appl. Phys. Lett.* 100 (2012) 213503

- [32] P. S. Ma, H. W. Kim, J. H. Oh, Y. Y. Kim, "Mode separation of a single-frequency bi-modal elastic wave pulse by a phononic crystal", *Appl. Phys. Lett.* 99 (2011) 201906
- [33] P. S. Ma, Y. E. Kwon, Y. Y. Kim, "Wave dispersion tailoring in an elastic waveguide by phononic crystals", *Appl. Phys. Lett.* 103 (203) 151901
- [34] J. O. Vasseur, O. B. Matar, J. F. Robillard, A.-C. Hladky-Hennion, P. A. Deymier, "Band structures tunability of bulk 2D phononic crystals made of magneto-elastic materials", *AIP Adv.* 1 (2011) 041904
- [35] S. Yoo, Y. J. Kim, Y. Y. Kim, "Hybrid phononic crystals for broad-band frequency noise control by sound blocking and localization", *J. Acoust. Soc. Am.* 132 (2012) EL411-EL416
- [36] L. Zhao, E. Laredo, O. Ryan, A. Yazdkhasti, H. T. Kim, R. Ganye, T. Horiuchi, M. Yu, "Ultrasound beam steering with flattened acoustic metamaterial Luneburg lens", *Appl. Phys. Lett.* 116 (2020) 071902
- [37] A. Arbabi, Y. Horie, M. Bagheri, A. Faraon, "Dielectric metasurfaces for complete control of phase and polarization with subwavelength spatial resolution and high transmission", *Nat. Nanotechnol.* 10 (2015) 937-943
- [38] A. Diaz-Rubio, V. S. Asadchy, A. Elsakka, S. A. Tretyakov, "From the generalized reflection law to the realization of perfect anomalous reflectors", *Sci. Adv.* 3 (2017) e1602714
- [39] A. V. Kildishev, A. Boltasseva, V. M. Shalaev, "Planar Photonics with Metasurfaces", *Science* 339 (6125)
- [40] C. Pfeiffer, A. Grbic, "Metamaterial Huygens' Surfaces: Tailoring Wave Fronts with Reflectionless Sheets", *Phys. Rev. Lett.* 110 (2013) 197401
- [41] C. Pfeiffer, N. K. Emani, A. M. Shaltout, A. Boltasseva, V. M. Shalaev, A. Grbic, "Efficient Light Bending with Isotropic Metamaterial Huygens' Surfaces", *Nano Lett.* 14 (2014) 2491-2497
- [42] F. Aieta, P. Genevet, N. Yu, M. A. Kats, Z. Gaburro, F. Capasso, "Out-of-Plane Reflection and Refraction of Light by Anisotropic Optical Antenna Metasurfaces with Phase Discontinuities", *Nano Lett.* 12 (2012) 1702-1706
- [43] F. Aieta, M. A. Kats, P. Genevet, F. Capasso, "Multiwavelength achromatic metasurfaces by dispersive phase compensation", *Science* 347 (2015) 1342-1345
- [44] F. Monticone, N. M. Estakhri, A. Alu, "Full Control of Nanoscale Optical Transmission with a Composite Metascreen", *Phys. Rev. Lett.* 110 (2013) 203903
- [45] G. Zheng, H. Muhlenbernd, M. Kenney, G. Li, T. Zentgraf, S. Zhang, "Metasurface holograms reaching 80% efficiency", *Nat. Nanotechnol.* 10 (2015) 308-312
- [46] H. T. Chen, A. J. Taylor, N. Yu, "A review of metasurfaces: physics and applications", *Rep. Prog. Phys.* 79 (2016) 076401
- [47] L. Huang, X. Chen, H. Muhlenbernd, G. Li, B. Bai, Q. Tan, G. Jin, T. Zentgraf, S. Zhang, "Dispersionless Phase Discontinuities for Controlling Light Propagation", *Nano Lett.* 12 (2012) 5750-5755
- [48] N. Yu, P. Genevet, M. A. Kats, F. Aieta, J. P. Tetienne, F. Capasso, Z. Gaburro,

- " Light Propagation with Phase Discontinuities: Generalized Laws of Reflection and Refraction", *Science* 334 (2011) 333-337
- [49] N. Yu, F. Capasso, "Flat optics with designer metasurfaces", *Nat. Mater.* 13 (2014) 139-150
- [50] S. Sun, Q. He, S. Xiao, Q. Xu, X. Li, L. Zhou, "Gradient-index meta-surfaces as a bridge linking propagating waves and surface waves", *Nat. Mater.* 11 (2012) 426-431
- [51] X. Ni, N. K. Emani, A. V. Kildishev, A. Boltasseva, V. M. Shalaev, "Broadband Light Bending with Plasmonic Nanoantennas", *Science* 335 (2012) 427-427
- [52] X. Ni, A. V. Kildishev, V. M. Shalaev, "Metasurface holograms for visible light", *Nat. Commun.* 4 (2013) 1-6
- [53] Y. Xu, Y. Fu, H. Chen, "Steering light by a sub-wavelength metallic grating from transformation optics", *Sci. Rep.* 5 (2015) 1-11
- [54] Y. Yang, H. Wang, F. Yu, Z. Xu, H. Chen, "A metasurface carpet cloak for electromagnetic, acoustic and water waves", *Sci. Rep.* 6 (2016) 1-6
- [55] Y. Zhao, A. Alu, "Manipulating light polarization with ultrathin plasmonic metasurfaces", *Phys. Rev. B* 84 (2011) 205428
- [56] B. Liu, W. Zhao, Y. Jiang, "Apparent negative reflection with the gradient acoustic metasurface by integrating supercell periodicity into the Generalized law of reflection", *Sci. Rep.* 6 (2016) 1-9
- [57] C. Ding, X. Zhao, H. Chen, S. Zhai, "Reflected wavefronts modulation with acoustic metasurface based on double-split hollow sphere", *Appl. Phys. A* 120 (2015) 487-493
- [58] C. Ding, H. Chen, S. Zhai, S. Liu, X. Zhao, "The anomalous manipulation of acoustic waves based on planar metasurface with split hollow sphere", *J. Phys. D: Appl. Phys.* 48 (2015) 045303
- [59] C. Faure, O. Richoux, S. Felix, V. Pagneux, "Experiments on metasurface carpet cloaking for audible acoustics", *Appl. Phys. Lett.* 108 (2016) 064103
- [60] C. L. Ding, Z. R. Wang, F. L. Shen, H. J. Chen, S. L. Zhai, "Experimental realization of acoustic metasurface with double-split hollow sphere", *Solid State Commun.* 229 (2016) 28-31
- [61] C. Shen, Y. Xie, J. Li, S. A. Cummer, Y. Jing, "Asymmetric acoustic transmission through near-zero-index and gradient-index metasurfaces", *Appl. Phys. Lett.* 108 (2016) 223502
- [62] G. Ma, M. Yang, S. Xiao, Z. Yang, P. Sheng, "Acoustic metasurface with hybrid resonances", *Nat. Mater.* 13 (2014) 873-878
- [63] H. Esfahlani, S. Karkar, H. Lissek, "Acoustic carpet cloak based on ultrathin metasurface", *Phys. Rev. B* 94 (2016) 014302
- [64] H. T. Sun, J. S. Wang, Y. Cheng, Q. Wei, X. J. Liu, "Modulation of water surface waves with a coiling-up-space metasurface", *AIP Adv.* 6 (2016) 055017
- [65] H. Zhu, F. Semperlotti, "Anomalous Refraction of Acoustic Guided Waves in Solids with Geometrically Tapered Metasurfaces", *Phys. Rev. Lett.* 117 (2016) 034302

- [66] J. Mei, Y. Wu, "Controllable transmission and total reflection through an impedance-matched acoustic metasurface", *New J. Phys.* 16 (2014) 123007
- [67] J. Zhao, B. Li, Z. N. Chen, C. W. Qiu, "Redirection of sound waves using acoustic metasurface", *Appl. Phys. Lett.* 103 (2013) 151604
- [68] J. Zhao, B. Li, Z. Chen, C. W. Qiu, "Manipulating Acoustic Wavefront by Inhomogeneous Impedance and Steerable Extraordinary Reflection", *Sci. Rep.* 3 (2013) 1-6
- [69] K. Tang, C. Qiu, M. Ke, J. Lu, Y. Ye, Z. Liu, "Anomalous refraction of airborne sound through ultrathin metasurfaces", *Sci. Rep.* 4 (2014) 1-7
- [70] M. Moleron, M. Serra-Garcia, C. Daraio, "Acoustic Fresnel lenses with extraordinary transmission", *Appl. Phys. Lett.* 105 (2014) 114109
- [71] P. Peng, B. Xiao, Y. Wu, "Flat acoustic lens by acoustic grating with curled slits", *Phys. Lett. A* 378 (2014) 3389-3392
- [72] P. Zhang, T. Li, J. Zhu, X. Zhu, S. Yang, Y. Wang, X. Yin, X. Zhang, "Generation of acoustic self-bending and bottle beams by phase engineering", *Nat. Commun.* 5 (2014) 1-9
- [73] R. A. Jahdali, Y. Wu, "High transmission acoustic focusing by impedance-matched acoustic meta-surfaces", *Appl. Phys. Lett.* 108 (2016) 031902
- [74] S. Zhai, H. Chen, C. Ding, F. Shen, C. Luo, X. Zhao, "Manipulation of transmitted wave front using ultrathin planar acoustic metasurfaces", *Appl. Phys. A* 120 (2015) 1283-1289
- [75] S. Zhai, H. Chen, C. Ding, L. Li, F. Shen, C. Luo, X. Zhao, "Ultrathin skin cloaks with metasurfaces for audible sound", *J. Phys. D: Appl. Phys.* 49 (2016) 225302
- [76] S. Zhai, C. Ding, H. Chen, F. Shen, C. Luo, X. Zhao, "Anomalous manipulation of acoustic wavefront with an ultrathin planar metasurface", *J. Vib. Acoust.* 138 (2016)
- [77] W. Tang, C. Ren, "Total transmission of airborne sound by impedance-matched ultra-thin metasurfaces", *J. Phys. D: Appl. Phys.* 50 (2017) 105102
- [78] W. Wang, Y. Xie, B. I. Popa, S. A. Cummer, "Subwavelength diffractive acoustics and wavefront manipulation with a reflective acoustic metasurface", *J. Appl. Phys.* 120 (2016) 195103
- [79] X. Wang, X. Wang, W. Yu, Z. Jiang, D. Mao, "Acoustic performance of boundaries having constant phase gradient", *J. Acoust. Soc. Am.* 140 (2016) EL7-EL13
- [80] Y. F. Zhu, X. Y. Zou, R. Q. Li, X. Jiang, J. Tu, B. Liang, J. C. Cheng, "Dispersionless manipulation of reflected acoustic wavefront by subwavelength corrugated surface", *Sci. Rep.* 5 (2015) 1-12
- [81] Y. Li, B. Liang, Z. M. Gu, X. Y. Zou, J. C. Cheng, "Reflected wavefront manipulation based on ultrathin planar acoustic metasurfaces", *Sci. Rep.* 3 (2013) 1-6.
- [82] Y. Li, X. Jiang, R. Q. Li, B. Liang, X. Y. Zou, L. L. Yin, J. C. Cheng, "Experimental realization of full control of reflected waves with subwavelength

- acoustic metasurfaces", *Phys. Rev. Appl.* 2 (2014) 064002
- [83] Y. Li, X. Jiang, B. Liang, J. C. Cheng, L. Zhang, "Metascreen-based acoustic passive phased array", *Phys. Rev. Appl.* 4 (2015) 024003
- [84] Y. Li, M. B. Assouar, "Three-dimensional collimated self-accelerating beam through acoustic metascreen", *Sci. Rep.* 5 (2015) 1-7
- [85] Y. Li, S. Qi, M. B. Assouar, "Theory of metascreen-based acoustic passive phased array", *New J. Phys.* 18 (2016) 043024
- [86] Y. Tian, Q. Wei, Y. Cheng, Z. Xu, X. Liu, "Broadband manipulation of acoustic wavefronts by pentamode metasurface", *Appl. Phys. Lett.* 107 (2015) 221906
- [87] Y. Tian, Q. Wei, Y. Cheng, X. Liu, "Acoustic holography based on composite metasurface with decoupled modulation of phase and amplitude", *Appl. Phys. Lett.* 110 (2017) 191901
- [88] Y. Xie, W. Wang, H. Chen, A. Konneker, B. I. Popa, S. A. Cummer, "Wavefront modulation and subwavelength diffractive acoustics with an acoustic metasurface", *Nat. Commun.* 5 (2014) 1-5
- [89] Y. Zhu, B. Assouar, "Multifunctional acoustic metasurface based on an array of Helmholtz resonators", *Phys. Rev. B* 99 (2019) 174109
- [90] A. Epstein, O. Rabinovich, "Unveiling the properties of metagratings via a detailed analytical model for synthesis and analysis", *Phys. Rev. Appl.* 8 (2017) 054037
- [91] A. M. H. Wong, G. V. Eleftheriades, "Perfect Anomalous Reflection with a Bipartite Huygens' Metasurface", *Phys. Rev. X* 8 (2018) 011036
- [92] L. Quan, Y. Ra'di, D. L. Sounas, A. Alu, "Maximum Willis coupling in acoustic scatterers", *Phys. Rev. Lett.* 120 (2018) 254301
- [93] O. Rabinovich, A. Epstein, "Analytical Design of Printed Circuit Board (PCB) metagratings for perfect anomalous reflection", *IEEE Trans. Antennas Propag.* 66 (2018) 4086-4095
- [94] S. Larouche, D. R. Smith, "Reconciliation of generalized refraction with diffraction theory", *Opt. Lett.* 37 (2012) 2391-2393
- [95] S. Y. Kim, W. Lee, J. S. Lee, Y. Y. Kim, "Longitudinal wave steering using beam-type elastic metagratings", *Mech. Syst. Signal Proc.* 156 (2021) 107688
- [96] S. R. Craig, X. Su, A. Norris, C. Shi, "Experimental realization of acoustic bianisotropic gratings", *Phys. Rev. Appl.* 11 (2019) 061002
- [97] V. Popov, F. Boust, S. N. Burokur, "Controlling diffraction patterns with metagratings", *Phys. Rev. Appl.* 10 (2018) 011002
- [98] Y. Ra'di, D. L. Sounas, A. Alu, "Metagratings: Beyond the Limits of Graded Metasurfaces for Wave Front Control", *Phys. Rev. Lett.* 119 (2017) 067404
- [99] H. Lee, J. K. Lee, H. M. Seung, Y. Y. Kim, "Mass-stiffness substructuring of an elastic metasurface for full transmission beam steering", *J. Mech. Phys. Solids* 112 (2018) 577-593
- [100] L. Cao, Y. Xu, B. Assouar, Z. Yang, "Asymmetric flexural wave transmission based on dual-layer elastic gradient metasurfaces", *Appl. Phys. Lett.* 113 (2018) 183506

- [101] L. Cao, Z. Yang, Y. Xu, "Steering elastic SH waves in an anomalous way by metasurface", *J. Sound Vibr.* 418 (2018) 1-14
- [102] L. Cao, Z. Yang, Y. Xu, B. Assouar, "Deflecting flexural wave with high transmission by using pillared elastic metasurface", *Smart Mater. Struct.* 27 (2018) 075051
- [103] S. Li, J. Xu, J. Tang, "Tunable modulation of refracted lamb wave front facilitated by adaptive elastic metasurfaces", *Appl. Phys. Lett.* 112 (2018) 021903
- [104] S. M. Yuan, A. L. Chen, L. Cao, H. W. Zhang, S. W. Fan, B. Assouar, Y. S. Wang, "Tunable multifunctional fish-bone elastic metasurface for the wavefront manipulation of the transmitted in-plane waves", *J. Appl. Phys.* 128 (2020) 224502
- [105] S. W. Lee, J. H. Oh, "Single layer elastic metasurface with double negativity for anomalous refraction", *J. Phys. D: Appl. Phys.* 53 (2020) 265301
- [106] X. Su, A. N. Norris, "Focusing, refraction, and asymmetric transmission of elastic waves in solid metamaterials with aligned parallel gaps", *J. Acoust. Soc. Am.* 139 (2016) 3386
- [107] X. Su, Z. Lu, A. N. Norris, "Elastic metasurfaces for splitting SV- and P-waves in elastic solids", *J. Appl. Phys.* 123 (2018) 091701
- [108] X. Wu, X. Xia, J. Tian, Z. Liu, W. Wen, "Broadband reflective metasurface for focusing underwater ultrasonic waves with linearly tunable focal length", *Appl. Phys. Lett.* 108 (2016) 163502
- [109] Y. Liu, Z. Liang, F. Liu, O. Diba, A. Lamb, J. Li, "Source Illusion Devices for Flexural Lamb Waves Using Elastic Metasurfaces", *Phys. Rev. Lett.* 119 (2017) 034301
- [110] A. Colombi, D. Colquitt, P. Roux, S. Guenneau, R. V. Craster, "A seismic metamaterial: The resonant metawedge", *Sci. Rep.* 6 (2016) 1-6
- [111] A. Colombi, V. Ageeva, R. J. Smith, A. Clare, R. Patel, M. Clark, D. Colquitt, P. Roux, S. Guenneau, R. V. Craster, "Enhanced sensing and conversion of ultrasonic Rayleigh waves by elastic metasurfaces", *Sci. Rep.* 7 (2017) 1-9
- [112] M. S. Kim, W. R. Lee, Y. Y. Kim, J. H. Oh, "Transmodal elastic metasurface for broad angle total mode conversion", *Appl. Phys. Lett.* 112 (2018) 241905
- [113] S. W. Lee, H. M. Seung, W. Choi, M. Kim, J. H. Oh, "Broad-angle refractive transmodal elastic metasurface", *Appl. Phys. Lett.* 117 (2020) 213502
- [114] X. Li, Y. Chen, X. Zhang, G. Huang, "Shaping elastic wave mode conversion with a piezoelectric-based programmable meta-boundary", *Extreme Mech. Lett.* 39 (2020) 100837
- [115] J. M. Kweun, H. J. Lee, J. H. Oh, H. M. Seung, Y. Y. Kim, "Transmodal Fabry-Perot Resonance: Theory and Realization with Elastic Metamaterials", *Phys. Rev. Lett.* 118 (2017) 205901
- [116] X. Yang, Y. Y. Kim, "Topology optimization for the design of perfect mode-converting anisotropic elastic metamaterials", *Compos. Struct.* 201 (2018) 161-177
- [117] X. Yang, Y. Y. Kim, "Asymptotic theory of bimodal quarter-wave impedance matching for full mode-converting transmission", *Phys. Rev. B.* 98 (2018) 144110
- [118] X. Yang, J. M. Kweun, Y. Y. Kim, "Theory for Perfect Transmodal Fabry-Perot

Interferometer", *Sci. Rep.* 8 (2018) 1-6

[119] X. Yang, M. Kweun, Y. Y. Kim, "Monolayer metamaterial for full modeconverting transmission of elastic waves", *Appl. Phys. Lett.* 115 (2019) 071901

ABSTRACT (KOREAN)

탄성파 모드 제어와 빔 조향이 가능한 메타물질

이우림

서울대학교 대학원

기계항공공학부

본 연구에서는 탄성파에 있는 다중 모드를 정밀하게 제어하고, 동시에 파동의 방향을 제어하는 탄성 메타물질의 설계 및 검증하는 것을 목표로 한다. 탄성 초음파는 비파괴검사 및 의료계 장비 등의 다양한 응용 분야에서 활용되고 있으며, 그렇기 때문에 초음파를 정밀하게 제어하는 기술은 굉장히 중요하다. 최근에 초음파를 획기적으로 제어할 수 있는 구조물인 탄성 메타물질이 주목받고 있지만, 탄성파는 종파와 횡파 등의 다중모드의 존재로 인해 제어가 특히 까다롭다. 이는 결과적으로 파동의 제어기술에 심각한 제한을 걸고 있다.

이러한 한계를 해결하기 위해 본 연구에서는 탄성파의 방향제어와 동시에 모드제어를 목표로 할 수 있는 메타물질을 제안한다. 구체적으로는,

탄성 음향자 결정구조와 탄성 메타표면을 이용하여 파동의 방향을 제어한다. 원하는 모드의 파동만이 전파하는 조건을 찾아내어 메타물질 설계에 고려한다. 먼저, 탄성 음향자 결정구조에서는 모드 해석을 통해, 한 가지 모드의 파동이 전파한다. 설계된 탄성 음향자 결정구조가 탄성 초음파를 정밀하게 제어하는 것을 실험을 통해 검증하였다.

다음으로, 탄성 메타표면에서는 특정 모드의 입사파를 동일 모드 혹은 다른 모드로, 원하는 모드의 투과파로 변환시킨다. 동시에 원하는 방향으로의 투과파 빔 조향을 구현한다. 파동의 전달 행렬과 산란 행렬을 이용하여, 위상 변이를 제어하는 단위구조의 물성치를 파악한다. 설계한 단일층 메타물질은 모드보존 혹은 모드변환을 하면서 위상 변이를 제어하고, 투과파를 원하는 방향으로 제어할 수 있다. 제안된 메타물질 해석 및 설계 기법은 정교한 제어를 요구하는 탄성 초음파 기술을 크게 향상시킬 것으로 기대된다.

주요어: 탄성 메타물질, 유도 초음파, 탄성과 모드 제어, 빔 조향, 음향자 결정구조, 메타표면.

학 번 : 2015-20704

ACKNOWLEDGEMENTS

This research was supported by grants from the National Research Foundation of Korea (NRF) (Grant Nos. 2014M3A6B3063711) funded by the Korean Government contracted through IAMD (Institute of Advanced Machines and Design) at Seoul National University.